Alma Mater Studiorum · Università di Bologna

Scuola di Scienze
Corso di Laurea Magistrale in Fisica

Measurement of $\mathcal{CP}$ asymmetries in $\Lambda_b^0 \to pK^-$ and $\Lambda_b^0 \to p\pi^-$ decays at LHCb

Relatore:
Prof. Angelo Carbone

Correlatore:
Dott. Stefano Perazzini

Presentata da:
Fabio Ferrari

Sessione I
Anno Accademico 2013/2014

"If it disagrees with experiments, it's wrong.
In that simple statement is the key to science.
It doesn't make a difference how beautiful your guess is,
it doesn't matter how smart you are,
who made the guess or what his name is.
If it disagrees with experiments, it's wrong – that's all there is to it."

Richard P. Feynman

Abstract

L'esperimento LHCb è stato progettato per realizzare misure di precisione nel settore della fisica del *flavour* al Large Hadron Collider (LHC) presso il CERN. Dopo la recente osservazione della violazione della simmetria $\mathcal{CP}$ nel decadimento del mesone B_s^0 in una coppia pione-kaone, è interessante vedere qualora la stessa transizione nei decadimenti dei barioni Λ_b^0, al livello dei quark coinvolti, dia luogo a grandi effetti di violazione di $\mathcal{CP}$. Questi decadimenti ricevono contributi sia da diagrammi di Feynman ad albero, sia da diagrammi cosiddetti a pinguino, e possono essere sensibili alla presenza di fisica oltre il Modello Standard.

La misura dell'osservabile di violazione di $\mathcal{CP}$ definito come $\Delta\mathcal{A}_{CP} = \mathcal{A}_{\mathcal{CP}}(\Lambda_b^0 \to pK^-) - \mathcal{A}_{\mathcal{CP}}(\Lambda_b^0 \to p\pi^-)$, dove $\mathcal{A}_{\mathcal{CP}}(\Lambda_b^0 \to pK^-)$ e $\mathcal{A}_{\mathcal{CP}}(\Lambda_b^0 \to p\pi^-)$ sono le asimmetrie di violazione diretta di $\mathcal{CP}$ nei decadimenti $\Lambda_b^0 \to pK^-$ e $\Lambda_b^0 \to p\pi^-$, viene presentata per la prima volta usando i dati di LHCb. La procedura seguita per ottimizzare la selezione degli eventi, per calibrare l'identificazione delle particelle, per parametrizzare le varie componenti presenti nello spettro di massa invariante, e per calcolare le correzioni dovute alla presenza di un'asimmetria di produzione dello stato iniziale e asimmetrie di rivelazione degli stati finali, è descritta in dettaglio.

Utilizzando i campioni completi di collisioni pp, acquisiti nel 2011 e nel 2012 dal rivelatore LHCb e corrispondenti ad una luminosità integrata di circa 3 fb^{-1}, si ottiene il valore $\Delta\mathcal{A}_{\mathcal{CP}} = (0.8 \pm 2.1 \pm 0.2)\%$. La prima delle due incertezze è di natura statistica mentre la seconda corrisponde ad uno degli effetti sistematici dominanti. Essendo questo risultato compatibile con zero, non viene evidenziata la presenza di violazione della simmetria $\mathcal{CP}$. Questa è la misura più precisa di violazione di $\mathcal{CP}$ nei decadimenti di barioni contenenti quark b mai realizzata. Quando l'analisi sarà ultimata con uno studio esaustivo di tutte le incertezze sistematiche, i risultati saranno pubblicati dalla Collaborazione LHCb.

Abstract

The LHCb experiment has been designed to perform precision measurements in the flavour physics sector at the Large Hadron Collider (LHC) located at CERN. After the recent observation of $\mathcal{CP}$ violation in the decay of the B_s^0 meson to a charged pion-kaon pair at LHCb, it is interesting to see whether the same quark-level transition in Λ_b^0 baryon decays gives rise to large $\mathcal{CP}$-violating effects. Such decay processes involve both tree and penguin Feynman diagrams and could be sensitive probes for physics beyond the Standard Model.

The measurement of the $\mathcal{CP}$-violating observable defined as $\Delta\mathcal{A}_{CP} = \mathcal{A}_{\mathcal{CP}}(\Lambda_b^0 \to pK^-) - \mathcal{A}_{\mathcal{CP}}(\Lambda_b^0 \to p\pi^-)$, where $\mathcal{A}_{\mathcal{CP}}(\Lambda_b^0 \to pK^-)$ and $\mathcal{A}_{\mathcal{CP}}(\Lambda_b^0 \to p\pi^-)$ are the direct $\mathcal{CP}$ asymmetries in $\Lambda_b^0 \to pK^-$ and $\Lambda_b^0 \to p\pi^-$ decays, is presented for the first time using LHCb data. The procedure followed to optimize the event selection, to calibrate particle identification, to parametrise the various components of the invariant mass spectra, and to compute corrections due to the production asymmetry of the initial state and the detection asymmetries of the final states, is discussed in detail.

Using the full 2011 and 2012 data sets of pp collisions collected with the LHCb detector, corresponding to an integrated luminosity of about 3 fb^{-1}, the value $\Delta\mathcal{A}_{\mathcal{CP}} = (0.8 \pm 2.1 \pm 0.2)\%$ is obtained. The first uncertainty is statistical and the second corresponds to one of the dominant systematic effects. As the result is compatible with zero, no evidence of $\mathcal{CP}$ violation is found. This is the most precise measurement of $\mathcal{CP}$ violation in the decays of baryons containing the b quark to date. Once the analysis will be completed with an exhaustive study of systematic uncertainties, the results will be published by the LHCb Collaboration.

Contents

Introduction

One of the most intriguing questions in modern physics is why we do not observe the presence of antimatter in our universe. This question is directly related to the study of $\mathcal{CP}$ violation in particle physics.

Up to 60 years ago, it was believed that all laws of Nature were invariant under the application of charge-conjugation ($\mathcal{C}$) and parity ($\mathcal{P}$) transformations. After a careful review of all the particle experiments conducted until then, Tsung Dao Lee and Chen Ning Yang realized in 1956 that there was no experimental reason to believe that the $\mathcal{P}$ symmetry was conserved. Hence they proposed a series of experiments that could be carried out to verify that assumption. The suggestion was positively received by C. S. Wu and her team, which in 1957 found a clear violation of $\mathcal{P}$ conservation in the ^{60}Co β decay [1]. After this experimental evidence, the fact that the $\mathcal{P}$ symmetry was violated by weak interactions was definitively established. A subsequent experiment made by Goldhaber *et .al.* [2] in 1958 showed that the neutrino is *left-handed*, *i.e.* its spin is antiparallel with respect to its momentum. It was soon pointed out that the independent application of $\mathcal{C}$ and $\mathcal{P}$ operators to the *left-handed* neutrino (ν_L) led to physical states not observed in Nature (*right-handed* neutrino (ν_R) and *left-handed* anti-neutrino ($\bar{\nu}_L$), respectively), but that the application of the $\mathcal{CP}$ operator to the ν_L led to the observed $\bar{\nu}_R$. For this reason it was thought that the $\mathcal{CP}$ symmetry was indeed conserved. However, in 1964, Cronin and Fitch discovered that the $\mathcal{CP}$ symmetry was broken in a small fraction of K_L^0 decays [3], yielding the first experimental evidence of $\mathcal{CP}$ violation.

Murray Gell-Mann and George Zweig developed some years later a classification scheme for hadrons that soon would have be known as quark model. This model initially comprised only the *up*, *down* and *strange* quarks. In 1963, to preserve the universality of weak interactions, *i.e.* the fact that the coupling constant was the same in all transitions, Nicola Cabibbo introduced a mixing angle θ_C (the so-called Cabibbo angle) and made the hypothesis that the state coupling to the up quark was a superposition of down-type quarks, *i.e.*:

$$d' = d\cos(\theta_C) + s\sin(\theta_C) \ .$$

Few years later, in 1970, Glashow, Iliopoulos, and Maiani proposed to explain the observed suppression of flavour-changing neutral currents (FCNC) processes with the hy-

pothesis that the up quark coupled to a second superposition of down-type quarks, orthogonal to d' and defined as:

$$s' = -d\sin(\theta_C) + s\cos(\theta_C) \ .$$

Moreover, to completely cancel the tree-level FCNC diagrams, they also theorized the existence of a fourth quark, the *charm* quark [4]. This prediction was experimentally confirmed four years later by two experimental groups led by Samuel C. C. Ting at the Brookhaven National Laboratory [5] and by Burton Richter at the Stanford Linear Accelerator [6], through the discovery of the first $c\bar{c}$ resonance, called the J/ψ meson.

We can write d' and s' combinations in matrix notation as:

$$\begin{pmatrix} d' \\ s' \end{pmatrix} = \begin{pmatrix} \cos\theta_C & \sin\theta_C \\ -\sin\theta_C & \cos\theta_C \end{pmatrix} \begin{pmatrix} d \\ s \end{pmatrix} \ ,$$

where the 2×2 matrix is known as Cabibbo matrix.

By noticing that $\mathcal{CP}$ violation could not be explained in a four-quark model, Kobayashi and Maskawa generalized the Cabibbo matrix into the so-called Cabibbo–Kobayashi–Maskawa matrix [7] (or CKM matrix):

$$\begin{pmatrix} d' \\ s' \\ b' \end{pmatrix} = \begin{pmatrix} V_{ud} & V_{us} & V_{ub} \\ V_{cd} & V_{cs} & V_{cb} \\ V_{td} & V_{ts} & V_{tb} \end{pmatrix} \begin{pmatrix} d \\ s \\ b \end{pmatrix} \ ,$$

thus predicting the existence of another quark doublet [7]. This hypothesis was then confirmed with the discovery of the *bottom* quark in 1977 by Leon M. Lederman and collaborators at FermiLab [8] and with the discovery of the *top* quark in 1995 by the CDF [9] and DØ [10] collaborations. The CKM matrix is characterized by four free parameters: three mixing angles and one complex phase, the latter accounting for $\mathcal{CP}$ violation. This formalism has proven to be very successful in explaining and predicting $\mathcal{CP}$ violation in different decays. For their work, Kobayashi and Maskawa were awarded with the Nobel Prize in 2008.

Since its discovery in 1964, a systematic study of the $\mathcal{CP}$ violation phenomenon has been carried out by a number of experiments. Another important leap was made owing to the ARGUS collaboration, that discovered in 1987 the $B^0 - \bar{B}^0$ mixing and opened the venue for the measurement of $\mathcal{CP}$ violation using mesons containing the b quark. Few years ago the CDF Collaboration reported the first observation of $B_s^0 - \bar{B}_s^0$ mixing [11], and very recently the LHCb Collaboration that of $D^0 - \bar{D}^0$ mixing [12]. The existence of $\mathcal{CP}$ violation in the decays of B^0 mesons was actually demonstrated by the BaBar and Belle experiments [13,14]. Finally, the first observation of $\mathcal{CP}$ violation in B_s^0 decays was reported by LHCb [15].

$\mathcal{CP}$ violation is still nowadays a very promising field of research, with an exhaustive programme of precision measurements being pursued by LHCb, and another venue going

to be opened by the Belle II experiment in Japan. In particular, charmless two-body decays of *beauty* baryons involve elements of the CKM matrix that could be sensitive to physics beyond the Standard Model, as these decays proceed also through loop-level quark transitions. For this reason, it is important to measure $\mathcal{CP}$ violation in such decays.

This thesis focuses on the $\Lambda_b^0 \to pK^-$ and $\Lambda_b^0 \to p\pi^-$ decays, discussing measurements of $\mathcal{CP}$ violation using data collected with the LHCb detector. LHCb is one of the four major experiments currently active at the CERN Large Hadron Collider (LHC) in Geneva, specifically dedicated to the study of $\mathcal{CP}$ violation and rare decays of *beauty* and *charm* hadrons. The thesis is organized as follows.

In the first chapter, theoretical aspects of the Standard Model of particle physics are presented. A brief overview of the CKM formalism and of the present experimental status concerning CKM matrix elements is given. Then, the basic tools needed to cope with the phenomenology of b-hadron decays are discussed.

The second chapter is dedicated to the description of the LHCb detector. It starts with a brief overview of the LHC collider and its operation, and then the LHCb detector and all of its sub-detectors are described in detail. Particular attention is payed on the particle identification sub-detectors, which are very relevant for the analysis of the decays under study. Finally, the trigger system used to acquire data during the physics runs is described, along with the data management and computing systems used in the offline analysis.

In the third chapter, the details of the analysis performed to measure $\mathcal{CP}$ violation in $\Lambda_b^0 \to pK^-$ and $\Lambda_b^0 \to p\pi^-$ decays are given. First of all a description of the trigger selection and of the procedure developed to calibrate the response of particle identification sub-detectors is given. Then the model used to parametrise the invariant mass shape in the maximum likelihood fits and the offline selection optimised to obtain the best statistical sensitivity on the $\mathcal{CP}$ asymmetries are presented. Finally, the value of the physical quantity $\Delta\mathcal{A}_{\mathcal{CP}} = \mathcal{A}_{\mathcal{CP}}(\Lambda_b^0 \to pK^-) - \mathcal{A}_{\mathcal{CP}}(\Lambda_b^0 \to p\pi^-)$, where $\mathcal{A}_{\mathcal{CP}}(\Lambda_b^0 \to pK^-)$ and $\mathcal{A}_{\mathcal{CP}}(\Lambda_b^0 \to p\pi^-)$ are the direct $\mathcal{CP}$ asymmetries in $\Lambda_b^0 \to pK^-$ and $\Lambda_b^0 \to p\pi^-$ decays, is quoted as the final results of the thesis, and conclusions are drawn.

Chapter 1

$\mathcal{CP}$ violation in charmless charged two-body H_b decays

$\mathcal{CP}$ violation, *i.e.* the non-invariance of fundamental interactions under the charge conjugation ($\mathcal{C}$) and parity ($\mathcal{P}$) operations, is one of the most relevant topics in modern physics. Using the Dirac notation and applying the $\mathcal{C}$ operator to a particle, we obtain its antiparticle:

$$\mathcal{C}|\pi^+\rangle = |\pi^-\rangle \ , \tag{1.1}$$

i.e. the $\mathcal{C}$ operator acts on the internal quantum numbers of a particle and changes their sign (*e.g.* $Q \to -Q$ for the electric charge). Applying it a second time we obtain:

$$\mathcal{C}^2|\pi^+\rangle = \mathcal{C}|\pi^-\rangle = |\pi^+\rangle \Rightarrow \mathcal{C}^2 = 1 \ , \tag{1.2}$$

hence the eigenvalues of the $\mathcal{C}$ operator are ± 1. Under the $\mathcal{P}$ operator, spatial coordinates are reversed

$$\mathcal{P}|\vec{x}\rangle = |-\vec{x}\rangle \ , \tag{1.3}$$

and this translates in changing the handedness of the reference frame. If we apply the $\mathcal{P}$ operator a second time we obtain:

$$\mathcal{P}^2|\vec{x}\rangle = \mathcal{P}|-\vec{x}\rangle = |\vec{x}\rangle \Rightarrow \mathcal{P}^2 = 1 \ , \tag{1.4}$$

hence, again, the eigenvalues of the $\mathcal{P}$ operator are ± 1. When we apply these two operators together, their eigenvalues must be multiplied, since they are discrete operators, and so the $\mathcal{CP}$ eigenvalues are also ± 1. Naively speaking, there is $\mathcal{CP}$ violation when the $\mathcal{CP}$-eigenvalue associated to the initial state is different from that of the final state.

If the $\mathcal{CP}$ symmetry were an exact symmetry of Nature, the behavior of matter and antimatter would be the same. During the past years it has been discovered that only gravitational, electromagnetic and strong interactions respect the $\mathcal{C}$ and $\mathcal{P}$ symmetries and, therefore, also their combination $\mathcal{CP}$. Conversely, it has been found that weak

interactions do not respect $\mathcal{P}$ and $\mathcal{C}$ symmetries. Before 1964 it was thought that all of the fundamental interactions had to respect the $\mathcal{CP}$ symmetry, but an experiment by Fitch and Cronin, involving neutral kaon decays, observed for the first time that also $\mathcal{CP}$ was violated [3]. From that moment, $\mathcal{CP}$ violation has been deeply studied using decays of K, B and D hadrons.

$\mathcal{CP}$ violation can arise from three different sources, namely:

- the flavor mixing of neutral mesons, *i.e.* the transformation of a neutral meson to its $\mathcal{CP}$ counterpart;
- directly from decay diagrams, where the decay rate of a particle to a final state differs from the decay rate of the relative antiparticle to the charge coniugate final state;
- in the interference between mixing and decay.

$\mathcal{CP}$ violation is nowadays a well established for what concerns K^0 and B^0 decays [16] - [25]; in the case of D mesons, the LHCb collaboration has recently found an evidence for $\mathcal{CP}$ violation [26]. Finally, in 2013 the LHCb Collaboration observed for the first time the presence of $\mathcal{CP}$ violation in the decays of the B_s^0 meson [15].

1.1 The Standard Model

The Standard Model (SM) is the theory that describes electromagnetic, weak and strong interactions, responsible for the dynamics of the known sub-atomic particles. The particles contained in this model are divided into two families: fermions (with semi-integer spin) and bosons (with integer spin). Fermions are then further divided into leptons and quarks, depending on whether they interact via the electromagnetic and weak forces only, or also via the strong force. Moreover, leptons and quarks are then organized in 3 families, as shown in Fig. 1.1.

Quarks have semi-integer charges ($+2/3$ for the up type members and $-1/3$ for the down type members), while leptons have integer charges (-1 for the up type members and 0 for the neutrinos). Fermions are the fundamental constituents of the matter and they interact exchanging force carriers. Each interaction has its own mediator: γ for the electromagnetic interaction, $W^{\pm}$ and Z^0 for the weak interaction and 8 gluons for the strong interaction. Their masses and their principal properties are reported in Fig. 1.1. In 2012, the ATLAS and CMS collaborations have discovered a new boson that so far has shown to have the properties of the Standard Model Higgs Boson.

Quarks can form hadrons, that are subdivided into mesons, composed of a $q\bar{q}$ pair, and baryons, composed of three quarks (or anti-quarks).

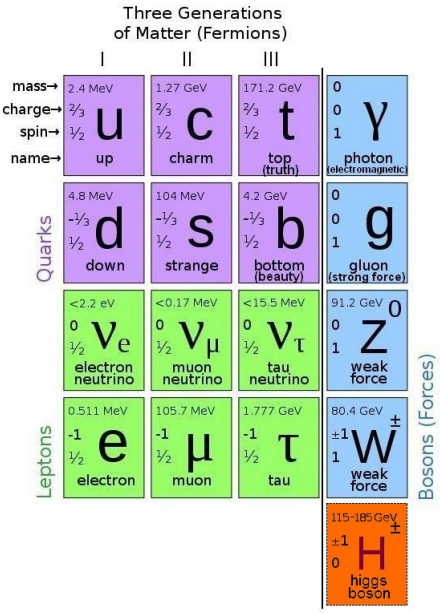

Figure 1.1: Elementary particles forming the Standard Model. We can see six quarks (purple background), six leptons (green background), four bosons (blue background) and the Higgs boson (orange background).

The SM is described by a Lagrangian density that is invariant under non-abelian local gauge transformations [28]. The local gauge symmetry group for the SM is:

$$G_{SM} = SU(3)_C \otimes SU(2)_L \otimes U(1)_Y. \tag{1.5}$$

The color interactions, described by the quantum chromodynamics (QCD), are obtained requiring the local gauge invariance of the Lagrangian for $SU(3)_C$ transformations, while the request of invariance for transformations of the $SU(2)_L \otimes U(1)_Y$ group describes the electroweak interactions.

The most general renormalizable Lagrangian consistent with the symmetry group (1.5) that describes the SM interactions can be divided into four parts:

$$\mathcal{L}_{SM} = \mathcal{L}_{Gauge} + \mathcal{L}_{Kinetic} + \mathcal{L}_{Higgs} + \mathcal{L}_{Yukawa} \tag{1.6}$$

The first term in $\mathcal{L}_{SM}$ describes the propagation of gauge fields and is given by

$$\mathcal{L}_{Gauge} = -\frac{1}{4} G^a_{\mu\nu} (G^a)^{\mu\nu} - \frac{1}{4} W^d_{\mu\nu} (W^d)^{\mu\nu} - \frac{1}{4} B_{\mu\nu} B^{\mu\nu}, \tag{1.7}$$

with

$$G^a_{\mu\nu} \quad = \quad \partial_\mu G^a_\nu - \partial_\nu G^a_\mu + g_s f_{abc} G^b \mu G^c_\nu$$

$$\begin{aligned} W^d_{\mu\nu} &= \partial_\mu W^d_\nu - \partial_\nu W^d_\mu + g\varepsilon_{def} W^e_\mu W^f_\nu \\ B_{\mu\nu} &= \partial_\mu B_\nu - \partial_\nu B\mu \end{aligned} \tag{1.8}$$

where:

- $G^a_{\mu\nu}$ is the Yang-Mills tensor that represents the eight ($a = 1, 2, \ldots, 8$) gluon fields G^a_μ, g_s is the strong coupling constant and f_{abc} are the $SU(3)_C$ structure constants.
- $W^d_{\mu\nu}$ is the weak field tensor that represent three ($d = 1, 2, 3$) gauge fields W^d_μ, g is the Quantum Flavour Dynamics (QFD) coupling constant and ε_{def} are the $SU(2)_W$ structure constants.
- $B_{\mu\nu}$ is the electromagnetic tensor that represents the $U(1)_Y$ gauge field B_μ.

The presence of the $f_{abc}G^b_\mu G^c_\nu$ and $\varepsilon_{def}W^e_\mu, W^f_\nu$ terms in the first two equations above indicates that QCD and QFD are non-abelian theories, whose gauge fields can then self-interact. This no longer holds for QED that forbids photon self-interaction, being an abelian theory.

The second term contained in $\mathcal{L}_{SM}$ describes the kinetic energy of fermions and their interaction with gauge fields:

$$\mathcal{L}_{Kinetic} = \bar{\psi}\gamma^\mu i D_\mu \psi \tag{1.9}$$

where γ^μ are the Dirac matrices, ψ is a Dirac spinor, $\bar{\psi} = \psi^\dagger\gamma^0$ is an adjoint Dirac spinor and D_μ it the covariant derivative definite as

$$D_\mu = \underbrace{\partial_\mu + \frac{ig}{2}W^d_\mu\sigma_d + \frac{ig'}{2}B_\mu Y}_{\nabla_\mu} + \frac{ig_s}{2}G^a_\mu\lambda_a. \tag{1.10}$$

In this equation we have Y, σ_d and λ_a that are respectively the $U(1)_Y$, $SU(2)_W$ and $SU(3)_C$ symmetry groups generators, g' that is the electromagnetic coupling constant and ∇_μ that represents the covariant derivative of the electroweak sector; finally σ_d and λ_a are the 2×2 Pauli matrices and the 3×3 Gell-Mann matrices.

The third part of $\mathcal{L}_{SM}$ is the Higgs Lagrangian, that describes the spontaneous electroweak symmetry breaking (EWSB) that allows all SM particles to acquire mass. This Lagrangian is written as

$$\mathcal{L}_{Higgs} = (\nabla_\mu\phi)^\dagger(\nabla^\mu\phi) + \underbrace{\mu^2\phi^\dagger\phi + \lambda(\phi^\dagger\phi)^2}_{V(\phi^\dagger\phi)} \tag{1.11}$$

where the first term represents the kinetic energy of the Higgs field together with its gauge interactions and other terms represent, respectively, the mass term and the self-interaction term. Those two terms form the Higgs potential, indicated as $V(\phi^\dagger\phi)$, in

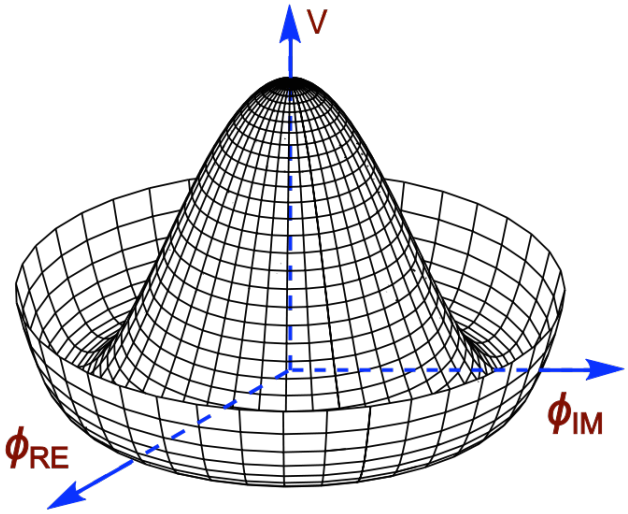

Figure 1.2: Higgs potential representation with the bonds $\mu^2 < 0$ and $\lambda > 0$.

which μ and λ are parameters not predicted by the theory and are commonly called *mass* and *quartic coupling*.

The most important aspect of the Higgs Mechanism is the introduction of a scalar field ϕ

$$\phi = \frac{1}{\sqrt{2}} \begin{pmatrix} \phi^\dagger \\ \phi^0 \end{pmatrix}, \tag{1.12}$$

assumed to be present everywhere in the space-time and weakly self-interacting. This modifies the vacuum state making it non-symmetric. In this way, masses are dynamically generated thanks to their interaction with the ϕ field, or to be more accurate, with the excitation of this field, the Higgs boson. A convenient bound for the free parameters is $\mu^2 < 0$ and $\lambda > 0$: in this way the Higgs potential assumes the shape of a mexican hat, as shown in Fig. 1.2 and the vacuum state $\phi = 0$ becomes a local maximum that disturbs the symmetry of the system, making it unstable. If one sets $\phi^\dagger = 0$, $\phi^0 = v$ and $Y = 1$ where v is the value of the infinite degenerate minima, then the Higgs field acquires a vacuum expectation value (VEV) $\langle\phi\rangle_0$ expressed as

$$\langle\phi\rangle_0 = \frac{1}{\sqrt{2}} \begin{pmatrix} 0 \\ v \end{pmatrix} \quad \text{with} \quad v = \sqrt{\frac{-\mu^2}{\lambda}} \simeq 246\text{GeV} \tag{1.13}$$

This leads to the EWSB that generates four fields W^a_μ $(a = 1, 2, 3)$ and B_μ. The physical fields are then defined as:

- two charged vector fields $W^\pm_\mu = \frac{1}{\sqrt{2}}(W^1_\mu \mp iW^2_\mu)$ with mass $m_W = \frac{gv}{2}$;

- one neutral vector field $Z_\mu = \cos\theta_w W^3_\mu - \sin\theta_w B_\mu$ with mass $m_Z = \frac{m_W}{\cos\theta_w}$;
- one photon field $A_\mu = \sin\theta_w W^3_\mu + \cos\theta_w B_\mu$ with mass $m_A = 0$.

As a consequence, a Higgs boson with mass $m_H = \sqrt{-2\mu^2} = \sqrt{2\lambda\mu}$ must exist to allow this mechanism to work correctly.

The last term in $\mathcal{L}_{SM}$ is the Yukawa Lagrangian that predicts the fermions masses through their interactions with the Higgs field:

$$\mathcal{L}_{Yukawa} = -Y^d_{ij}\overline{Q^I_{Li}}\phi D^I_{Rj} - Y^u_{ij}\overline{Q^I_{Li}}\widetilde{\phi}U^I_{Rj} - Y^l_{ij}\overline{L^I_{Li}}\widetilde{\phi}l^I_{Rj} + h.c. \tag{1.14}$$

where ϕ is the Higgs field, $\widetilde{\phi} = i\sigma_2\phi^*$, $Y^{u,d,l}$ are 3×3 complex matrices, i, j are generations labels, Q^I_L are left-handed quark doublets, D^I_R and U^I_R are respectively right-handed down-type and up-type quark singlets, L^I_L are left-handed lepton doublets and l^I_R are right-handed lepton singlets; all the doublets and the singlets are expressed in the weak-eigenstate basis. If we consider only quarks, when the EWSB happens we have that Eq. (1.14) yields the quarks mass terms: their physical states are obtained diagonalizing the Yukawa matrix Y^f using four unitary matrix $V^f_{L,R}$ following the relation

$$M^f_{diag} = \frac{v}{\sqrt{2}}V^f_L Y^f V^{f\dagger}_R, \tag{1.15}$$

where v is the VEV and $f = u, d$. After this brief overview regarding the SM, we will now discuss how $\mathcal{CP}$ symmetry is broken in the SM framework.

1.2 The CKM matrix

In the SM, $\mathcal{CP}$ symmetry is broken through complex phases in the Yukawa couplings of quark fields with the Higgs scalar field:

$$\mathcal{L}_{Yukawa} = -Y^d_{ij}\overline{Q^I_{Li}}\phi D^I_{Rj} - Y^u_{ij}\overline{Q^I_{Li}}\phi^\dagger U^I_{Rj} + h.c. \tag{1.16}$$

where Eq. (1.16) is the analogue of Eq. (1.14) neglecting the terms involving leptons. As a consequence of the diagonalisation of the Yukawa matrix Y^f, quarks weak-eigenstates and mass-eigenstates become mixed and the charged current interactions for quarks can be obtained through:

$$\mathcal{L}_{W^\pm} = \frac{g}{\sqrt{2}}\overline{U_{Li}}\gamma^\mu(V^u_L V^{d\dagger}_L)_{ij}D_{ij}W^+_\mu + h.c. \tag{1.17}$$

The product of the two V^f_L matrices contains the couplings of an up-type quark and a down-type quark to the charged W bosons and is called Cabibbo-Kobayashi-Maskawa (CKM) matrix [7, 29]:

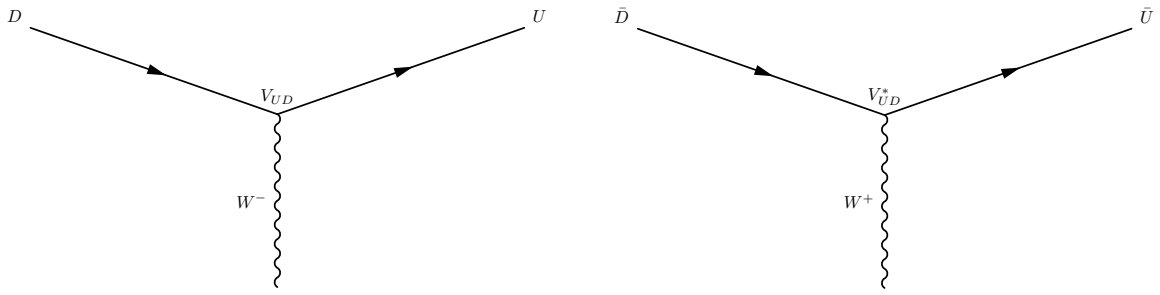

Figure 1.3: Feynman diagrams representing the charged-current interaction of an up-type and down-type quark. The left diagram represents the interaction involving a negative vector boson W^- while the right diagram represents its $\mathcal{CP}$ coniugate diagram, involving a W^+ boson. The coupling factor V_{UD}, deriving from V_{CKM}, is also reported.

$$V_{CKM} = V_L^u V_L^{d\dagger} = \begin{pmatrix} V_{ud} & V_{us} & V_{ub} \\ V_{cd} & V_{cs} & V_{cb} \\ V_{td} & V_{ts} & V_{tb} \end{pmatrix}. \tag{1.18}$$

We can draw Feynman diagrams representing the charged-current weak interactions between an up-type and down-type quark (see Fig. 1.3), where the elements of the CKM matrix modify the coupling strengths. It is now appropriate to describe the CKM matrix main properties before turning our attention on how it accounts for $\mathcal{CP}$ violation.

1.2.1 CKM matrix properties

One of the main features of the CKM matrix is its unitarity, required since processes involving quarks will not be invariant under a change of the quark field basis representation. This condition fixes the number of free parameters of the matrix. Indeed, a $N \times N$ unitary matrix contains $N(N-1)/2$ mixing angles and $N(N+1)/2$ complex phases. Moreover, we shall note that in the CKM matrix case, the Lagrangian allows to redefine the phase of each quark field obtaining:

$$\left.\begin{array}{l} U \to e^{-i\phi_U} U \\ D \to e^{-i\phi_D} D \end{array}\right\} V_{UD} \to e^{i\phi_U} V_{UD} e^{-i\phi_D} \tag{1.19}$$

This relations imply that $2N-1$ phases will cancel out, being unphysical. We can therefore compute the number of free parameters of a $N \times N$ complex matrix describing mixing between N quarks generations to be:

$$\underbrace{\frac{1}{2}N(N-1)}_{\text{Number of mixing angles}} + \underbrace{\frac{1}{2}(N-1)(N-2)}_{\text{Number of physical complex phases}} = (N-1)^2 \tag{1.20}$$

In the $N = 2$ case then we have one mixing angle and no complex phases, obtaining the Cabibbo matrix:

$$V_C = \begin{pmatrix} \cos\theta_C & \sin\theta_C \\ -\sin\theta_C & \cos\theta_C \end{pmatrix} \tag{1.21}$$

Using this matrix, it was possible to explain the suppression of flavor changing neutral currents (FCNC); moreover the nature of V_C opened the road to speculations about the existence of the charm quark [**?**, 30].

If we now analyze the case with $N = 3$, using Eq. 1.20 it follows that there will be three mixing angles and one complex phase as free parameters. The latter is the responsible for $\mathcal{CP}$ violation in weak interactions. The CKM matrix can be parameterized in many ways, among which one of the most famous is:

$$V_{CKM} \begin{pmatrix} c_{12}c_{13} & s_{12}c_{13} & s_{13}e^{-i\delta} \\ -s_{12}c_{23} - c_{12}s_{23}s_{13}e^{i\delta} & c_{12}c_{23} - s_{12}s_{23}s_{13}e^{i\delta} & s_{23}c_{13} \\ s_{12}s_{23} - c_{12}c_{23}s_{13}e^{i\delta} & -c_{12}s_{23} - s_{12}c_{23}s_{13}e^{i\delta} & c_{23}c_{13} \end{pmatrix} \tag{1.22}$$

where the notation $s_{ij} = \sin\theta_{ij}$ and $c_{ij} = \cos\theta_{ij}$ has been used and δ is the $\mathcal{CP}$ violating complex phase. We can choose the angles θ_{ij} to lie in the interval $[0, \pi/2]$ so that $s_{ij},\ c_{ij} > 0$: this means that the mixing between two quark generations i, j will vanish if the corresponding θ_{ij} is zero. In the particular case $\theta_{13} = \theta_{23} = 0$, the third generation will decouple and the CKM matrix will return to the form V_C of Eq. 1.21. The complex phase in the mixing matrix is a necessary condition for $\mathcal{CP}$ violation, but it is not sufficient. As noted in [31], another necessary condition is:

$$(m_t^2 - m_c^2)(m_t^2 - m_u^2)(m_c^2 - m_u^2)(m_b^2 - m_s^2)(m_b^2 - m_d^2)(m_s^2 - m_d^2) \times J_{CP} \neq 0 \tag{1.23}$$

where

$$J_{CP} = |\Im(V_{i\alpha}V_{j\beta}V_{i\beta}^*V_{j\alpha}^*)| \qquad (i \neq j, \alpha \neq \beta) \tag{1.24}$$

is the Jarlskog parameter ($\Im$ stands for the imaginary part). This relation descends from the fact that, according to Eq. (1.19), it would be possible to remove the CKM phase if any of two quarks with the same charge were degenerate in mass. As a consequence, $\mathcal{CP}$ violation origin is deeply connected with the quark mass hierarchy and with the number of fermion generations. Therefore, J_{CP} can be regarded as a measurement of the magnitude of $\mathcal{CP}$ violation present within the SM; moreover, the value of J_{CP} can be written, using the parametrization given in Eq. (1.22), as:

$$J_{CP} = s_{12}s_{13}s_{23}c_{12}c_{23}c_{13}^2 \sin\delta. \tag{1.25}$$

Experimental measurements give $J_{CP} = \mathcal{O}(10^{-5})$, which means that $\mathcal{CP}$ violation in the Standard Model is very small; various extension of the SM could enhance this value.

1.2.2 Measurements of CKM matrix elements

It is possible to determine CKM matrix elements through the following tree-level processes:

- $|V_{ud}|$ - Nuclear beta decays ($d \to ue\bar{\nu}_e$ transitions);
- $|V_{us}|$ - Semi-leptonic kaons decays $K \to \pi l\bar{\nu}$ ($s \to ul\bar{\nu}$ transitions);
- $|V_{ub}|$ - Exclusive and inclusive semi-leptonic B-hadron decays ($b \to ul\bar{\nu}$);
- $|V_{cd}|$ - Semi-leptonic D-hadron decays $D \to \pi l\bar{\nu}$ ($c \to dl\bar{\nu}$ transitions) and charm production from ν interaction with matter;
- $|V_{cs}|$ - Semi-leptonic D decays ($c \to sl\bar{\nu}$ transitions) and leptonic D_s decays ($D_s \to l\bar{\nu}$);
- $|V_{cb}|$ - Exclusive and inclusive semi-leptonic B decays to charm ($b \to cl\bar{\nu}$);
- $|V_{tb}|$ - Branching ratio of $t \to Wb$ decay (assuming CKM matrix unitarity) and single top-quark-production cross section.

For what concerns V_{td} and V_{ts}, their magnitude is not measurable using tree-level processes. Therefore, the optimal way to obtain their values is to extract $|V_{td}/V_{ts}|$ from $B^0 - \bar{B}^0$ and $B_s^0 - \bar{B}_s^0$ oscillations, which are described by box diagrams where u, c, t quarks circulate as virtual states. In Tab. (1.1) we have summarized the current values of the CKM matrix elements, while in Fig. 1.4 we report a graphical representation of the order of magnitude of quark transitions in the CKM matrix.

CKM matrix element	Experimental value
$\|V_{ud}\|$	0.97425 ± 0.00022
$\|V_{us}\|$	0.2252 ± 0.0009
$\|V_{ub}\|$	$(3.89 \pm 0.44) \times 10^{-3}$
$\|V_{cd}\|$	0.230 ± 0.011
$\|V_{cs}\|$	1.023 ± 0.036
$\|V_{cb}\|$	$(40.6 \pm 1.3) \times 10^{-3}$
$\|V_{td}\|$	$(8.4 \pm 0.6) \times 10^{-3}$
$\|V_{ts}\|$	$(38.7 \pm 2.1) \times 10^{-3}$
$\|V_{tb}\|$	0.88 ± 0.07

Table 1.1: CKM matrix elements current experimental values with their associated errors.

As can be clearly seen, transitions between quarks of the same generation correspond to V_{CKM} elements of $\mathcal{O}(1)$ while transitions between the first and the second and between

the second and the third generations are suppressed by a factor $\mathcal{O}(10^{-1})$ and $\mathcal{O}(10^{-2})$ respectively. Finally, transitions between the first and third generations are the most suppressed ($\mathcal{O}(10^{-3})$).

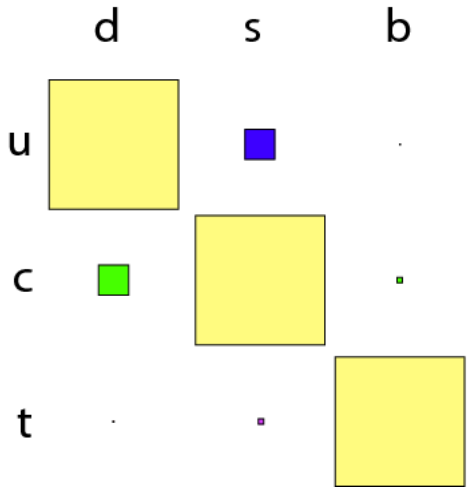

Figure 1.4: Pictorial representation of the order of magnitude of quarks transitions in the CKM matrix; the box sizes are proportional to the experimental V_{ij} measurements.

1.2.3 The Wolfenstein parametrization

Considering the measured magnitudes of the CKM matrix elements V_{ij}, we can note that:

$$s_{12} = 0.22 \gg s_{23} = \mathcal{O}(10^{-2}) \gg s_{13} = \mathcal{O}(10^{-3}) \ . \tag{1.26}$$

We can then introduce the Wolfenstein parametrization [32], defining:

$$s_{12} = \lambda = \frac{|V_{us}|}{\sqrt{|V_{ud}|^2 + |V_{us}|^2}} \ , \tag{1.27}$$

$$s_{23} = A\lambda^2 = \lambda \left| \frac{V_{cb}}{V_{us}} \right| \ , \tag{1.28}$$

and

$$s_{13} e^{-i\delta} = A\lambda^3(\rho - i\eta) = V_{ub} \ . \tag{1.29}$$

Having said that, now we can rewrite the CKM matrix presented in Eq. (1.22) as a power expansion of the parameter $\lambda = \sin\theta_C$, where θ_C is the Cabibbo angle:

$$V_{CKM} = \begin{pmatrix} 1 - \lambda^2/2 & \lambda & A\lambda^3(\rho - i\eta) \\ -\lambda & 1 - \lambda/2 & A\lambda^2 \\ A\lambda^3(1 - \rho - i\eta) & -A\lambda^2 & 1 \end{pmatrix} + \mathcal{O}(\lambda^4) \ . \tag{1.30}$$

It is also useful to continue the expansion in λ to the subsequent order, obtaining:

$$\begin{aligned}
V_{ud} &= 1-\frac{1}{2}\lambda^2-\frac{1}{8}\lambda^4+\mathcal{O}(\lambda^6), \quad V_{us}=\lambda+\mathcal{O}(\lambda^7), \quad V_{ub}=A\lambda^3(\rho-i\eta),\\
V_{cd} &= -\lambda+\frac{1}{2}A^2\lambda^5[1-2(\rho+i\eta)]+\mathcal{O}(\lambda^7), \quad V_{cs}=1-\frac{1}{2}\lambda^2-\frac{1}{8}\lambda^4(1+4A^2)+\mathcal{O}(\lambda^6),\\
V_{cb} &= A\lambda^2+\mathcal{O}(\lambda^8), \quad V_{td}=A\lambda^3\left[1-(\rho+i\eta)\left(1-\frac{1}{2}\lambda^2\right)\right]+\mathcal{O}(\lambda^7),\\
V_{ts} &= -A\lambda^2+\frac{1}{2}A\lambda^4[1-2(\rho+i\eta)]+\mathcal{O}(\lambda^6), \quad V_{tb}=1-\frac{1}{2}A^2\lambda^4+\mathcal{O}(\lambda^6). \qquad (1.31)
\end{aligned}$$

We will now stop for a moment to make some considerations about the relations written above:

- $V_{ub}\equiv A\lambda^3(\rho-i\eta)$ by definition does not receive any correction;
- $V_{us}=\lambda$ and $V_{cb}=A\lambda^2$ to a very high accuracy;
- the presence of a $\mathcal{CP}$ violating term, *i.e.* the imaginary term $i\eta$, in V_{cs} and V_{cb} is suppressed at least by a factor λ^6 and λ^8 respectively: this means that we expect small $\mathcal{CP}$ violation effects in the charm sector;
- contributions to $\mathcal{CP}$ violation from V_{td} and V_{ts} are at the level of λ^5 and λ^4 respectively.

To express V_{td} in a more concise way, it is useful to define:

$$\bar{\rho}\equiv\rho\left(1-\frac{1}{2}\lambda^2\right), \quad \bar{\eta}=\eta\left(1-\frac{1}{2}\lambda^2\right), \qquad (1.32)$$

allowing us to write:

$$V_{td}=A\lambda^3(1-\bar{\rho}-i\bar{\eta}). \qquad (1.33)$$

Finally we note that we can rewrite the Jarlskog parameter introduced in Eq. (1.24) as:

$$J_{CP}=\lambda^6A^2\eta, \qquad (1.34)$$

directly related to the $\mathcal{CP}$ violating term η.

1.2.4 CKM matrix unitary triangles

The unitarity of the CKM matrix implies that $V_{CKM}V_{CKM}^\dagger=V_{CKM}^\dagger V_{CKM}=\mathbb{I}$. This relation contains a set of twelve equations relating the matrix elements: six for the diagonal terms equal to 1 and six for the off-diagonal terms equal to 0. The equations

for the off-diagonal terms can be represented as triangles in the complex plane, all with same area $J_{CP}/2$:

$$\underbrace{V_{ud}V_{us}^*}_{\mathcal{O}(\lambda)} + \underbrace{V_{cd}V_{cs}^*}_{\mathcal{O}(\lambda)} + \underbrace{V_{td}V_{ts}^*}_{\mathcal{O}(\lambda^5)} = 0 \,, \tag{1.35}$$

$$\underbrace{V_{us}V_{ub}^*}_{\mathcal{O}(\lambda^4)} + \underbrace{V_{cs}V_{cd}^*}_{\mathcal{O}(\lambda^2)} + \underbrace{V_{ts}V_{tb}^*}_{\mathcal{O}(\lambda^2)} = 0 \,, \tag{1.36}$$

$$\underbrace{V_{ud}V_{ub}^*}_{(\rho+i\eta)A\lambda^3} + \underbrace{V_{cd}V_{cb}^*}_{-A\lambda^3} + \underbrace{V_{td}V_{tb}^*}_{(1-\rho-i\eta)A\lambda^3} = 0 \,, \tag{1.37}$$

$$\underbrace{V_{ud}^*V_{cd}}_{\mathcal{O}(\lambda)} + \underbrace{V_{us}^*V_{cs}}_{\mathcal{O}(\lambda)} + \underbrace{V_{ub}^*V_{cb}}_{\mathcal{O}(\lambda^5)} = 0 \,, \tag{1.38}$$

$$\underbrace{V_{cd}^*V_{td}}_{\mathcal{O}(\lambda^4)} + \underbrace{V_{cs}^*V_{ts}}_{\mathcal{O}(\lambda^2)} + \underbrace{V_{cb}^*V_{tb}}_{\mathcal{O}(\lambda^2)} = 0 \,, \tag{1.39}$$

$$\underbrace{V_{ud}^*V_{td}}_{(1-\rho-i\eta)A\lambda^3} + \underbrace{V_{us}^*V_{ts}}_{-A\lambda^3} + \underbrace{V_{ub}^*V_{tb}}_{(\rho+i\eta)A\lambda^3} = 0 \,. \tag{1.40}$$

In these equations we have underlined the value of each product at the leading order in λ as obtained from Eq. (1.30), representing the length of the corresponding triangle sides. We note that only the triangles represented by Eqs. (1.37) and (1.40) have sides of the same order of magnitude; in Figs. 1.5 (left) and 1.5 (right) there is a graphical representation of these triangles.

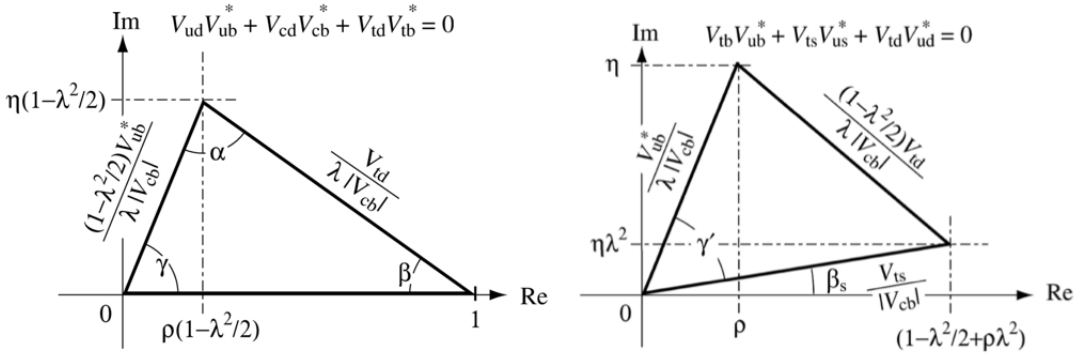

Figure 1.5: Unitary triangles drawn in the complex plane corresponding to Eq. (1.37) (left) and to Eq. (1.40) (right).

Focusing on the triangle represented by Eq. (1.37), using the expressions contained in Eq. (1.30), it is easy to see that the relation:

$$[(\rho + i\eta) + (-1) + (1 - \rho - i\eta)]A\lambda^3 = 0 \tag{1.41}$$

is satisfied, while to the next order, using Eqs. (1.31) and (1.32), one gets:

$$[(\bar{\rho}+i\bar{\eta})+(-1)+(1-\bar{\rho}-i\bar{\eta})]A\lambda^3+\mathcal{O}(\lambda^7)=0. \tag{1.42}$$

Dividing for the common factor $A\lambda^3$, we obtain the triangle represented in the left part of Fig. 1.5, usually called "The Unitary Triangle" (UT); its importance will be discussed later. We can now write the relations between the UT sides and the CKM matrix elements as:

$$R_b \equiv \sqrt{\bar{\rho}^2+\bar{\eta}^2} = \left(1-\frac{\lambda^2}{2}\right)\frac{1}{\lambda}\frac{|V_{ub}|}{|V_{cb}|}\ , \tag{1.43}$$

$$R_t \equiv \sqrt{(1-\bar{\rho})^2+\bar{\eta}^2} = \frac{1}{\lambda}\frac{|V_{td}|}{|V_{cb}|}\ , \tag{1.44}$$

while the following relations hold for the UT angles:

$$V_{ub} = A\lambda^3\left(\frac{R_b}{1-\lambda^2/2}\right)e^{-i\gamma}, \tag{1.45}$$

$$V_{td} = A\lambda^3 R_t e^{-i\beta}\ , \tag{1.46}$$

where the angles γ and β appear. We can finally write the angles relations with the CKM matrix elements in the following way:

$$\alpha \equiv \arg\left(-\frac{V_{td}V_{tb}^*}{V_{ud}V_{ub}^*}\right) = \arg\left(-\frac{1-\bar{\rho}-i\bar{\eta}}{\bar{\rho}+i\bar{\eta}}\right)\ , \tag{1.47}$$

$$\beta \equiv \arg\left(-\frac{V_{cd}V_{cb}^*}{V_{td}V_{tb}^*}\right) \equiv \phi_d/2 = \arg\left(\frac{1}{1-\bar{\rho}-i\bar{\eta}}\right)\ , \tag{1.48}$$

$$\gamma \equiv \arg\left(-\frac{V_{ud}V_{ub}^*}{V_{cd}V_{cb}^*}\right) = \arg(\bar{\rho}+i\bar{\eta})\ , \tag{1.49}$$

Considering now to the triangle described by Eq. (1.40), we find similar characteristics with respect to the UT described by Eq. (1.37); expanding Eq. (1.40) we obtain:

$$\left\{\left[1-\rho-i\eta-\lambda^2\left(\frac{1}{2}\rho-i\eta\right)\right]+\left[-1+\lambda^2\left(\frac{1}{2}-\rho-i\eta\right)\right]+(\rho+i\eta)\right\}A\lambda^3+\mathcal{O}(\lambda^7)=0 \tag{1.50}$$

If we divide for the common factor $A\lambda^3$, then we obtain a triangle with an apex placed in the point (ρ,η) instead of $(\bar{\rho},\bar{\eta})$, tilted by an angle:

$$\beta_s \equiv \phi_s/2 = \arg\left(\frac{V_{ts}V_{tb}^*}{V_{cs}V_{cb}^*}\right). \tag{1.51}$$

1.2.5 Determination of the UT parameters

Here we discuss the state of the art for what concerns the measurements of the UT parameters; more details about the adopted experimental techniques and the results can be found in Refs. [33, 34]. To determine the parameters, we need information from both experimental and theoretical sources; the experimental information about UT parameters can be obtained from the following measurements:

$|\mathbf{V_{ub}}|/|\mathbf{V_{cb}}|$: This ratio can be obtained through branching fraction measurements of semi-leptonic decays governed by $b \to ul\bar{\nu}$ and $b \to cl\bar{\nu}$ transitions. This quantity is proportional to the UT side between the γ and α angles, expressed as $\frac{(1-\lambda^2/2)V_{ub}^*}{\lambda|V_{cb}|}$.

$\mathbf{\Delta m_d}$: This parameter measures the $B^0 - \bar{B}^0$ mixing frequency. It is proportional to the magnitude of V_{td} and thus to the side of the UT between the α and β angles. However, the relation between Δm_d and V_{td} is plagued by large theoretical uncertainties, thus the quantity $\Delta m_s/\Delta m_d$ is also used as a constrain for the UT.

$\mathbf{\Delta m_s/\Delta m_d}$: Δm_s is the analogue quantity of Δm_d in $B_s^0 - \bar{B}_s^0$ mixing; its value is proportional to V_{ts}. The relations between $\Delta m_s/\Delta m_d$, V_{ts} and V_{td} contains some theoretical parameters that can be estimated more precisely with respect to the case of Δm_d.

β: This angle can be measured from time-dependent measurements of the $B^0 \to J/\psi K^0$ decays. Its relation with the $\bar{\rho}$ and $\bar{\eta}$ has been analyzed in the previous section.

$\varepsilon_{\mathbf{K}}$: This quantity is related to the size of $\mathcal{CP}$ violation in the neutral kaon system.

α: It is possible to measure this UT angle from $B \to \pi\pi$ and $B \to \rho\rho$ decays. Decay amplitudes and $\mathcal{CP}$ asymmetries of these channels are related to $V_{td}V_{tb}^*$ and $V_{ud}V_{ub}^*$ sides of the UT.

γ: This angle is determined through the $B \to D^{(*)}K^{(*)}$ decays, whose transitions are mediated by the V_{ub} and V_{cb} CKM elements.

$\sin(\mathbf{2}\beta + \gamma)$: Terms proportional to this quantity can be found in time-dependent decay rates of $B \to D^{(*)}\pi$ channels.

The determination of the UT parameters can be achieved, through the application of the Bayes theorem. The unknowns $\bar{\rho}$ and $\bar{\eta}$ are related to a set of N observables x_i by M relations $c_j = \phi_j(x_1, \ldots, x_N, \bar{\rho}, \bar{\eta})$, with $j \in \{1, M\}$. The joint p.d.f. for $\bar{\rho}$ and $\bar{\eta}$ can be found using the Bayes theorem; indeed, the conditional distribution $\mathbf{f}$ for $\bar{\rho}$ and $\bar{\eta}$ given the measurements x_i and the constrain relations c_j can be written as:

$$\mathbf{f}(\bar{\rho}, \bar{\eta}|x_1, \ldots, x_N, c_1, \ldots, c_M) \propto f(c1, \ldots, c_M|\bar{\rho}, \bar{\eta}, x_1, \ldots, x_N) \cdot f_0(\bar{\rho}, \bar{\eta}) \cdot g_0(x_1, \ldots, x_N), \quad (1.52)$$

where the f on the right side is the probability to obtain the constraint relations $c_1, \ldots, c_M$ for a given set of values $\bar{\rho}$, $\bar{\eta}$ and measurements x_i , f_0 is the *a priori* p.d.f. for $\bar{\rho}$, $\bar{\eta}$ and finally g_0 is the *a priori* p.d.f. for the observables $x_1, \ldots, x_N$, determined from experimental measurements and theoretical calculations. We can now write the following relation:

$$f(c1, \ldots, c_M|\bar{\rho}, \bar{\eta}, x_1, \ldots, x_N) = \prod_{j=1}^{M} \delta(c_j - \phi_j(x_1, \ldots, x_n, \bar{\rho}, \bar{\eta})) \tag{1.53}$$

where the δ stands for the Dirac delta function. Then, the joint p.d.f. for $\bar{\rho}, \bar{\eta}$ obtained in Eq. (1.52) becomes:

$$\mathbf{f}(\bar{\rho}, \bar{\eta}|x_1, \ldots, x_N, c_1, \ldots, c_M) \propto \prod_{j=1}^{M} \delta(c_j - \phi_j(x_1, \ldots, x_n, \bar{\rho}, \bar{\eta})) \cdot f_0(\bar{\rho}, \bar{\eta}) \cdot \prod_{i=1}^{N} f_i(x_i) \tag{1.54}$$

in which the $f_i(x_i)$ are the distributions of the observables x_i. To determine the joint p.d.f. for $\bar{\rho}$ and $\bar{\eta}$ one must then generate their values, weighted by the constraint relations, through the use of Monte Carlo technique. We report in Tab. 1.2 the input values used and the best values obtained for the parameters mentioned at the beginning of this section. The full fit results for the $\bar{\rho}$ and $\bar{\eta}$ parameters result to be:

$$\bar{\rho} = 0.132 \pm 0.020, \qquad \bar{\eta} = 0.358 \pm 0.012. \tag{1.55}$$

Parameter	Input value	Fit result
$\lvert V_{ub}\rvert$	0.00375 ± 0.00046	0.00362 ± 0.00012
$\lvert V_{cb}\rvert$	0.0409 ± 0.001	0.04172 ± 0.00056
Δm_d	(0.51 ± 0.004) ps^{-1}	(0.507 ± 0.005) ps^{-1}
Δm_s	(17.768 ± 0.024) ps^{-1}	(17.768 ± 0.024) ps^{-1}
α	$(90.9 \pm 8.0)^\circ$	$(87.7 \pm 3.3)^\circ$
$\sin(2\beta)$	0.680 ± 0.023	0.695 ± 0.021
$\cos(2\beta)$	0.87 ± 0.13	0.719 ± 0.021
γ	$(-109.9 \pm 7.1)^\circ$ and $(70.1 \pm 7.1)^\circ$	$(70.3 \pm 3.5)^\circ$
$2\beta + \gamma$	$(-89 \pm 54)^\circ$ and $(90 \pm 54)^\circ$	$(114.2 \pm 3.4)^\circ$
$\lvert\varepsilon_K\rvert$	$(2.22994 \pm 0.0104974) \times 10^{-3}$	$(2.22854 \pm 0.00998004) \times 10^{-3}$

Table 1.2: Full fit values obtained for the parameters listed at the beginning of this section using the procedure described in Ref. [35].

Finally, for completeness, we report a graphical representation of the allowed parameter values in Fig. 1.6.

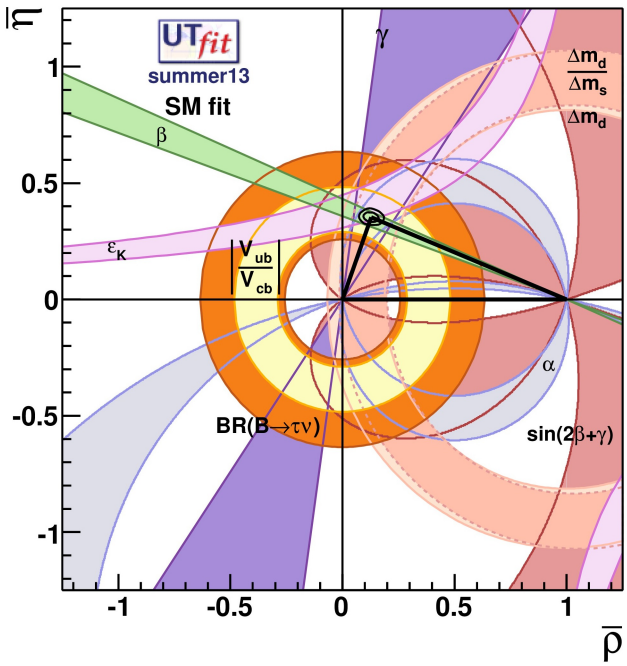

Figure 1.6: Graphical representation of the allowed parameters ranges as given from the full fit procedure described in Ref. [35]. The 68% and 95% contours for $\bar{\rho}$ and $\bar{\eta}$ parameters are also displayed.

1.3 Charmless two-body hadronic decays of the Λ_b^0 baryon

Rare B decays involving flavor changing neutral current (FCNC) transitions are of great interest to look for possible hints of new physics beyond the SM. In the SM, the FCNC transitions arise only at one-loop level, thus providing a sensitive test for the investigation of the gauge structure of the SM. Moreover, the study of weak decays of bottom hadrons can provide valuable information on the CKM matrix due to the fact that b decays involve five matrix elements (V_{cb}, V_{ub}, V_{td}, V_{ts} and V_{td}).

The weak decays concerning heavy baryons containing a b quark may provide important clues on flavor changing (FC) currents beyond the SM in a complementary way with respect to B mesons decays. Furthermore, since $\mathcal{CP}$ violation has been measured in B^0 and B_s^0 meson decays involving $b \to s$ transitions [15], one expects that there could be deviations also in the Λ_b^0 decays involving the same quark transitions. Therefore, the study of rare Λ_b^0 decays is of fundamental importance in order to establish possible signals of $\mathcal{CP}$ violation that could represent hints for NP.

The Feynman diagrams describing such transitions can be divided into two groups: tree-level topologies and penguin (or loop-level) topologies. In the case of the $\Lambda_b^0 \to p\pi^-$ and $\Lambda_b^0 \to pK^-$ the diagrams involved can be classified in three categories:

- $b \to d(s)$ transitions mediated by tree-level topologies;
- $b \to d(s)$ transitions mediated by loop-level QCD topologies;
- $b \to d(s)$ transitions mediated by loop-level EW topologies.

The different Feynman diagrams referring to the topologies listed above are shown in Fig. 1.7.

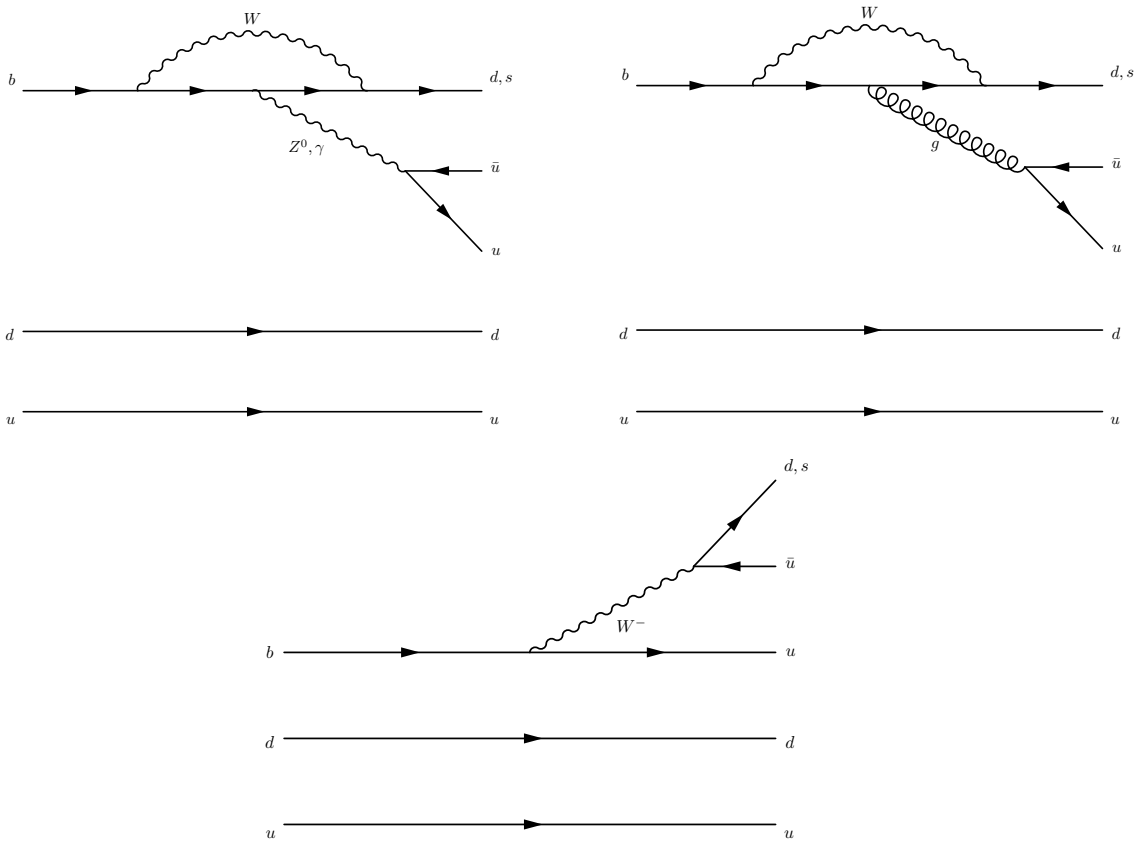

Figure 1.7: Feynman diagrams representing the penguin EW topology (top-left), the penguin QCD topology (top-right) and the tree-level topology (bottom) contributing to $\Lambda_b^0 \to pK^-$ ($b \to su\bar{u}$ transition) and $\Lambda_b^0 \to p\pi^-$ decays ($b \to du\bar{u}$ transition).

The standard theoretical framework used to study the non-leptonic Λ_b^0 decays is based on the effective Hamiltonian approach, which allows us to separate the short- and long-distance contributions through the Wilson operator product expansion. Since a detailed treatment of this approach is beyond the scope of this thesis, we will show only the essential features of this method in the next section.

1.3.1 Effective Hamiltonian approach

To fully describe the weak decays of hadrons, it is also necessary to consider the strong interaction binding together the constituents quarks. Due to the QCD asymptotic freedom, it is possible to treat short-distance corrections, *i.e.* the hard gluons contributions at energies of the order of $\mathcal{O}(M_W)$ down to hadronic scales ≥ 1 GeV, in perturbation theory. The theoretical framework adopted to exploit such property is the so called Operator Product Expansion (OPE) [36, 37].

This approach allows to write the effective Hamiltonian for the hadronic charmless Λ_b^0 decays as:

$$\mathcal{H}_{eff} = \frac{G_F}{\sqrt{2}} \left\{ V_{ub}V_{uq}^*[c_1(\mu)O_1^u(\mu) + c_2(\mu)O_2^u(\mu)] - V_{tb}V_{tq}^* \sum_{i=3}^{10} c_i(\mu)O_i(\mu) \right\} + h.c. \quad (1.56)$$

where $q = d, s$ and $c_i(\mu)$ are the Wilson coefficients evaluated at the renormalization scale μ. The operators O_{1-10} are given by the expressions:

$$\begin{aligned}
O_1^u &= (\bar{u}b)_{V-A}(\bar{q}u)_{V-A}, \\
O_2^u &= (\bar{u}_\alpha b_\beta)_{V-A}(\bar{q}_\beta u_\alpha)_{V-A}, \\
O_{3(5)} &= (\bar{q}b)_{V-A} \sum_{q'} (\bar{q}'q')_{V-A(V+A)}, \\
O_{4(6)} &= (\bar{q}_\alpha b_\beta)_{V-A} \sum_{q'} (\bar{q}'_\beta q'_\alpha)_{V-A(V+A))}, \\
O_{7(9)} &= \frac{3}{2}(\bar{q}b)_{V-A} \sum_{q'} e_{q'}(\bar{q}'q')_{V+A(V-A)}, \\
O_{8(10)} &= \frac{3}{2}(\bar{q}_\alpha b_\beta)_{V-A} \sum_{q'} e_{q'}(\bar{q}'_\beta q'_\alpha)_{V+A(V-A)}
\end{aligned} \quad (1.57)$$

where $O_{1,2}$ are the tree-level current-current operators, O_{3-6} are the QCD penguin operators, O_{7-10} are the EW penguin operators and $(\bar{q}_1 q_2)_{(V\pm A)}$ denote the usual $(V \pm A)$ currents. The sum over q' runs over all the quark fields active at the scale $\mu = \mathcal{O}(m_b)$, *i.e.* $(q' \in u, d, c, s, b)$.

The $\Lambda_b^0 \to p\pi^-$ decay proceeds at tree-level through $b \to du\bar{u}$ and at the loop-level via $b \to d$ penguin diagrams. We recall the following relations, in terms of the Wolfenstein parametrization:

$$V_{ub}V_{ud}^* \simeq A\lambda^3(\rho - i\eta), \qquad V_{tb}V_{td}^* \simeq A\lambda^3(1 - \rho + i\eta). \quad (1.58)$$

Note that the equations above are of the same order of magnitude and so we can conclude the $\Lambda_b^0 \to p\pi^-$ decay is tree dominated, as the penguin contributions are suppressed due

to the smallness of the penguin coefficients. Turning our attention to the $\Lambda_b^0 \to pK^-$ decay, we observe that this decay proceeds at the tree level through $b \to su\bar{u}$ and via $b \to s$ penguin diagrams. In this case we note that:

$$V_{ub}V_{us}^* = A\lambda^4(\rho - i\eta), \qquad V_{tb}V_{ts}^* = -A\lambda^2 \tag{1.59}$$

and so it is evident that the magnitude of $V_{tb}V_{ts}^*$ is almost two order of magnitudes larger than that of $V_{ub}V_{us}^*$. For this reason the $\Lambda_b^0 \to pK^-$ decay is dominated by the QCD penguin diagrams.

To conclude, we note that using the unitarity of the CKM matrix ($V_{tr}^*V_{tb} = -V_{ur}^*V_{ub} - V_{cr}^*V_{cb}$), we can write Eq. (1.56) in a more convenient way:

$$\mathcal{H}_{eff} = \frac{G_F}{\sqrt{2}} \left\{ \sum_{j=u,c} V_{jr}^* V_{jb} \left[\sum_{k=1}^{2} c_k(\mu) O_k^{jr} + \sum_{k=3}^{10} c_k(\mu) O_k^r \right] \right\}. \tag{1.60}$$

that will prove to be useful in the next section.

1.3.2 Decay amplitudes

Using the formalism just described we now can write the matrix element of a generic $\bar{H}_b \to \bar{f}$ decay:

$$\begin{aligned} A(\bar{H}_b \to \bar{f}) &= \langle \bar{f}|\mathcal{H}_{eff}|\bar{H}_b\rangle = \\ &= \frac{G_F}{\sqrt{2}} \left\{ \sum_{j=u,c} V_{jr}^* V_{jb} \left[\sum_{k=1}^{2} c_k(\mu) \langle \bar{f}|O_k^{jr}|\bar{H}_b\rangle + \sum_{k=3}^{10} c_k(\mu) \langle \bar{f}|O_k^r|\bar{H}_b\rangle \right] \right\}, \end{aligned} \tag{1.61}$$

while for its $\mathcal{CP}$ coniugate decay we have:

$$\begin{aligned} A(H_b \to f) &= \langle f|\mathcal{H}_{eff}^\dagger|H_b\rangle = \\ &= \frac{G_F}{\sqrt{2}} \left\{ \sum_{j=u,c} V_{jr}^* V_{jb} \left[\sum_{k=1}^{2} c_k(\mu) \langle f|O_k^{jr\dagger}|H_b\rangle + \sum_{k=3}^{10} c_k(\mu) \langle f|O_k^{r\dagger}|H_b\rangle \right] \right\}. \end{aligned} \tag{1.62}$$

Using the strong interaction invariance under $\mathcal{CP}$ and noting that $(\mathcal{CP})^\dagger(\mathcal{CP}) = \mathbb{I}$ we can write the following relations:

$$\begin{aligned} (\mathcal{CP})O_k^{jr}(\mathcal{CP})^\dagger &= O_k^{jr}\ , \\ (\mathcal{CP})O_k^{r}(\mathcal{CP})^\dagger &= O_k^{r}\ , \\ (\mathcal{CP})|f\rangle &= e^{i\phi_f}|\bar{f}\rangle\ , \\ (\mathcal{CP})|H_b\rangle &= e^{i\phi_{H_b}}|\bar{H}_b\rangle\ . \end{aligned} \tag{1.63}$$

The equations above allow us to rewrite Eq. (1.62) in the following way:

$$\begin{aligned} A(H_b \to f) &= e^{i(\phi_{H_b}-\phi_f)}\frac{G_F}{\sqrt{2}} \times \\ &\times \left\{ \sum_{j=u,c} V_{jr}^* V_{jb} \left[\sum_{k=1}^{2} c_k(\mu) \langle f | O_k^{jr\dagger} | H_b \rangle + \sum_{k=3}^{10} c_k(\mu) \langle f | O_k^{r\dagger} | H_b \rangle \right] \right\} . \end{aligned} \quad (1.64)$$

We then have that:

$$\begin{aligned} A(\bar{H}_b \to \bar{f}) &= e^{i\psi_1}|A_1|e^{i\delta_1} + e^{i\psi_2}|A_2|e^{i\delta_2} \\ A(H_b \to f) &= e^{i(\phi_{H_b}-\phi_f)} \times \left(e^{i\psi_1}|A_1|e^{i\delta_1} + e^{i\psi_2}|A_2|e^{i\delta_2} \right) , \end{aligned} \quad (1.65)$$

where $\psi_{1,2}$ denotes the $\mathcal{CP}$-violating phase coming from the CKM elements $V_{jr}V_{jb}^*$ and $|A_{1,2}|e^{i\delta 1,2}$ are the $\mathcal{CP}$- conserving strong amplitudes coming from:

$$|A|e^{i\delta} \sim \sum_k \underbrace{c_k(\mu)}_{\text{perturbative QCD}} \times \underbrace{\langle \bar{f} | c_k(\mu) | \bar{H}_b \rangle}_{\text{non-perturbative QCD}} . \quad (1.66)$$

Chapter 2

LHC and the LHCb experiment

LHCb [41] is one of the four major experiments operating at the Large Hadron Collider (LHC) at CERN, located near Geneva, across the border between France and Switzerland. In this chapter we will give a short description of the LHC collider, followed by a detailed description of the LHCb detector.

2.1 The Large Hadron Collider

The LHC [42] is a two-ring-hadron accelerator and collider, installed inside a 27 km long tunnel (the same where previously the LEP collider was installed), placed 100 m underground, as shown in Fig. 2.1. The accelerator is designed to collide protons up to a center-of-mass energy of 14 TeV, with an instantaneous luminosity of 10^{34} cm^{-2}s^{-1}, while heavy-ion collisions (Pb-Pb) happen at a center-of-mass energy of 2.8 TeV per nucleon, with a peak luminosity of 10^{27} cm^{-2}s^{-1}. This energies will be reached after the restart of the LHC machine in 2015, once the first long shutdown will be over. Until now, the LHC has collided protons at an energy of $\sqrt{s} = 7$ TeV in 2010-2011 and $\sqrt{s} = 8$ TeV in 2012.

The protons used in the collisions are obtained from ionized hydrogen atoms, once their electrons have been stripped off. As it is not possible to directly accelerate protons from their quasi-rest conditions up to 7 TeV, it is necessary to pre-accelerate them through a complex of machines, represented in Fig. 2.2. First, protons are injected in Linac2, a linear accelerator that provides the Proton Synchrotron Booster (PSB) with proton bunches of 50 MeV energy. The PSB can accelerate protons up to 1 GeV; after this, the particles are injected in the Proton Synchrotron (PS), where they reach an energy of 26 GeV. Then, the PS passes them to the Super Proton Synchrotron (SPS), where they are accelerated for the last time up to an energy of 450 GeV, before being injected into the LHC via two tunnels, called T12 and T18, shown in Fig. 2.2.

Once in the collider, the protons are kept in their orbits thanks to a magnetic field

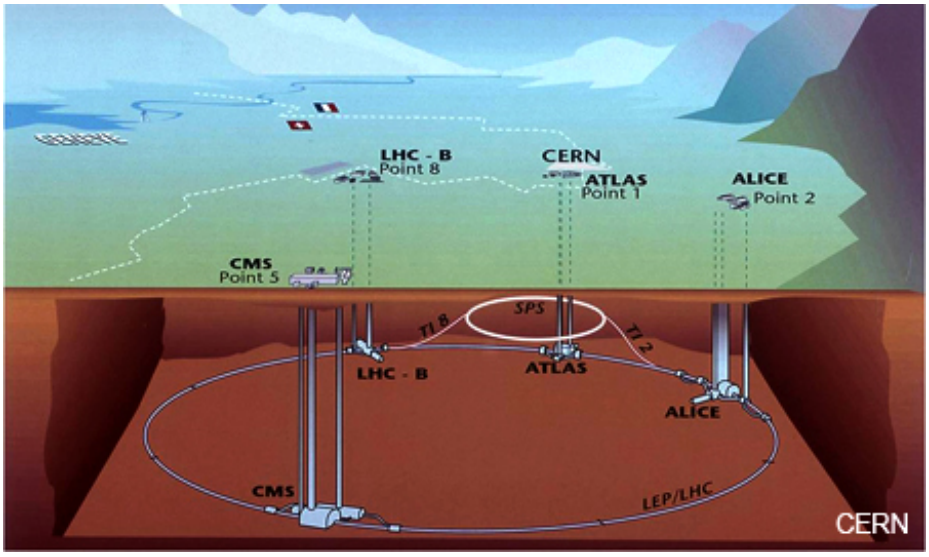

Figure 2.1: Schematic view of the LHC collider. As previously said, the collider is 100 m underground and there are 4 access points to the main experiments (ALICE, ATLAS, CMS, LHCb).

with an intensity of 8.34 T. To reach such a strong magnetic field it is mandatory to use superconducting magnetic dipoles, that operate at a temperature of 1.9 K (-271.3°C). At the nominal operation regime, the LHC rings store 2808 proton bunch per ring, each of them containing 1.1^{11} protons and colliding with a frequency of 40 MHz (*i.e.* the bunches collide every 25 ns).

The LHC has performed very well in the three years of data taking, allowing the LHCb experiment to collect more than 3 fb^{-1} of data (see Fig. 2.3), with an efficiency of well over 90%, as can be seen in Fig. 2.4. This implies that an unprecedented sample of D and B hadrons has been collected, allowing the LHCb collaboration to perform high precision measurements, improving previous results coming from the BaBar, Belle and CDF collaborations and allowing the discovery of new effects in the charm and beauty sector.

2.2 The LHCb experiment

The LHCb experiment is designed to exploit the great production cross section of $b\bar{b}$ pairs in pp collision at the LHC energies, measured at a center of mass energy of 7 TeV to be $\sigma_{b\bar{b}} = (284 \pm 20 \pm 49)\ \mu$b [43]. This fact and the excellent performances of the LHCb detector have already allowed precision studies of flavor physics which are expected to be improved in the future. The same characteristics that make LHCb a perfect experiment for b physics are ideal for the study of c physics as well, also because

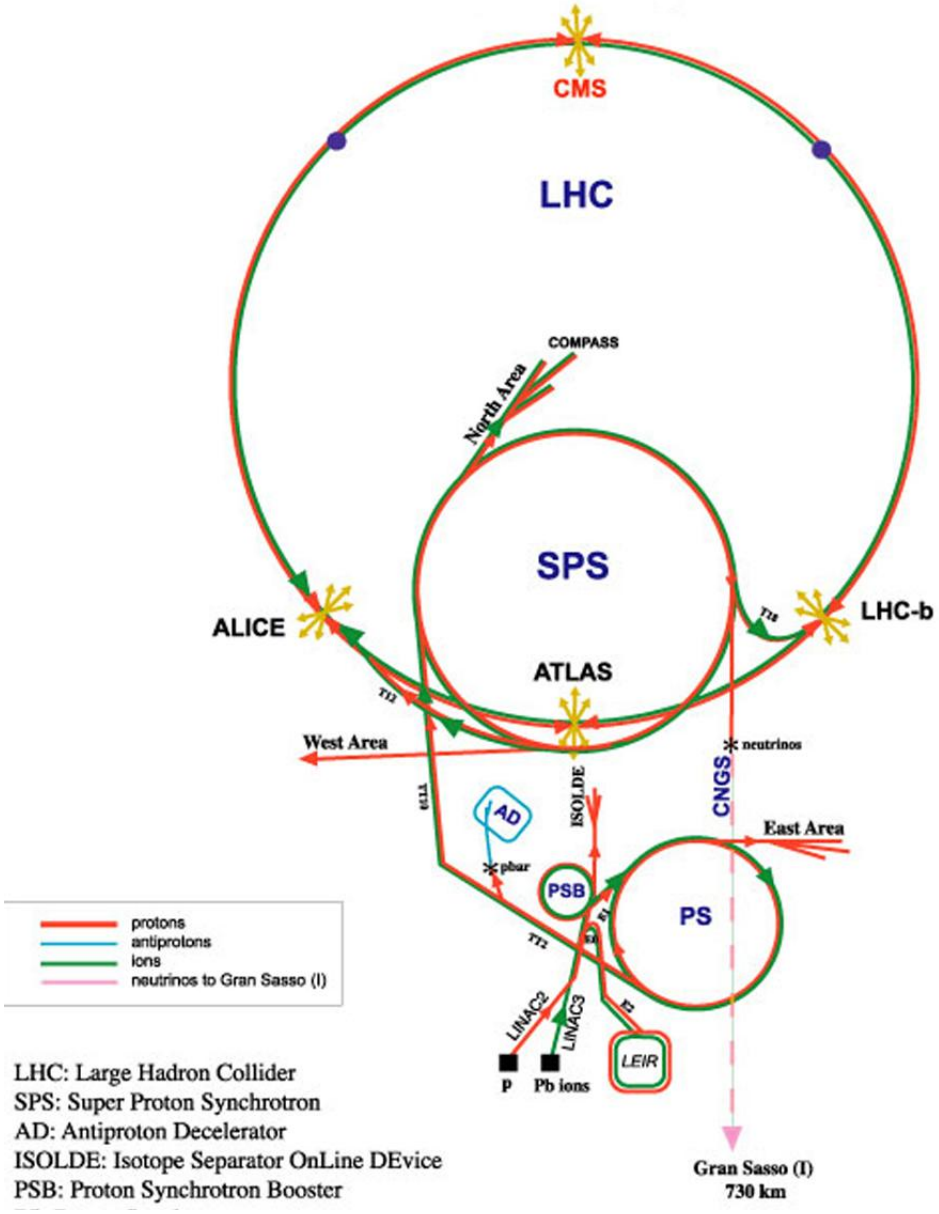

Figure 2.2: Scheme representing the various machines employed to pre-accelerate the protons that will be injected in the LHC. The protons are injected in the LINAC2 to begin their acceleration and then they enter the PSB, the PS and finally the SPS before being ready to be accelerated by the LHC.

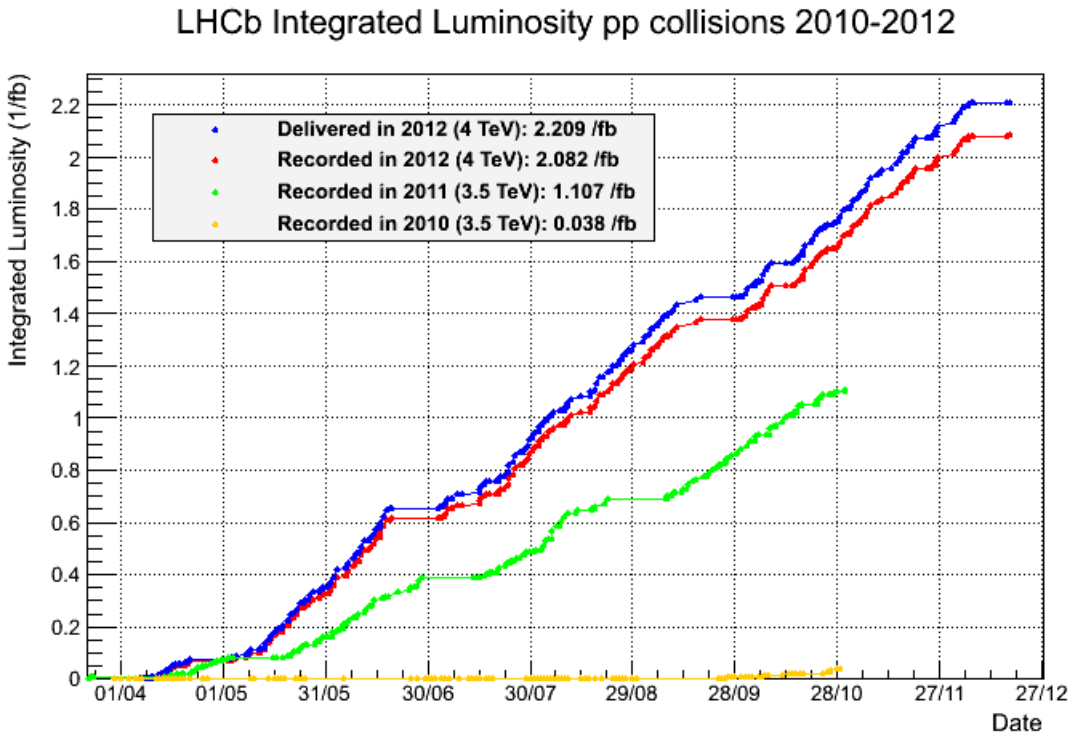

Figure 2.3: Plot showing the integrated luminosity delivered by the collider in the 2012 and recorded by LHCb in the same year. For completeness, the integrated luminosities recorded in 2010 and 2011 are also reported.

the $c\bar{c}$ production cross section is even larger than the $b\bar{b}$ production cross section, namely $\sigma_{c\bar{c}} = (6.1 \pm 0.93)\ mb$ [44].

The LHCb physics program is aimed at the search of NP beyond the SM, with an approach that is somewhat complementary to that used by the ATLAS and CMS collaborations. Indeed, while the latter experiments are designed to measure high p_T decay products that could indicate the production of new particles, the LHCb experiment is trying to measure the existence of such new particles by means of their virtual quantum effects. In particular, the main studies are devoted to the measurements of $\mathcal{CP}$ violation in b and c hadrons and to the determination of various branching ratios regarding B hadrons. Furthermore, the research is also active in other fields, like the search for exotic hadrons, studies of double parton scattering and production measurements of electroweak gauge boson in the forward kinematic region.

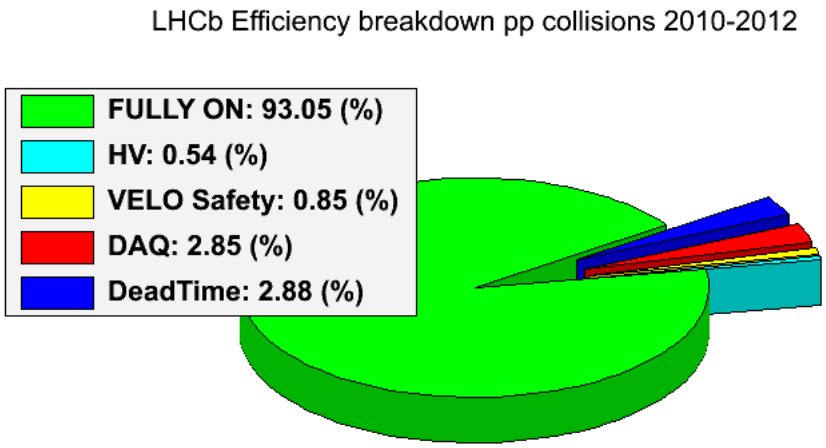

Figure 2.4: Pie chart showing the LHCb efficiency during the three years of pp collisions.

2.3 The LHCb detector

Due to the average imbalance in momentum of two partons that collide during a pp interaction, the b quarks are produced as strongly boosted along the beam-line. As a consequence, the B hadrons at the LHC are produced preminently in the same forward or backward region and with a small angle with respect to the beam direction. For that reason, in order to take advantage of this peculiarity, the LHCb detector, in contrast to other LHC detectors, is designed as a forward spectrometer, as can be seen in Fig. 2.5. Its geometrical acceptance lies between 10 and 300 mrad in the horizontal plane and between 10 and 250 mrad in the vertical plane: the difference in the acceptances is justified by the fact that the horizontal plane is also the bending plane for the charged particles deflected by the dipole magnetic field of LHCb. Therefore, the detector can measure particles that lie in a pseudo-rapidity[1] (η) range between 1.8 and 4.9. To pursue the LHCb physics program, the detector must have the following characteristics:

- a great precision in the reconstruction of the interaction vertices and of the B

[1]The pseudo-rapidity is defined as

$$\eta = -\ln\tan\left(\frac{\theta}{2}\right) = \frac{1}{2}\ln\frac{|\vec{p}|+p_L}{|\vec{p}|-p_L}$$

where θ is the angle between the particle and the beam axis and p_L is the longitudinal momentum

hadrons decay vertices, because to measure the neutral B mesons oscillations it is fundamental to have a suitable proper-time resolution;

- an excellent PID system in order to discriminate between charged pions, charged kaons and protons with momentum between few GeV/c up to 100 GeV/c. Moreover, to analyze final states containing leptons, there is the need to have also an optimal PID of muons and electrons.

- The invariant mass resolution must be as small as possible in order to discriminate the signals from the combinatorial background and in order to distinguish between B^0 and B_s^0 decays. For these reasons, the momentum of charged tracks must be measured with a relative precision of $\sim 10^{-3}$;

- because the production cross sections of c and b quarks together account for nearly 10% of the total pp inelastic cross section at $\sqrt{s} = 7$ TeV (*i.e.* one collision out of ten produces D or B hadrons), the trigger system must be able to reject a very large part of the background, in order to have manageable data-sample. To achieve this, the LHCb trigger is organized in multiple levels, each of them more specialized (but slower) than the previous;

- the large amount of data collected by the experiment requires efficient and reliable computing resources, both needed for the processing and the storage of data.

The LHCb detector is composed by two detector categories:

Tracking systems The VELO (VErtex LOcator) is a system that identifies the secondary interaction vertex and it is placed around the interaction point of the two beams. The Trigger Tracker (TT) is placed behind the first RICH and his task is the reconstruction of the particle tracks and the measurement of the particle momentum, together with the three tracking stations (T1, T2 and T3) placed after the Magnet.

Particle identification systems This part of the detector is composed of two Ring Imaging Cherenkov detectors, two calorimeters and a muon detector. The first Cherenkov detector, called RICH1, is placed immediately after the VELO, while the second, called RICH2, is after the Tracking Stations. These two detectors have the task to discriminate between the various types of particles that cross them. The Electromagnetic and Hadronic calorimeters (respectively called ECAL and HCAL) measure the energy of the particles that hit them (the ECAL measures e^+, e^- and γ energies, while the HCAL measures the hadrons energies). Finally we have the muon detector, composed by five MultiWire Proportional Chambers (MWPCs), spaced with iron filters, to measure the μ energies.

We will now give a detailed description of all the sub-detectors just mentioned.

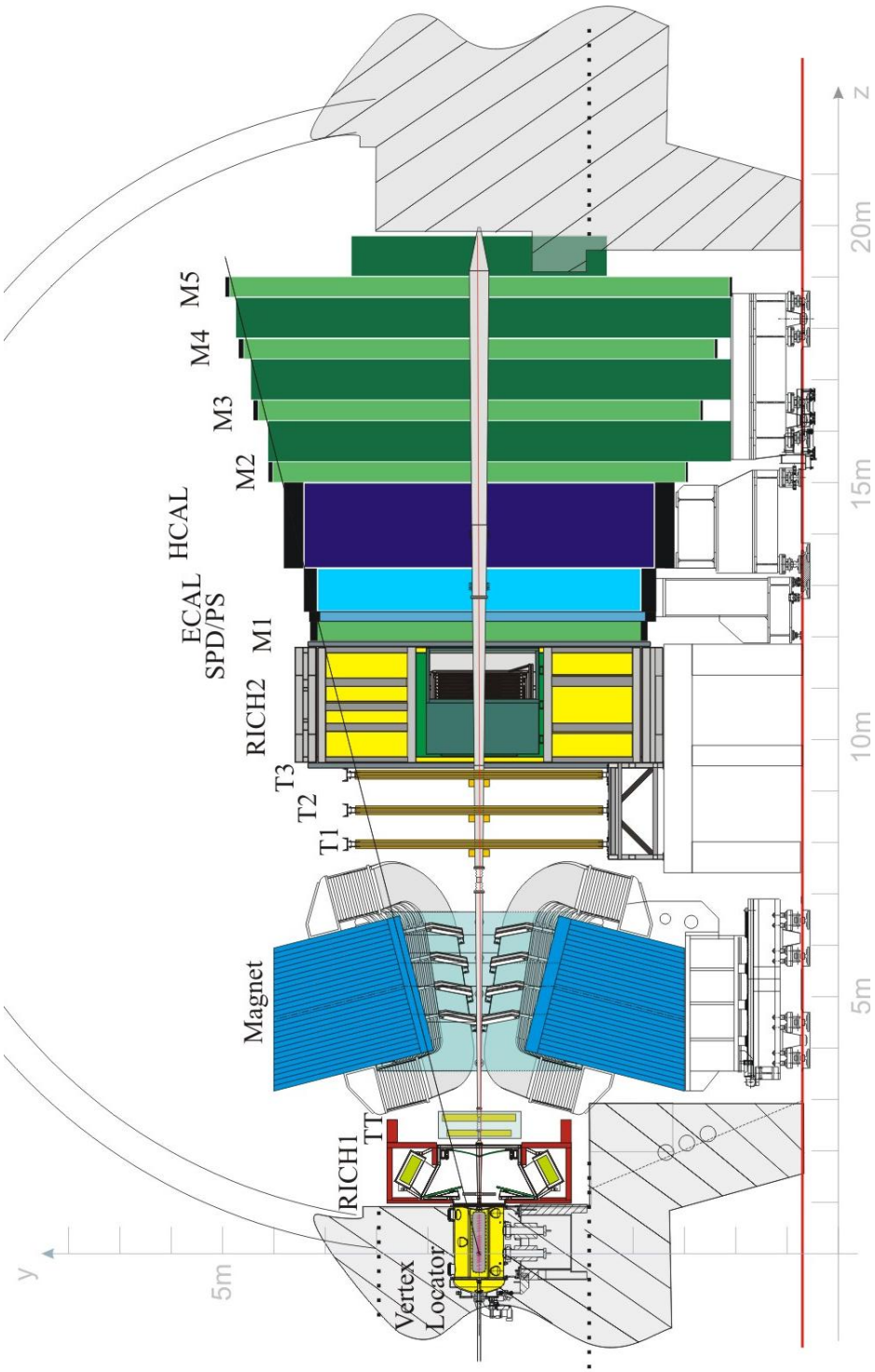

Figure 2.5: Scheme representing the LHCb detector. From left to right all the sub-detectors are visibles: VELO, RICH1, TT, Magnet, Tracking Stations, RICH2, Electromagnetic Calorimeter (ECAL), Hadronic Calorimeter (HCAL) and Muon Stations (M1-M5).

2.4 The LHCb tracking system

The tracking system is devoted to identify the interaction vertex, reconstruct the trajectories of charged particles and measure their momentum exploiting a magnetic field to bend them. The first task is accomplished by the VELO, that is also used for the track reconstruction, together with the Trigger Tracker and the three tracking stations. Finally, a warm magnetic dipole generates the magnetic field.

2.4.1 The Vertex Locator

B hadrons at LHCb have a mean distance of flight of about 1 cm. This is an important signature of B hadrons: the presence of a secondary vertex well displaced from the proton-proton primary vertex. For this reason and also due to the high track multiplicity in LHC collisions, it is imperative to have a vertex locator with a micrometric precision in order to select signal events and reject most of the background.

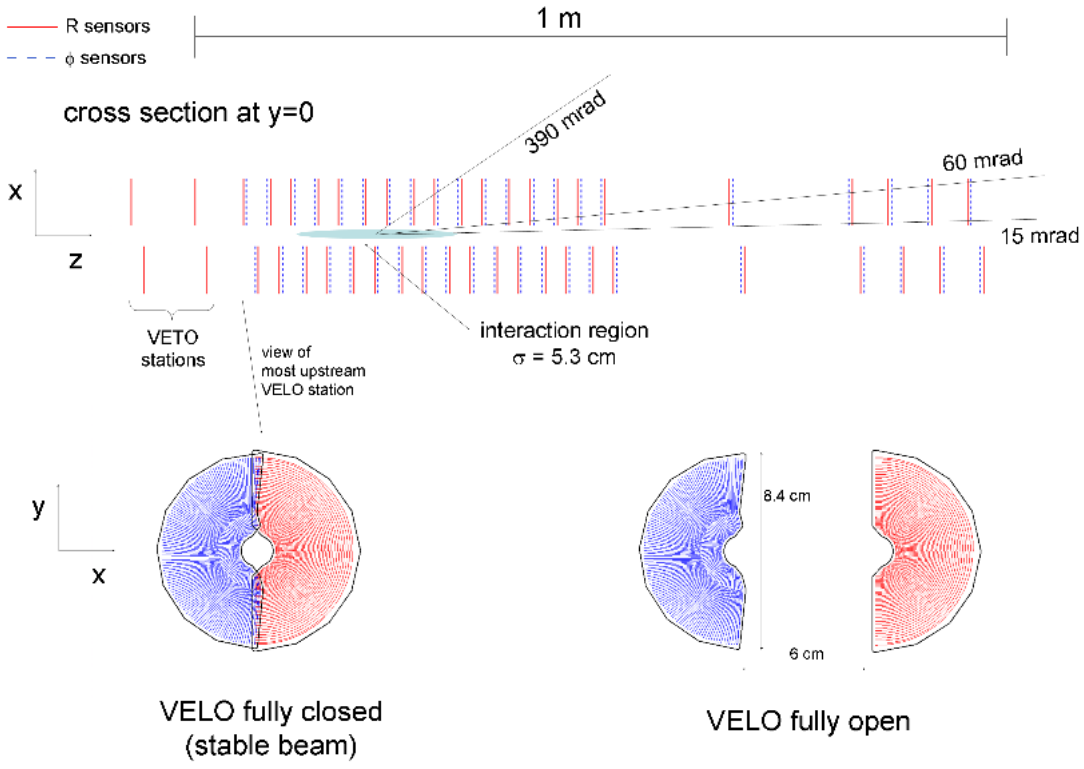

Figure 2.6: Top view of the VELO silicon sensors, with the VELO in the fully closed position (top). Frontal view of the modules in the closed (bottom left) and open positions (bottom right).

The VELO [45] is composed of 21 circular silicon modules, installed perpendicularly along the beam line, as shown in Fig. 2.6. Each silicon modules is divided in two halves, to allow the positioning of the VELO during the data taking phase (closed) or during the beam stabilization phase (open), as can be seen in the bottom part of Fig. 2.6. For this reason, the modules are installed on a movable device placed inside a vacuum vessel; it is important to note that the two halves of a module partly overlap in the closed VELO configuration (as shown in the bottom left part of Fig. 2.6), in order to achieve a better geometrical coverage. The modules are composed of two planes of 220 μm thick silicon microstrip sensors able to measure the distance from the beam (radial distance, R) and the polar angle ϕ of hits generated by the ionizing particles that cross the VELO. The structure of such R and ϕ sensors is reported in Fig. 2.7. The third coordinate z is simply measured knowing what modules give a signal for a particular particle hit.

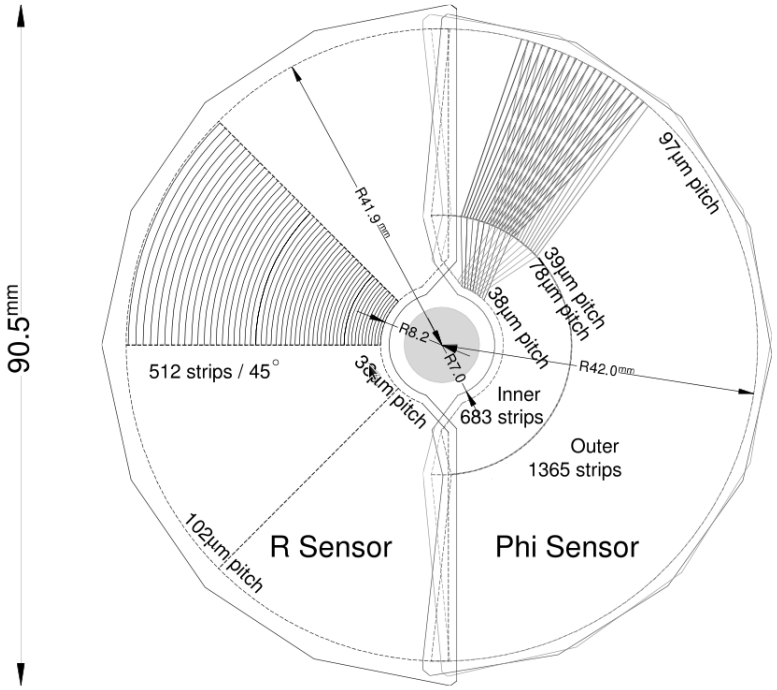

Figure 2.7: Geometry of the R (left) and ϕ (right) sensors of the silicon modules composing the VELO. For completeness, in the right part there are drawn the strips of two adjacent ϕ modules, to show their different orientation.

The R sensors are divided into four parts per halve, each one covering about 45°; the microstrips composing these parts are modeled in a semi-circular shape and their width increases as the distance from the center becomes greater, because the majority of the particles is expected to be near the beam axis (*i.e.* in high η regions). The microstrips width ranges from 40 μm near the center to 92 μm far from the beam.

The ϕ sensors are divided in an inner and in an outer region. The latter starts at a radius of 17.25 mm and its pitch is set to be roughly half (39.3 μm) that of the inner region (78.3 μm), which ends at the same radius. Inner and outer regions have different skew to the radial direction to improve pattern recognition: they are tilted by 20° and 10° respectively. Furthermore, to improve the track reconstruction, the longitudinally adjacent ϕ sensors have opposite skew to each other.

The performances of the VELO detector have been analyzed using the the data collected in 2010 and 2011. The resolution on the X and Y coordinates ranges from 40 μm to 10 μm depending on the number of tracks fitted while the resolution on the Z coordinate ranges from 250 μm to 50 μm, for the same reason: this trend is clearly seen in Fig. 2.8.

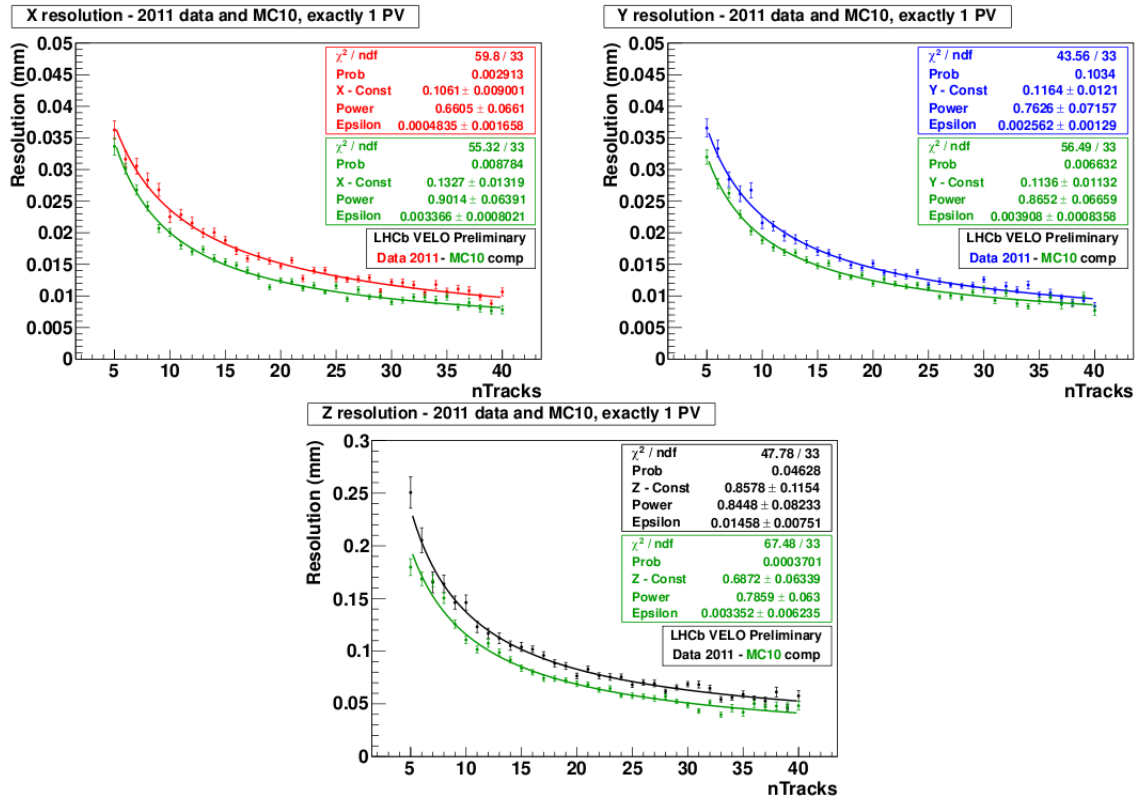

Figure 2.8: Plots showing the resolutions obtainable for the reconstruction of the primary vertex coordinates as a function of the number of fitted tracks. The plots report the X coordinate resolution (top left), the Y coordinate resolution (top right) and the Z coordinate resolution (bottom). The resolution displayed are referred to events where only one primary vertex has been reconstructed.

2.4.2 The Trigger Tracker

The Trigger Tracker (TT) [46] is placed after the first Ring Imaging Cherenkov detector RICH1 and before the magnet. The TT task is to provide reference segments used to combine the track reconstructed in the tracking stations with those reconstructed in the VELO, in order to improve the momentum and coordinate resolution. Since in the space between the VELO and the TT station an integrated magnetic field of 0.15 Tm is present, the track transverse momentum can be estimated with a resolution of $\delta p_T/p_T = 25\%$ at $p_T = 1$ GeV/c [47].

The system is composed by four stations, divided in two groups called respectively TTa and TTb, at a distance of about 30 cm one from the other and placed approximately 2.4 m after the beam interaction region. A detailed scheme of this part of the LHCb detector is shown in Fig. 2.9. Each of the four stations covers a rectangular region of about 120 cm in height and about 150 cm in width. A TT detector layer is composed of silicon microstrip sensors with a 183 μm pitch, arranged in readout strips up to 38 cm long, to keep the number of readout channels low. In the first and fourth stations the strips are parallel to the vertical plane, while in the second and third stations they are tilted respectively by $+5°$ (u-layer) and -5° (v-layer). This is done to improve the precision of the track reconstruction.

2.4.3 The tracking stations T1-T2-T3

The three tracking stations T1, T2 and T3 are placed behind the magnet. They are divided in two main parts, depending on the distance from the beam pipe. The inner part of the tracking stations is called Inner Tracker (IT), while the outer part is called Outer Tracker (OT). They adopt different technologies to detect the particles: the former is composed of silicon microstrip sensors, while the latter consists of drift straw tubes.

The Inner Tracker [48] covers the region around the beam pipe and it is arranged in a cross-shaped geometry, that grants optimal coverage while conserving surface; each station consist of four independent boxes arranged as shown in Fig. 2.10. As for the TT, the first and fourth planes of the IT have the sensors parallel to the vertical plane, while the second and the third planes have the sensors tilted by $+5°$ (u-layer) and -5° (v-layer). The side boxes have to two ladders of microstrips, with those of the lower sensor connected in series with those of the upper sensor to a single readout channel, while the top and bottom boxes have only one microstrips ladder. The total IT size is about 1.2 m in the bending plane and about 40 cm in the vertical plane.

The Outer Tracker [49] is a gas-filled straw tube detector, covering about 99% of the summed surface of the T1-T3 tracker stations. For each tracking station there are four planes of straw tubes arranged in the same way as the TT and IT silicon microstrip sensors: the first and the fourth have the tubes parallel to the vertical plane, while the second and the third have the tubes tilted by $+5°$ (u-layer) and -5° (v-layer). Moreover,

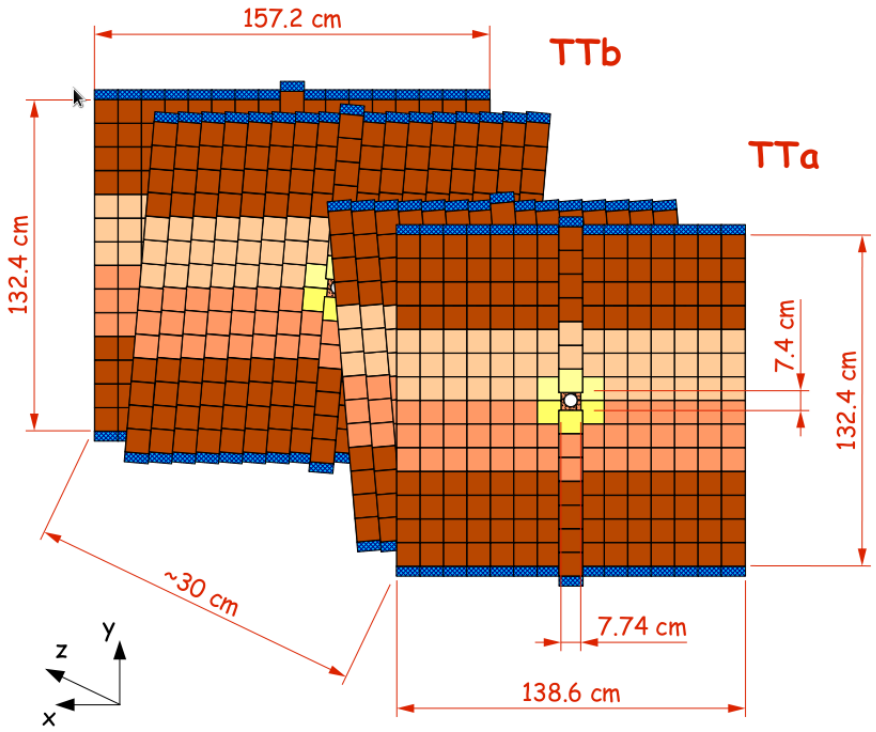

Figure 2.9: Trigger Tracker illustration. The first and fourth stations have sensors parallel to the vertical plane, while the second and third stations (called u-plane and v-plane) have sensors tilted respectively by $+5°$ and -5°.

each plane is composed of two rows of tubes, arranged in a honeycomb structure, as shown in Fig. 2.11. The straw tubes have a radius of 5 mm and are filled with a mixture of $Ar/CF_4/CO_2$. At the tube ends, locator pieces support and center the anode wire with a precision better than 100 μm. Unlike other tracking detectors here described, the OT measures drift times rather than pulse heights. The readout time window exceeds a single LHC bunch crossing interval due to the limited drift speed of the gas mixture. The OT resolution is better than 200 μm.

2.4.4 The LHCb dipole magnet

All modern experiments measure particle momenta through the curvature in a given magnetic field. For this reason, the LHCb detector is provided with a warm (*i.e.* non superconducting dipole) magnet dipole [50] placed between the TT and the first tracking station T1, as can be seen in Fig. 2.5. The magnet geometry has been chosen considering the detector acceptance: in fact, the magnet is formed by two coils shaped in a particular

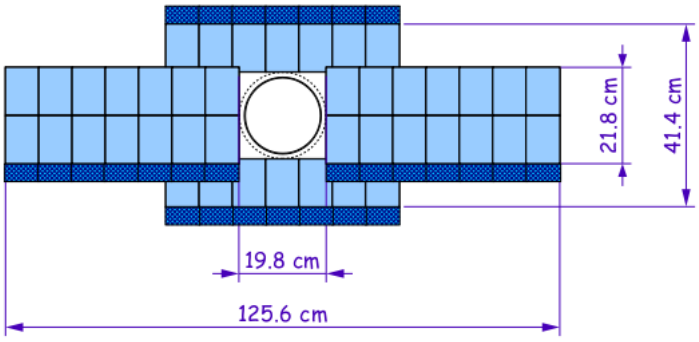

Figure 2.10: Inner Tracker layer with vertically oriented microstrip sensors. The four boxes are arranged around the beam pipe and the individual sensors inside the boxes are visible. The deep blue part of each box represents the readout plugs. For completeness, the dimensions of the IT are also reported.

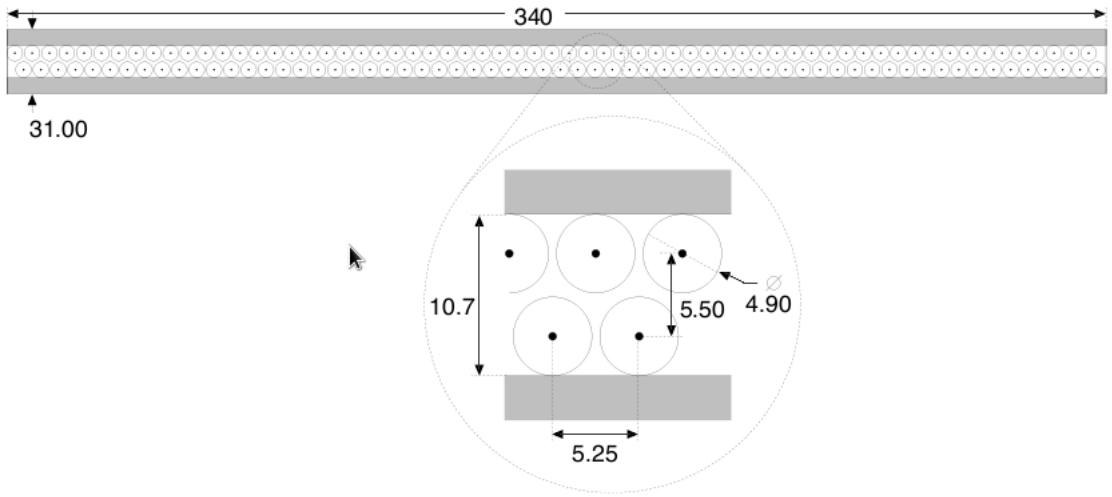

Figure 2.11: Cross section of a straw tube plane. The zoomed part shows the honeycomb structure of the two rows of tubes. For completeness, the dimensions (in mm) of the straw tube plane are also reported.

way, in order to become wider as the Z coordinate increases. The magnetic field is oriented along the Y coordinate, perpendicular to the X-Z plane, referred to as the bending plane. In Fig. 2.12 the Y component of the magnetic field is reported as a function of the Z coordinate and it can be seen that the maximum intensity of the magnetic field is about 1 T, while the magnetic field integral is 4 Tm.

During the data taking, the polarity of the magnetic field has been flipped several

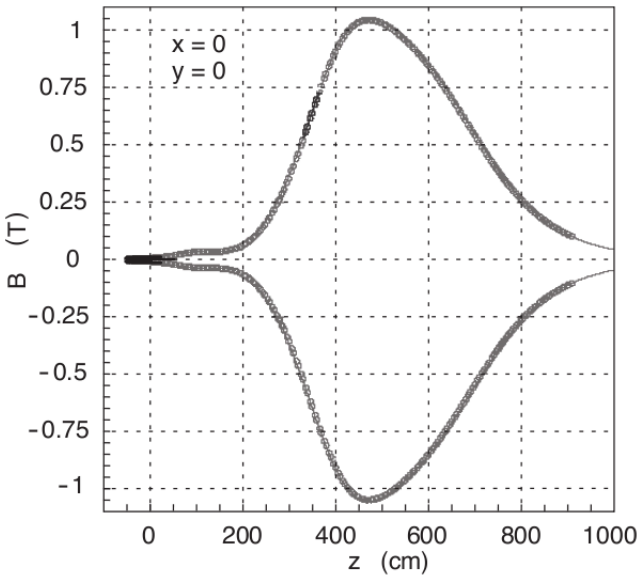

Figure 2.12: Magnetic field generated by the warm magnetic dipole as a function of the Z coordinate. From the plot it is evident that the maximum reached intensity is about 1 T.

times, in order to allow the evaluation of any left-right asymmetry in the detector. Indeed, since positive and negative charged particles are bent to opposite directions by the magnetic field, any variation in the detection efficiency between the left and the right part of the detector could affect $\mathcal{CP}$ asymmetry measurements.

2.4.5 Tracking algorithm and performances

We will now describe briefly how the tracking algorithm reconstructs the various track types, divided in five categories, as reported in Fig. 2.13:

Long tracks: Particles generating hits in all tracking sub-detectors.

VELO tracks: Particles generating hits only inside the VELO because they have been produced with a wide angle with respect to the beam pipe; for this reasons they exit from the detector geometrical acceptance just after the VELO.

Upstream tracks: These tracks are generated by particles with a low momentum, that produce hits in the VELO and in the TT, but are kicked off the geometrical acceptance of the detector by the magnetic field generated by the warm magnetic dipole. We can however measure the momentum of these particles thanks to the residual magnetic field present in the VELO, even if the measurement is affected by a 20% relative uncertainty.

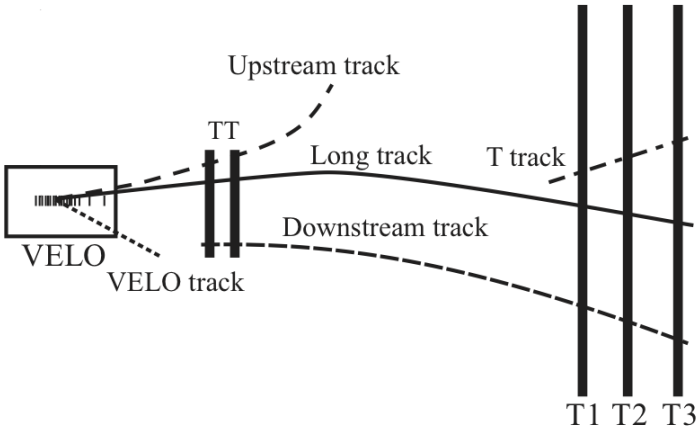

Figure 2.13: Illustration of the various track types: long, VELO, upstream, downstream and T tracks.

Downstream tracks: Long lived neutral particles can decay between the VELO and the TT, producing charged particles that generate hits in the TT and in the three tracking stations. These are the so-called downstream tracks.

T tracks: Hits only in the tracking stations are classified as T tracks.

Track finding and reconstruction are organized in different steps. The first starts with the definition of segments in the various sub-detectors: inside the VELO, segments are created matching all hits that lie on a straight line. In the tracking stations, a segment is created matching the hits contained in a section of the first and third station (*e.g.* in the left corner on these two stations), using the information given only by one plane of vertically oriented microstrip sensors. Then, under the hypothesis of a parabolic trajectory, the algorithm calculates the position of the hit in the middle stations and searches for compatible hits. If a signal is found, it is added to the segment and it is used to better determine the parameters of the trajectory. Finally, the compatible hits coming from the u-plane and the v-plane are also added, in order to have a 3-dimensional segment.

The reconstruction process is organized in a hierarchical way: the algorithm tries firstly to reconstruct long tracks and then it picks up unused segments to reconstruct downstream and upstream tracks. Long tracks are reconstructed with two algorithms: the first extrapolates VELO segments to the tracking stations, adding to the track the compatible hits in the TT. The second matches VELO and tracking stations segments one to each other, extrapolating VELO segments in the forward direction and tracking stations segments in the backward direction. Downstream tracks are reconstructed starting from T stations segments and then adding the compatible hits in the TT to those segments. Upstream tracks are obtained extrapolating VELO segments to the

Trigger Tracker, adding compatible hits and requiring a non compatibility with any of the tracking station segments.

Finally, a bi-directional Kalman filter is applied to better determine the track parameters and then a clone killer compares the reconstructed tracks, two by two: if a pair of tracks shares more than a fixed percentage of hits they are considered clones and only that with more hits (or the best χ^2) is stored.

2.5 The LHCb particle identification systems

In this section all the sub-detectors installed in the LHCb detector, used for the particles identification are described. These systems include two Ring Imaging Cherenkov detectors (RICH1 and RICH2), the electromagnetic calorimeter (ECAL), the hadronic calorimeter (HCAL) and finally the muon detector.

2.5.1 The RICH detectors

Particle identification is of fundamental importance in $\mathcal{CP}$ violation measurements. LHCb uses two Ring Imaging Cherenkov detectors (RICH1, installed immediately after the VELO, and RICH2, positioned after the tracking stations) [51] to discriminate charged pions, kaons and protons in a momentum range between few GeV/c up to about 150 GeV/c. Cherenkov light detectors exploit the light emitted by particles that travel in a medium faster than the light in the same medium. The relation between the Cherenkov photon emission angle θ_C and the refraction index n of the radiator is:

$$\cos(\theta_C) = \frac{1}{\beta n} \ , \tag{2.1}$$

where $\beta = v/c$ is the particle velocity with respect to the speed of light in vacuum. From this relation, we can notice that Cherenkov light is emitted only by those particles with $c/n < v < c$; in fact, if $v = c/n$ then $cos(\theta_C) = 1$ and so $\theta_C = 0$, while if $v = c$ then $\cos(\theta_C) = 1/n$ and so $\theta_C = \arccos(1/n)$. Thus, it is evident that for particles approaching the speed of light the Cherenkov angle will saturate at the value $\theta_C = \arccos(1/n)$. For these reasons, it is necessary to have different radiators in order to discriminate particles in a wide range of momenta.

RICH1 is optimized to identify tracks with a medium-low momentum, between 1 GeV/c and about 50 GeV/c. The structure of the apparatus is reported in the left part of Fig. 2.14. The RICH1 is placed immediately after the VELO and its geometrical acceptance (between 25 mrad to 330 mrad) is enough to cover practically the whole LHCb detector acceptance. There are two different types of radiators inside RICH1: the first is a 5 cm thick Aerogel layer, with $n = 1.03$, suitable for low momentum particles,

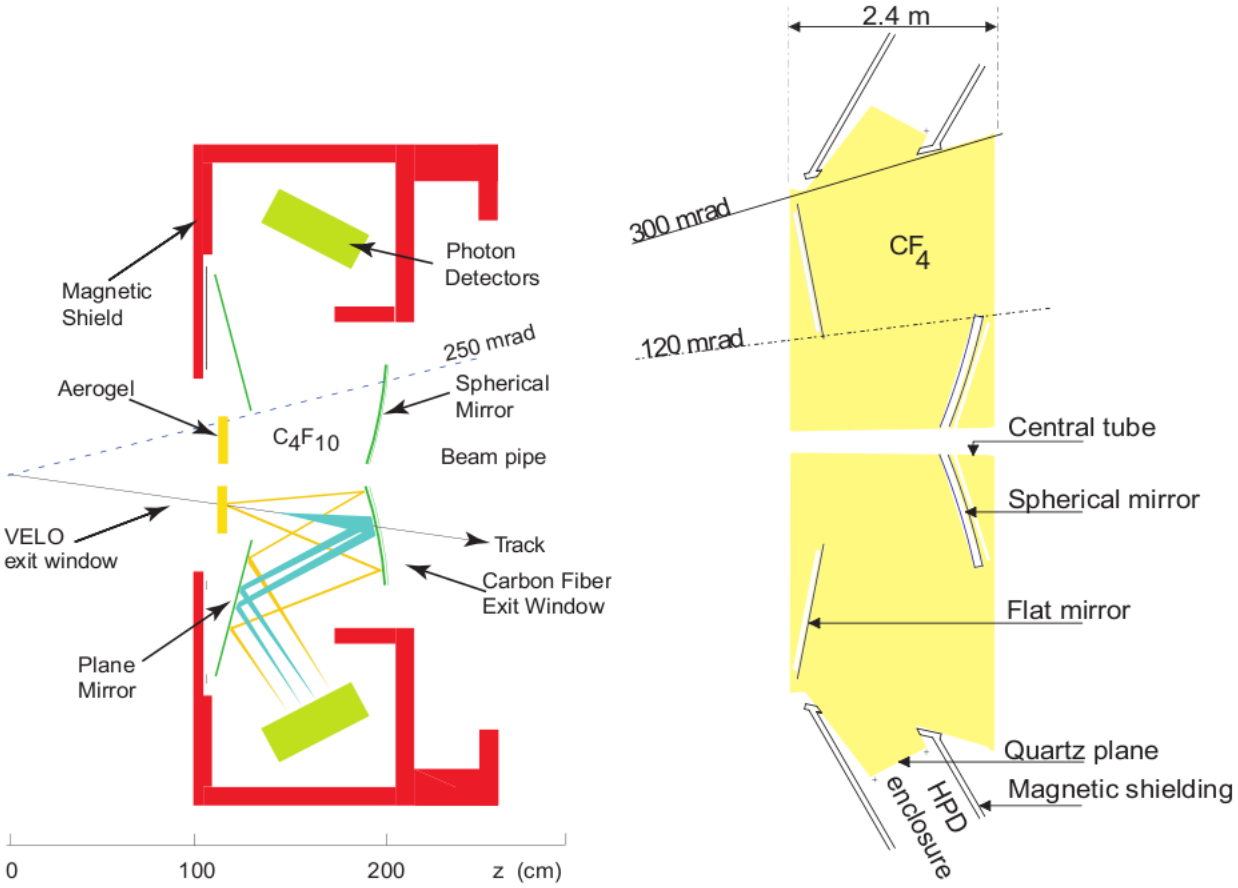

Figure 2.14: Left: schematic view of the RICH1 sub-detector. It is relevant to note the different Cherenkov photon emission angles of the Aerogel (yellow) and C_4F_{10} (light blue) radiators. Right: schematic view of the RICH2 sub-detector, filled with CF_4 gas.

while the second, gaseous C_4F_{10} ($n = 1.0015$), fills the remaining part of the detector and is employed to detect particles with higher momenta (up to 50 GeV/c).

RICH2 is placed behind the last tracking station and its geometrical acceptance, 120 mrad in the vertical plane and 100 mrad in the horizontal plane, covers the region of the detector where most of high momentum particles are found. The radiator chosen for this sub-detector is gaseous CF_4, with a refraction index $n = 1.00046$, optimal for the higher momentum region, up to about 150 GeV/c.

The Cherenkov photons emitted in both detectors are conveyed, through a system composed of spherical and plane mirrors, onto a lattice of photo detectors, the Hybrid Photon Detector (HPD). The HPD's are placed in both the RICH sub-detectors outside the LHCb detector acceptance and they are shielded against the residual magnetic field (this is particular important for RICH1, because in this region of the detector the residual

magnetic field is not negligible). The shielding is necessary in order to allow the HPD's to operate properly: indeed, the photo-electrons created in the photomultipliers would be bent by the residual magnetic field and this could reduce the HPD's performances. This configuration allows to have optimal results with signal's rise and fall times ~ 1 ns.

2.5.2 Particle identification method

RICH detectors are able to discriminate between the various mass hypotheses for a given particle. Indeed, as shown in Fig. 2.15, the photon emission angle is related to the particle mass and to its momentum. Moreover, since the emission covers the full solid angle, we expect to see rings on the HPD plane, with radius proportional to θ_C. The hits on the HPD plane will be distributed around a particular radius value (that corresponds to the Cherenkov emission angle); anyway, due to resolution effects, the distribution will be smeared around the central value. Measuring the photons hit positions, it is then possibile to obtain a value of θ_C for each particle, allowing us to discriminate between the various mass hypotheses.

Due to an irreducible background, given by photons coming from other particles, and due to the complexity of the problem, the following approach has been chosen to achieve the best particle discrimination. For a given set of mass hypotheses, the probability for a single photon to be detected on a single HPD pixel is computed; then, the expected contribution from all sources is compared with the observed number of photons and a likelihood is calculated (the change in the likelihood value depends only on the mass hypotheses assigned to the tracks). Only five mass hypotheses are considered for the tracks detected: electron, muon, pion, kaon, proton. Since the computation of the likelihood for all tracks would be unfeasible, a different approach is adopted. In fact, the pion mass-hypothesis is used for all the tracks detected and a first global likelihood is computed. Then the hypothesis is changed to e, μ, K and p for one particle at a time and the change in the global likelihood is computed. The chosen mass hypotheses is the one that returns the maximum improvement in the global likelihood. This process is repeated for all tracks, until no improvement is observed in the likelihood value.

The discriminating variable is the so called $\Delta \log \mathcal{L}$. For example, $\Delta \log \mathcal{L}_{K-\pi}(P)$ is the difference between the logarithm of the likelihood under the K and π hypothesis for the particle P

$$\Delta \log \mathcal{L}_{K-\pi}(P) = \log \mathcal{L}_K(P) - \log \mathcal{L}_\pi(P) \ . \tag{2.2}$$

A large positive value of $\Delta \log \mathcal{L}_{K-\pi}(P)$ corresponds to a high probability that the particle P is a kaon, while a large negative value of $\Delta \log \mathcal{L}_{K-\pi}(P)$ corresponds to a high probability that the particle P is a pion.

The efficiency of this discriminating method has been widely studied using real data samples with high purity final states selectable only using kinematical cuts, due to their particular kinematic characteristics (*e.g.* $K^0_S \to \pi^+\pi^-$, $\Lambda \to p\pi^-$, $D^{*+} \to$

$D^0(K^-\pi^+)\pi^+$), without using the RICH sub-detectors. The results are reported in Fig. 2.16, where the efficiency (for correctly identified particles) and misidentification (for wrongly identified particles) are plotted as a function of the momentum (as θ_C depends on the particle momentum).

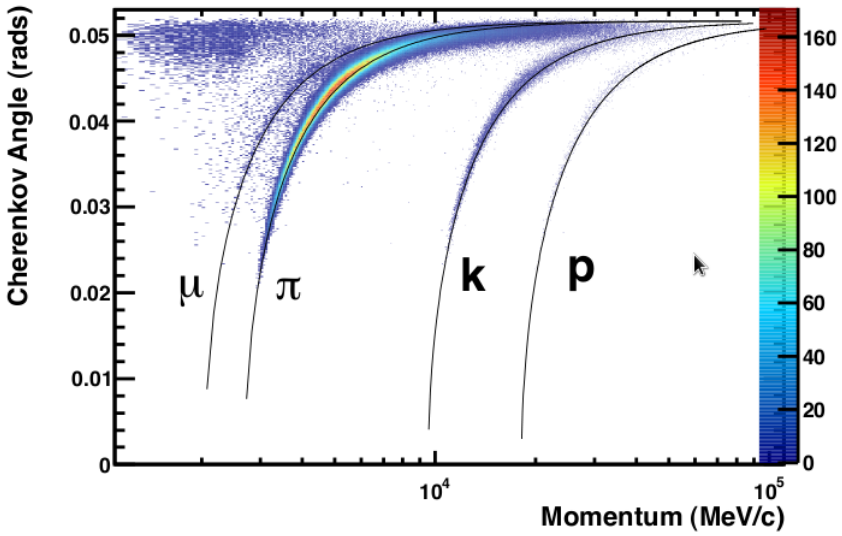

Figure 2.15: Cherenkov photons emission angle as a function of the particle momentum. The theoretical value (solid line) is superimposed to the experimental results.

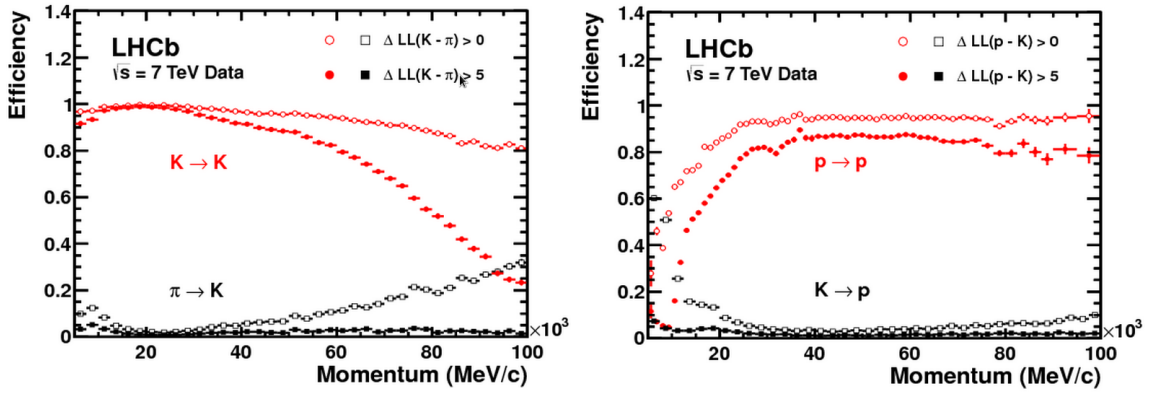

Figure 2.16: Left: Efficiency for the identification of kaons (red) and misidentification probability of pions as kaons (black) as a function of the particle momentum. Solid and empty points correspond to different requirements on the $\Delta \log \mathcal{L}$. Right: Efficiency for the identification of protons (red) and misidentification probability of kaons as protons (black) as a function of the particle momentum. Solid and empty points correspond to different requirements on the $\Delta \log \mathcal{L}$.

2.5.3 The calorimeters system

The calorimeter system [52] is used to measure hadron, electron and photon energies, thus giving information for their identification. Moreover, it provides important information for the Level-0 trigger (L0-trigger), evaluating hadron, electron and photon transverse energy[2] E_T. The calorimeter system is divided into four sub-detectors:

- Scintillator Pad Detector (SPD);
- Pre-Shower (PS);
- Electromagnetic Calorimeter (ECAL);
- Hadronic Calorimeter (HCAL).

In Fig. 2.17 we have schematically represented the calorimeter system and the interactions of each sub-detector with each type of particle. Each sub-detector is divided

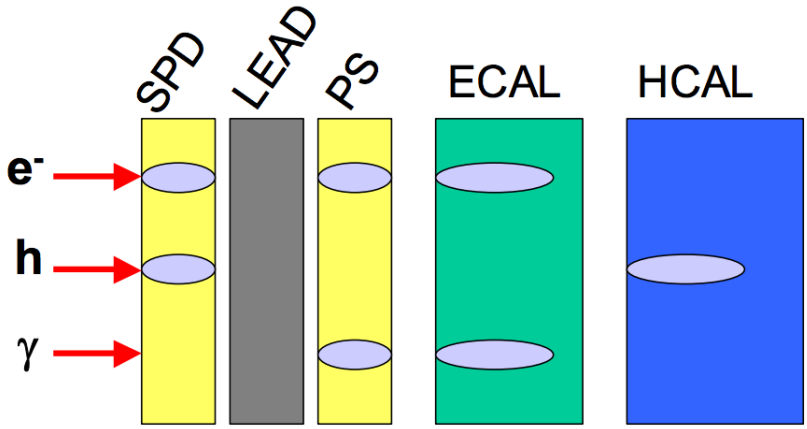

Figure 2.17: Signal deposited on the different parts of the calorimeter by an electron, a hadron and a photon.

into regions with different dimensions and where differently sized sensors are used (the smallest sensors, *i.e.* the most precise, are placed in the inner regions, while the biggest are placed in the outer regions). SPD, PS and ECAL are divided in three regions (inner, middle and outer), while the HCAL is divided only in two regions (inner and outer); a schematic view of these structures is displayed in Fig. 2.18. The sensor size increases as the distance from the beam pipe is greater in order to reach a compromise between occupancy and the number of read-out channels.

[2]The transverse energy is defined as $E_T = E\sin(\theta)$, where E is the energy measured in the calorimeter and θ is the polar angle of the hits in the calorimeter with respect to the beam pipe.

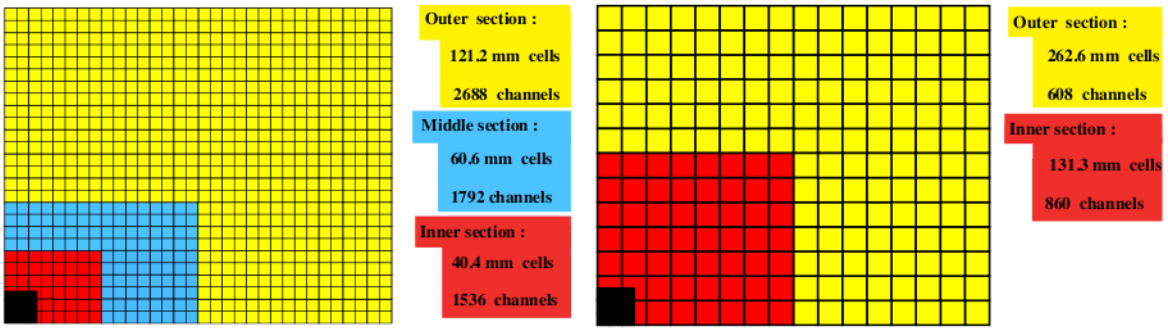

Figure 2.18: Left: frontal schematic view of the SPD/PS and ECAL, where the three regions described in the text are visible. Right: frontal schematic view of the HCAL, where the two regions described in the text are visible. Note that only a quarter of the detectors is shown. For completeness, the sensor dimensions and the number of channels are also reported for both the images.

The SPD and the PS are auxiliary sub-detectors of the Electromagnetic calorimeter and they are placed in front of it. The SPD is used to discriminate between charged and neutral particles, as the former emits light when crossing a scintillator material while the latter does not. The PS is instead used to obtain a better discrimination between electrons and pions. Both the SPD and the PS consist of scintillating pads with a thickness of 15 mm, interspaced with a 2.5 radiation lengths[3] lead converter. The light produced by the scintillator material is collected using wavelength-shifting fibers (WLS). These fibers are used to transmit the light to multi-anode photomultipliers (MAPMTs) located outside the detector. The SPD and the PS contain about 6000 pads each.

The ECAL is a sampling calorimeter realized using Shashlik technology and separated in independent modules. The Shashlik calorimeters are sampling calorimeters in which the scintillation light is read-out via WLS fibers running perpendicularly to the converter/absorber plates [54, 55]: this technique offers the combination of an easy assembly, good hermiticity and fast time response. A sketch of ECAL is given in Fig. 2.19.

Each ECAL module is composed of 66 lead converter layers (2 mm thick), each one installed between two plastic scintillator layers 4 mm thick. In total, all the layers

[3]The radiation length is defined as

$$X_0 = \frac{A \cdot 716.4\ g/cm^2}{Z(Z+1)\ln(287\sqrt{Z})}$$

where A is the mass number and Z is the atomic number of the material considered. The radiation length corresponds to the distance over which the energy of an electron is reduced by a factor $1/e$ only due radiation loss. For a discussion see Ref. [53].

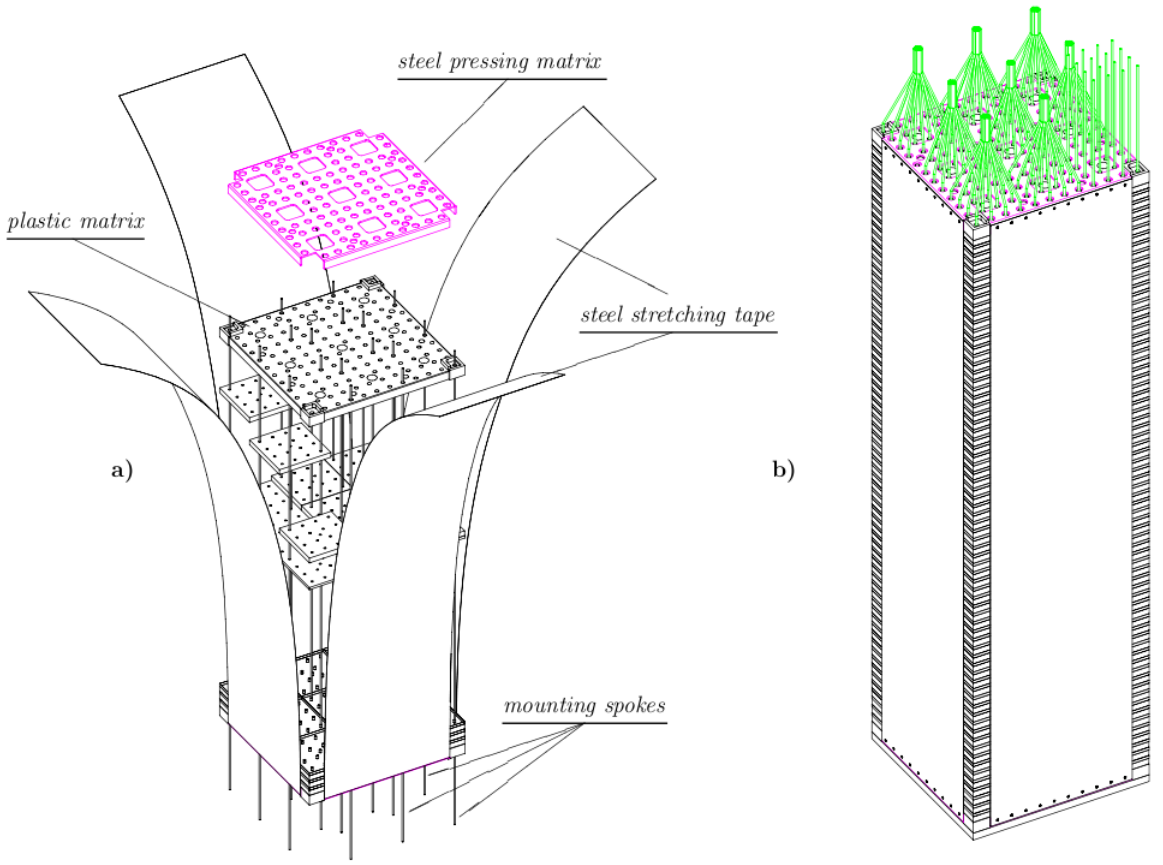

Figure 2.19: Left: Representation of an ECAL module during the assembly phase. The lead/scintillator layers are clearly visible. Right: Representation of an assembled ECAL module. The green lines connected to an end are the WLS fibers connecting the calorimeter to the photomultipliers.

installed in the ECAL correspond to about 25 radiation lengths and 1.1 nuclear interaction lengths. The WLS fibers bring the light produced by the scintillator material to the read-out photo-multipliers in the back part of the module. As shown in Fig. 2.18, the module size and the number of read-out channels differ depending on the region where the module is installed. In the inner region each module has a section of 4×4 cm^2, with 9 read-out channels per module; the middle region contains modules with a section of 6×6 cm^2 and 4 read-out channels. Finally, the outer region is composed of 12×12 cm^2 modules with one channel each.

The HCAL main task it to measure the energies of hadronic showers. This information if fundamental for the Level-0 trigger. The HCAL structure is very similar to the ECAL structure, with the difference that each module is composed of scintillator layers 4 mm thick interleaved with steel layers 16 mm thick. This corresponds to roughly 5.6

nuclear interaction lengths in total. In the inner region, modules have a section of 13 × 13 cm^2, while in the outer region they are 26 × 26 cm^2.

2.5.4 Calorimeter system resolution

The calorimeter system performances have been evaluated from many test beams made before the start of the data taking [56]. Energy resolutions are given by $\sigma(E)/E = (8.5-9.5)\%/\sqrt{E} \oplus 0.8\%$ for ECAL and $\sigma(E)/E = (69 \pm 5)\%/\sqrt{E} \oplus (9 \pm 2)\%$ for HCAL. The ECAL calibration is achieved by reconstructing resonances decaying to two photons like $\pi^0 \to \gamma\gamma$ and $\eta \to \gamma\gamma$. Calibration of the HCAL can be realized by measuring the ratio E/p between the energy E as measured in the calorimeter for a hadron with momentum p, as measured by the tracking system.

2.5.5 Muon detectors

The final part of the LHCb detector consists of five muon stations, that altogether form the muon sub-detector [57]. Muons with high p_T are very important particles since they are used by the tagging algorithm to identify the flavor of the spectator B-hadron produced associated to the signal B-hadron. Moreover, several final products of B-hadron decay chains contain muons, *e.g.* $B_s^0 \to J/\Psi(\mu^+\mu^-)\phi$, $B^0 \to K^{*0}\mu^+\mu^-$, $B_s \to \mu^+\mu^-$.

Five stations (M1,..., M5) cover an angular acceptance of ±300 mrad in the horizontal plane and ±200 mrad in the vertical plane. The geometrical efficiency for the detection of muons coming from B-hadrons is nearly 46%. The first muon station M1 is placed before the calorimeters, to avoid possible muon multiple scattering effects, that could modify the particle trajectory. The remaining four muon station (M2-M5) are placed after the calorimeter system, at the end of the LHCb detector. A schematic view of the entire muon sub-detector is reported in Fig. 2.20.

Each muon station is divided into four regions (R1-R4, where R1 is the closest to the beam pipe and R4 is the farther). The dimensions of the chambers increase as they are more and more distant from the beam pipe; moreover, also the segmentation of each region increases as the distance from the beam pipe becomes greater, in a ratio 1:2:4:8, as shown in Fig 2.21. In this way, the charged particle occupancy is expected to be about the same in each region. All the chambers are Multi-Wire Proportional Chambers, except for the inner region of the M1 station, where triple-GEM detectors are employed. MWPCs have four overlapped gaps, each one 5 mm thick and with a distance between wires of about 2 mm. In total, the muon detector contains 1380 MWPCs. The triple-GEM detector consists of three gas electron multiplier foils sandwiched between anode and cathode planes.

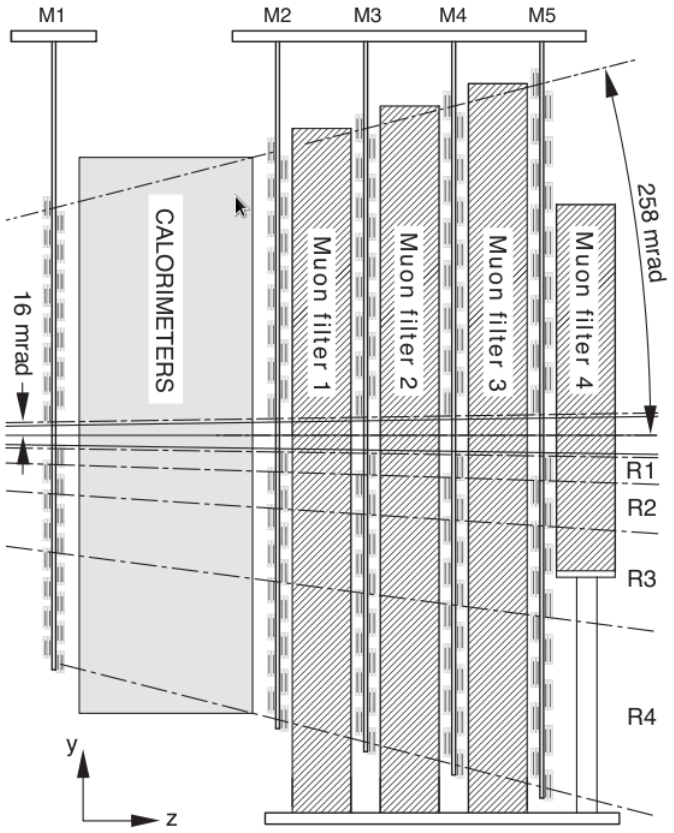

Figure 2.20: Lateral view of the muon detector. As stated in the text, the first muon station M1 is placed before the calorimeters, while the remaining stations are placed at the end of the LHCb detector.

2.5.6 Muon-ID algorithm performances

The algorithm for muon-ID in the hardware trigger starts from hits in the M3 station. For each hit, a straight line is extrapolated to the interaction region defining a "field of interest", that takes into account also the magnetic field kick, around such a trajectory. Hits coming from long and downstream tracks that are found around the extrapolated trajectory are fitted together to form a muon track. To consider the track as a muon it is requested to have hits in M1-M3 if the track momentum is between 3 and 3.5 GeV/c and to have hits in M1-M4 if the track momentum is between 3.5 and 4.5 GeV/c. Finally, it is required to have hits in all the five stations if the track momentum is higher than 4.5 GeV/c.

After this, complex algorithms compute the muon likelihood for each muon track, used as a particle identification discriminator.

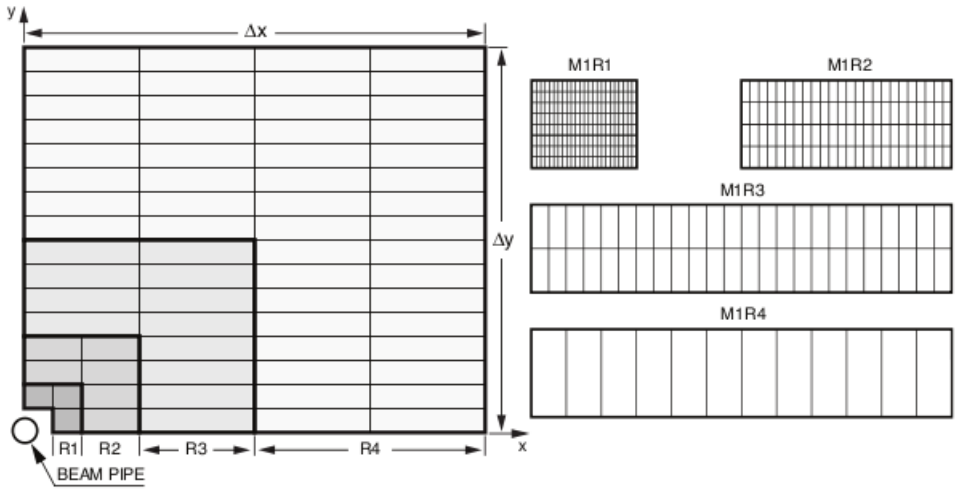

Figure 2.21: Left: Frontal view of a muon station section. Each rectangle represents a chamber and it is evident that they become larger as the distance from the beam pipe becomes greater. Right: different segmentation types of the four chambers. The inner chambers are more segmented than the outer ones.

2.6 The LHCb trigger

As already stated, the production cross section of $b\bar{b}$ and $c\bar{c}$ pairs are quite large, but they are smaller than the pp inelastic cross section. This means that we need a good trigger system in order to accept only the interesting events while rejecting at the same time most of the background events. The LHCb trigger has been developed to work at the bunch crossing frequency of the LHC, in order to process the largest number of events. The only way to reach the desired performances is to divide the trigger into different levels, each processing the output of the previous.

The LHCb trigger system is divided into three levels:

Level-0 (L0): this is the first trigger level and it is based on custom electronics. It is designed to perform a first filtering of the events, reducing the input rate of about 10 MHz to an output rate of only 1 MHz.

High Level Trigger 1 (HLT1): this is the second trigger level and, in contrast to the first, it is software based. The task of HLT1 is to filter events in an inclusive way and to reduce the rate of accepted events to 50 kHz, starting from an input rate given by the L0 of about 1 MHz.

High Level Trigger 2 (HLT2): this is the last trigger level and, as the previous one, it is completely software based. The HLT2 takes an input rate of 50 kHz from

the HLT1 and reduces it to an output rate of about 3 kHz, applying an exclusive selection of beauty and charm decays. The output of HLT2 is finally sent to mass storage.

After this brief introduction, we will now describe in detail the various trigger levels.

2.6.1 Level-0 Trigger

The L0 trigger uses information coming mainly from the tracking system and from the calorimeter system. In fact, at this level, the trigger decides to keep or discard events based on measures of p_T and E_T of the particles composing the event. The system uses three independent systems running in parallel:

Electron/photon trigger: this trigger uses the information given by the SPD/PS and ECAL detectors. Custom boards are programmed to measure the energy of electromagnetic showers. The event is accepted if there is at least one cluster with E_T exceeding a given threshold.

Hadronic trigger: as the name suggests, this trigger utilises the information given by the HCAL detector. The way in which it works is the same as the electron/photon trigger: the event is accepted if there is at least one cluster with enough transverse energy.

Muon trigger: it uses the information given by the five muon stations. Tracks are reconstructed defining fields of interest around particles hits and then connecting hits in the same field of interest. Events are accepted if at least one muon candidate has a transverse momentum greater than a threshold; moreover, the trigger contains a line to select muon pairs, asking that the sum of their transverse momentum exceeds a threshold.

Furthermore, since in 2010 and 2011 the detector worked at an input rate four times larger than what planned, a system to reject high-occupancy events was developed and implemented in the L0 trigger. Thanks to its fast response, the SPD can be used to roughly estimate the number of charged particles per event. It has been decided to accept events only if the number of hits in the SPD was less than 600.

2.6.2 The High Level Trigger 1

The task of this trigger level is to reduce the input rate from the L0 trigger to a more manageable level. This is done rejecting events with an OT occupancy larger than 20%, because they would take more than the $\sim$ 25 ms allowed to the HLT1 to take a decision. After this first rough selection, the remaining events are reconstructed, considering that:

- High mass B hadrons and their production mechanism imply that the particles produced in their decays have a large momentum p and transverse momentum p_T compared to other hadrons composed by light quarks.

- The average decay length of B hadrons produced at the LHC is about 1 cm. As a consequence, their decay products will have a large impact parameter (IP) with respect to their primary vertex (PV).

- Each B hadron decay has at least one final state particle with large p, p_T and IP.

- VELO reconstruction time is fast enough to allow the full information on the primary vertex to be used by the HLT1.

- The full reconstruction can be performed only for a limited number of tracks due to limited time available.

The last two points are the reason why the reconstruction is divided in two steps. In the first step VELO tracks and PV are reconstructed. The tracks are selected requiring large impact parameters with respect to the closest PV and a minimum number of hits in the VELO. If the difference between the expected number of hits and the observed number of hits in the VELO is greater than a certain threshold, the track is rejected. For example, a typical choice of the cut values used is: $IP > 125$ μm, $N_{hits}^{obs} > 9$ and $N_{hits}^{exp} - N_{hits}^{obs} < 3$. After this, forward reconstructed tracks are further selected, requiring minimal p and p_T thresholds. Finally, remaining tracks are fitted using a bi-directional Kalman filter with outlier removal, in order to obtain an offline-quality value for the track χ^2 as well as an offline-quality covariance matrix at the first state of the track, allowing a cut on the IP significance squared ($\chi^2(IP)$). Cut on $\chi^2(IP)$ is very efficient in rejecting background, while the track χ^2 is suitable in rejecting ghost tracks.

2.6.3 The High Level Trigger 2

HLT2 filtering is mainly based on three inclusive selections, the so-called topological lines. In addition, a few dedicated lines for the LHCb core analyses are used.

The main strategy of topological lines is to build multibody candidates in the following way:

- two particles are combined to form a two-body object;

- another input particle is added to the two-body object to form a three-body object and so on;

- the pion mass hypothesis is adopted for all tracks.

In this way, n-body objects are built combining the $(n-1)$-body candidate with another particle (saving CPU time with respect to combining n particles directly). Particles are added to an object only if they respect a cut on the distance of closest approach ($DOCA$). For example, the two particles forming a two-body object need to have $DOCA < 0.15$ mm. When a 3-body object is built combining a 2-body object with another particle, another $DOCA < 0.15$ mm cut is imposed and so on for the construction of further objects.

In addition, HLT2 contains lines which exploit tracks identified as muons. Dimuon candidates are formed and, depending on their mass, cuts are applied on the flight distance and p_T of the dimuon candidate. Single muon candidates are accepted requiring a large p_T or a combination of $\chi^2(IP)$ and p_T cuts.

2.7 Data management and computing

The basic LHCb computing model is based on a series of distributed multi-tier regional centers of different dimensions. LHCb (as well as the other three major experiment at the LHC) requires large amounts disk space as well as of CPU power in order to store and process the data coming from the detector and to perform the first selections; it is important to note that it would be unfeasible to concentrate the resources needed to perform these tasks in one single place. For that reason the computing system is divided in different tiers dedicated to specific duties. The Tier0, located at CERN, provides to LHCb about 20% of the total resources required by the experiment and it is connected to the Tier1 centers via 10 Gbit/s optical-fibre links. Moreover, Tier0 stores all the RAW data, also providing a copy distributed among the Tier1 centers. There are 6 LHCb Tier1 centers worldwide that are responsible for storing a proportional share of raw and reconstructed data, as well as performing large-scale reprocessing and storing the corresponding output. Moreover, the Tier1 centers have to distribute the data to the Tier2 centers and to store a part of the simulated data coming from them. Each Tier1 is connected to a number of Tier2 centres, usually in the same geographical location. Finally, Tier3 resources consist of local clusters in a university department and are dedicated to specific jobs needed by the research team who owns them. This system is collectively referred to as the World LHC Computing Grid (WLCG). A schematic representation of its structure in Fig. 2.22.

2.7.1 Data processing

The data processing involves several phases that normally follow each other in a sequential manner.

The real RAW data come from the detector and they are reconstructed via the online Event Filter farm. Obviously, the first step is to collect the events of interest with an ap-

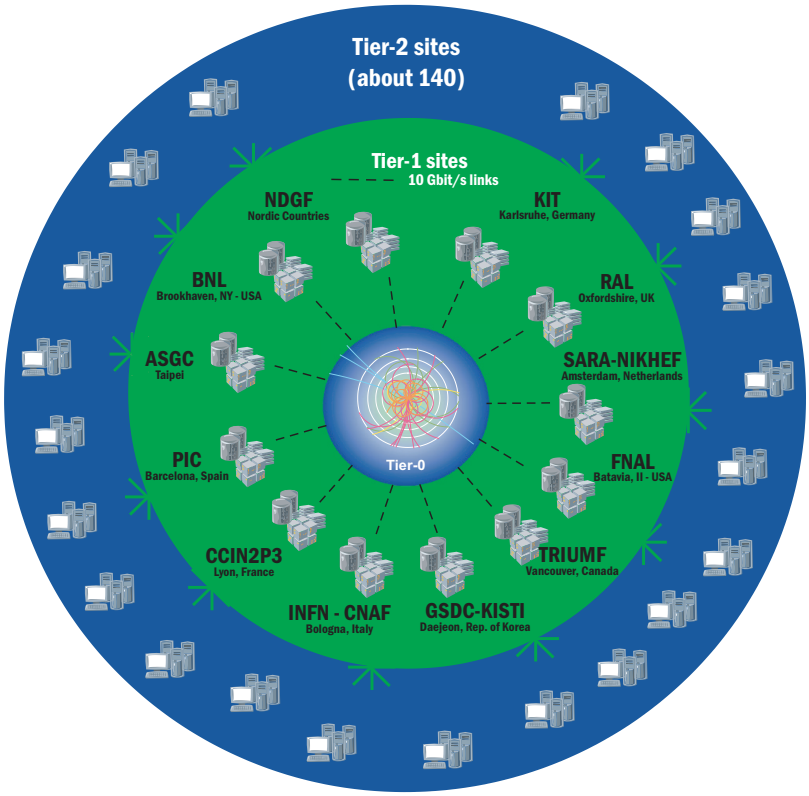

Figure 2.22: Schematic representation of the WLCG.

propriate trigger system. The RAW data are then processed using optimized and highly specialized algorithms implemented by the HLTs. The software applies the necessary calibration corrections during the reconstruction of the properties of the particles and imposes cuts based on physics criteria. The RAW events accepted by the trigger are then transferred to the CERN Tier0 center in order to be archived and they are forwarded to the Tier1 centres for further processing. It is important to note that the system does not keep a copy of the data excluded by the trigger selection: if an event is discarded then it is lost forever.

For what concerns the simulated data, the events are generated by a MonteCarlo model of LHCb detector, that includes the best understanding of the LHCb detector response, trigger response and dead material. This type of data contain extra "truth" information apart from the simulated hits and other quantities of interest. The truth information is needed to keep track of physics history of the event and it is carried through all the subsequent processing steps in order to be used during the analysis. Apart from this information, that implies that simulated datasets are larger than real raw data, the format of the simulated and real raw data is the same and thus they can be reprocessed by the same software.

Whether the data are real or simulated, they must be reconstructed in order to provide physical meaningful quantities: for example, one must determine the energy of electromagnetic and hadronic showers measuring calorimeter clusters, or hits in the tracking system have to be associated to tracks. Furthermore, the information about PID coming from the RICH sub-detectors must also be reconstructed to provide particle identification. The reconstruction process produces a new type of data, the so called Data Summary Tape (DST).

The informations contained in the DST (tracks, energies, clusters, PID) is further analysed with specific algorithms, in order to identify candidates that could form composite particles. These algorithms are designed to select only certain categories of events (*e.g.* B2HH algorithm selects only B candidates decaying to two hadrons) and are called stripping lines. Such stripping lines are written for each channel of interest and they produce the output used for further analysis. The output of the stripping stage is referred to as full DST. In addition to the full DST, an event tag is also created for faster reference to the selected events. The tag contains a little summary of the event characteristics together with the results of the pre-selection algorithms and a reference to the events contained in the DST dataset.

The LHCb Collaboration runs the stripping lines four times per year: the first using the original data reconstruction, the second over the re-processed RAW data and the last two as the selection cuts and the analysis algorithms evolve.

Chapter 3

Determination of $\mathcal{A}_{\mathcal{CP}}(\Lambda_b^0 \to pK^-) - \mathcal{A}_{\mathcal{CP}}(\Lambda_b^0 \to p\pi^-)$

In this chapter we describe the analysis procedure followed to measure the difference between the direct $\mathcal{CP}$ asymmetries of the $\Lambda_b^0 \to pK^-$ and $\Lambda_b^0 \to p\pi^-$ decays, $\Delta\mathcal{A}_{\mathcal{CP}} = \mathcal{A}_{\mathcal{CP}}(pK^-) - \mathcal{A}_{\mathcal{CP}}(p\pi^-)$. The data sample employed includes the full 2011 and 2012 $H_b \to h^+h^{'-}$ datasets, corresponding to a integrated luminosity $\int \mathcal{L}dt \simeq 3$ fb^{-1}.

In order to measure $\Delta\mathcal{A}_{\mathcal{CP}}$ we need to first to determine the following quantities:

$$\mathcal{A}^{RAW}(pK^-) = \frac{N(\Lambda_b^0 \to pK^-) - \bar{N}(\bar{\Lambda}_b^0 \to K^+\bar{p})}{N(\Lambda_b^0 \to pK^-) + \bar{N}(\bar{\Lambda}_b^0 \to K^+\bar{p})} \tag{3.1}$$

and

$$\mathcal{A}^{RAW}(p\pi^-) = \frac{N(\Lambda_b^0 \to p\pi^-) - \bar{N}(\bar{\Lambda}_b^0 \to \pi^+\bar{p})}{N(\Lambda_b^0 \to p\pi^-) + \bar{N}(\bar{\Lambda}_b^0 \to \pi^+\bar{p})} \ , \tag{3.2}$$

where N and $\bar{N}$ are the number of occurrences of the corresponding decay, as determined from the fits to the invariant mass spectra. Finally the raw asymmetries need to be corrected to take into account detection asymmetries of the final state particles and the Λ_b^0 production asymmetry.

The first section describes the data sample employed and the pre-selection used. In the second section the PID calibration procedure is discussed. In the third section we describe in detail the invariant mass model used in the fitting procedure. The fourth section is devoted to the description of the offline selection employed to further refine the data in order to obtain the best statistical sensitivity on the $\mathcal{CP}$ asymmetries. The fifth section shows the results obtained from the fitting procedure and the sixth section describes the corrections needed to obtain the final $\Delta\mathcal{A}_{\mathcal{CP}}$ measurement.

3.1 Data sample and pre-selection

The data sample used in this analysis is composed of the entire sample of pp collisions collected during the 2011 and 2012 by the LHCb detector. The total integrated luminosity of about 3 fb^{-1} is divided by year and magnet polarity as reported in Tab. 3.1. In 2011 the LHC operated at a center-of-mass energy of 7 TeV, while in 2012 the runs have been done at $\sqrt{s} = 8$ TeV. Since the asymmetry we are going to measure is a characteristic of the decay, we do not separate the 2011 and 2012 datasets. However, note that the corrections to the raw asymmetries depend on the center-of-mass energy, but it has been verified that applying two different corrections to 2011 and 2012 data is totally equivalent to using a mean correction for the full sample.

	2011	2012
Magnet Down	584.26 pb^{-1}	1068.07 pb^{-1}
Magnet Up	434.42 pb^{-1}	1038.83 pb^{-1}
Mag. Down + Mag. Up	1018.68 pb^{-1}	2106.90 pb^{-1}
Total	3125.58 pb^{-1}	

Table 3.1: Integrated luminosities divided by year and magnet polarity.

3.1.1 Trigger

In order to select only the relevant events, the LHCb detector employs three trigger levels, as already discussed in the detector chapter. Here we briefly describe the main algorithms used to select the data of interest for the analysis: `L0Hadron`, `Hlt1TrackAllL0`, and `Hlt2B2HH`.

The `L0Hadron` trigger algorithm must decide whether to accept or to reject an event in a very short time, due to the large input rate (1 MHz). For this reason the algorithm selects events on the basis of few measured quantities coming from fast detectors. In particular, the events are selected if the number of hits (N_{SPD}^{hits}) in the Scintillator Pad Detector (SPD) is less than a given threshold and if there is at least one cluster in the Hadronic Calorimeter (HCAL) with a transverse energy (E_{HCAL}^T) greater than a given energy. The values used for the 2011 and 2012 runs for the `L0Hadron` trigger requirements are listed in Tab. 3.2.

Cut Type	2011	2012
N_{SPD}^{hits}	< 600	< 600
E_{HCAL}^T	> 3.5 GeV/c^2	> 3.62 GeV/c^2

Table 3.2: List of L0 selection cuts used in the `L0Hadron` trigger line.

The `Hlt1TrackAllL0` trigger algorithm receives the output from the previous trigger level and further reduces the rate in three steps, imposing additional cuts. In the first step, an event is accepted requiring the number of hits in the Outer Tracker (N_{OT}^{hits}), Inner Tracker (N_{IT}^{hits}) and in the Vertex Locator (N_{VELO}^{hits}) to be smaller than given thresholds, listed in Tab. 3.3. In the second step the algorithm reconstructs the primary vertices and the VELO track segments. In this step, the VELO segments are requested to have a difference between the expected and observed VELO hits (N_{VELO}^{miss}) less than 3, a number of hits in the VELO (N_{VELO}^{hits}) greater than 9 and a minimum impact parameter (IP_{VELO}) with respect to all primary vertices greater than 100 μm. In the third step, the trigger algorithm uses the survived VELO segments to fully reconstruct the forward tracks. These final tracks are selected imposing further requirements on their momentum (p), transverse momentum (p_T), and number of hits in the tracking system ($N_{Tracking}^{hits}$). The selected tracks are then re-fitted using a BiDirectional Kalman filter and are required to have a χ^2/d.o.f. under a certain threshold and an impact parameter with respect to all the primary vertices greater than 16. The algorithm then selects the events with at least one track surviving the three steps mentioned above. All the cuts imposed by the `Hlt1TrackAllL0` trigger algorithm are listed in Tab. 3.3 separated for 2011 and 2012 data taking conditions.

Cut Type	2011	2012
N_{OT}^{hits}	< 15000	< 15000
N_{IT}^{hits}	< 3000	< 3000
N_{VELO}^{hits}	< 10000	< 10000
N_{VELO}^{miss}	< 3	< 3
N_{VELO}^{hits}	> 9	> 9
IP_{VELO} [μm]	> 100	> 100
p [GeV/c]	> 10	> 3
p_T [GeV/c]	> 1.7	> 1.7
$N_{Tracking}^{hits}$	> 16	> 16
χ^2_{Track}	< 2	< 1.5
χ^2_{Vertex}	> 16	> 16

Table 3.3: List of HLT1 selection cuts used in the `Hlt1TrackAllL0` trigger line.

The `Hlt2B2HH` trigger algorithm receives the events that survived the first two trigger levels and performs an online reconstruction of the $H_b \to h^+h'^-$ candidates using pairs of oppositely charged tracks. The candidates are selected by imposing cuts on the daughter particles and on the b hadron. In particular, requirements on the transverse momentum (p_T^{Track}), impact parameter (IP^{Track}) and quality of reconstruction (χ^2_{Track}/d.o.f.) are imposed on each track used to form the H_b hadron. Moreover, the algorithm cuts on the reconstructed invariant mass under the pion hypothesis for both the daughter tracks

($m_{\pi^+\pi^-}$) and on the distance of closest approach (DOCA) of the two final state particles. Finally, requests on the b hadron impact parameter (IP_{H_b}), the time of flight computed under the $\pi\pi$ hypothesis ($t_{\pi\pi}$), and the transverse momentum $p_T^{H_b}$ are imposed. A summary of the cuts is reported in Tab. 3.4.

Cut Type	2011/2012
Track p_T [GeV/c]	> 1.0
Track IP [μm]	> 120
Track χ^2/d.o.f.	< 5
$m_{\pi^+\pi^-}$ [GeV/c^2]	[4.7,5.9]
DOCA [μm]	< 100
IP_{H_b}[μm]	< 120
$t_{\pi\pi}$ [ps]	> 0.6
$p_T^{H_b}$ [GeV/c]	> 1.2

Table 3.4: List of HLT2 selection cuts used in the `Hlt2B2HH` trigger line.

3.1.2 Stripping

The events that pass the trigger requirements are then selected by means of pre-selection algorithms. This procedure, within the LHCb Collaboration, takes the name of *stripping* and is centrally managed.

In this analysis we have used data selected by means of the `B2HHBDT` stripping line. This algorithm implements the same cuts used by the `Hlt2B2HH` trigger algorithm to select $H_b \to h^+h'^-$ candidates (except for the daughter tracks χ^2/d.o.f., now requested to be less than 3); note that being an offline selection, thus not limited by timing constrains, the stripping uses quantities reconstructed with better quality with respect to the trigger algorithm. Then, a multivariate analysis technique based on boosted decision trees (BDT) is employed in order to further discriminate between signal and background events. The BDT algorithm takes its decision on the basis of the variables reported in Tab. 3.5.

3.1.3 Monte Carlo samples

We use samples of fully simulated Monte Carlo (MC) signal events. In these samples the 2011 and 2012 data taking conditions have been reproduced in order to have events comparable with the real data. The MC data are generated in two different samples, one for each year, reproducing the observed ratio between 2011 and 2012 integrated luminosities. Moreover, the ratio between the statistics collected with different magnet polarities is also respected.

BDT variables		
$\min(p_T^+, p_T^-)$	DOCA	$p_T^{H_b}$
$\max(p_T^+, p_T^-)$	χ^2_{Vertex}	IP_{H_b}
$\min(IP^+, IP^-)$		FD_{H_b}
$\max(IP^+, IP^-)$		

Table 3.5: Variables used to train the BDT algorithm employed in the stripping procedure. Note that with FD_{H_b} we indicate the flight distance of the b hadron.

All these samples are obtained using various software packages. In particular, pp collisions are generated using the PYTHIA generator [59, 60], adapted to LHCb through specific configurations [61]. The b hadron decays are described by EvtGen [62]; moreover, in order to treat correctly the final state soft photon emission, outlined in detail in the signal model paragraph 3.3.1, the PHOTOS generator [63] is employed. Finally, the interaction of the generated particles with the detector materials and the detector response are simulated using the Geant toolkit [64, 65], as described in [66].

3.2 Calibration of particle identification

Particle identification (PID) is of fundamental importance in all this analysis. As the kinematic cuts used to select the various $H_b \to h^+ h'^-$ candidates are the same for all channels, the only way to distinguish one channel from another is to use different PID cuts. In addition, the efficiencies of PID requirements are needed to determine the amount of other $H_b \to h^+ h'^-$ decays, where one or both the final state particles have been mis-identified, contaminating the invariant mass spectra of the considered signals.

In order to calibrate the response of RICH detectors high statistics and high purity samples of pions, kaons and protons are needed. Thanks to the large D^* production cross-section and to their particular kinematic characteristics, $D^{*+} \to D^0(K^-\pi^+)\pi^+$ decays[1] can be used as a source of large samples of pions and kaons selected without the application of any PID cut. Likewise, $\Lambda \to p\pi^-$ decays are suitable calibration samples for protons. The residual background contamination has been removed from these samples using the *s$\mathcal{P}$lot* technique [67]. In Fig. 3.1 the distributions of the variable $\Delta m = m(D^*) - m(D^0)$ for $D^{*+} \to D^0(K^-\pi^+)\pi^+$ and of the invariant mass of $\Lambda \to p\pi^-$ are shown. Note that in Fig. 3.1 only a part of the calibration samples (each containing $\sim$ 100 M events) is shown. The superimposed curves are the result of the maximum likelihood fits to the spectra used to unfold the variables relative to true pions, kaons and protons.

[1] Throughout this chapter, unless stated otherwise, charge conjugation is always implied.

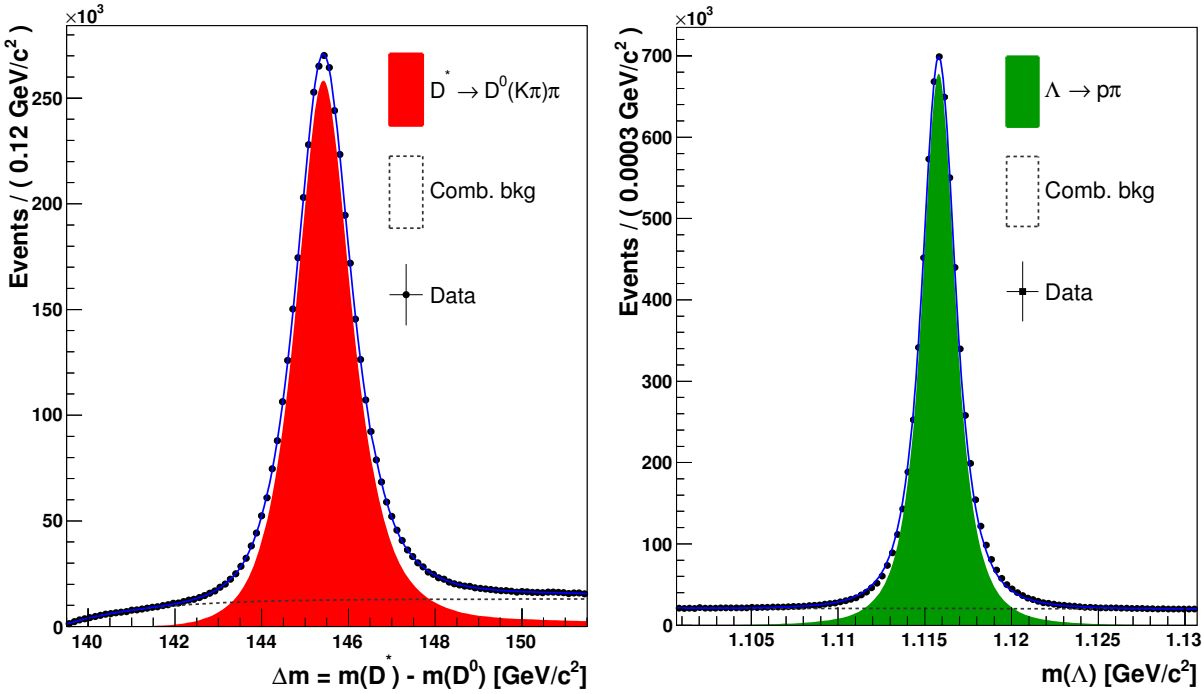

Figure 3.1: Distribution of the variable $\Delta m = m(D^*) - m(D^0)$ (left) and invariant mass spectrum of $\Lambda \to p\pi^-$ decay. The results of binned maximum likelihood fits are superimposed.

The procedure of PID calibration has been developed taking into account the following considerations:

- Since the aim is to distinguish between three kind of particles (pions, kaons and protons) a complete set of PID discriminators consists of two $\Delta \log \mathcal{L}$ variables as defined in Eq. (2.2). For example, in order to select kaons we need to apply requirements on both $\Delta \log \mathcal{L}_{K-\pi}$ (in order to reject pions) and $\Delta \log \mathcal{L}_{K-p}$ (in order to reject protons). If a particle survives the cuts defined to select kaons, then the kaon hypothesis is assigned to that particle.

- The value of $\Delta \log \mathcal{L}$ depends directly from the momentum of the particle through its relation with the emission angle of Cherenkov photons. In addition, since the two RICH detectors have different angular acceptance and have radiators optimized for different momentum regions, the values of $\Delta \log \mathcal{L}$ show a dependence also on the pseudo-rapidity (η) of the particle.

- Several studies [58] performed by the LHCb collaboration showed a degradation

of RICH performances in events with high occupancy. This effect can be parameterized studying the dependence of $\Delta \log \mathcal{L}$ with respect to the number of tracks (N^{tracks}) in the event.

- The kinematics of particles coming from $H_b \to h^+h'^-$ decays is different from the kinematics of pions, kaons and protons contained in the calibration samples. This is evident from the distributions reported in Fig. 3.2, where background subtracted calibration samples are compared with samples of $H_b \to h^+h'^-$ decays from MC events.

- The distribution of N^{tracks} in $H_b \to h^+h'^-$ events results to be slightly different with respect to the distribution observed in the calibration samples. This difference is shown in Fig. 3.3, where the distributions of N^{tracks} for $D^{*+} \to D^0(K^-\pi^+)\pi_s^+$, $\Lambda \to p\pi$ and $H_b \to h^+h'^-$ events are superimposed.

As a first step of the calibration procedure, for a given set of PID requirements, maps of PID efficiencies in bins of p, η and N^{tracks} are determined applying the cuts to the $\Delta \log \mathcal{L}$ variables of the calibration samples. For example, in a given region of p, η, and N^{tracks} the efficiency of a PID cut applied to kaons, is given by the number of calibration kaons surviving that PID requirement divided by the total number of calibration kaons in that region. Since the number of tracks in the event is uncorrelated from the kinematic of the decay, it turns out to be useful to integrate out the dependence of PID efficiencies with respect to N^{tracks}. This is done by averaging the PID efficiencies in each bin of p and η according to the distribution of N^{tracks} for $H_b \to h^+h'^-$ events shown in Fig. 3.3. The integration can be formalized in the following equation:

$$\bar{\varepsilon}\left(p,\eta\right) = \frac{1}{N}\sum_{i=0}^{N} \varepsilon\left(p,\eta,N_i^{tracks}\right) \tag{3.3}$$

where $\bar{\varepsilon}\left(\cdot\right)$ is the final PID efficiency for the bin defined by p and η; $\varepsilon\left(\cdot\right)$ is the PID efficiency for the bin corresponding to p, η and N_i^{tracks}; N_i^{tracks} is a random number extracted according to the distribution of N^{tracks} of $H_b \to h^+h'^-$ events, shown in Fig. 3.3; N is a number large enough to avoid statistical fluctuation in the averaging procedure (several trials proved $N = 100000$ to be sufficiently large without consuming too much computing power). The final outcomes of this procedure are the maps of PID efficiencies in bins of p and η for particles coming from $H_b \to h^+h'^-$ decays. As a reference, in Fig. 3.4 we report the PID efficiency maps for pions, kaons and protons relative to the requirement $\Delta \log \mathcal{L}_{K-\pi} > 3$ AND $\Delta \log \mathcal{L}_{K-p} > -5$.

The efficiency of a PID requirement applied on a $H_b \to h^+h'^-$ decay is estimated using the following equation:

$$\varepsilon_{h^+h'^-} = \frac{1}{N}\sum_{i=1}^{N} \bar{\varepsilon}_{h^+}\left(p_i^+,\eta_i^+\right)\cdot\bar{\varepsilon}_{h'^-}\left(p_i^-,\eta_i^-\right), \tag{3.4}$$

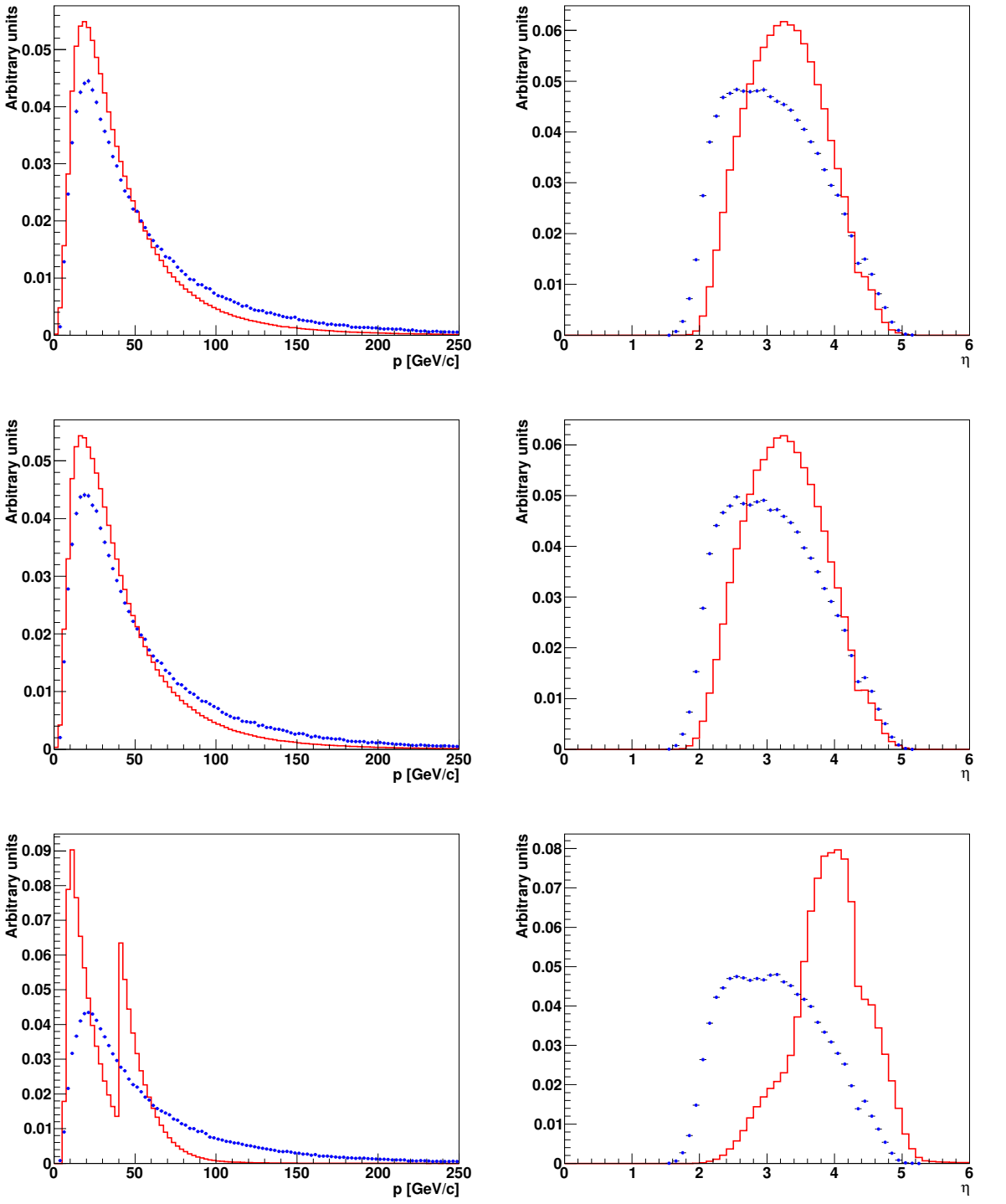

Figure 3.2: Comparison between the p (left) and η (right) distributions for kaons (top), pions (middle) and protons (bottom) coming from the fully simulated $H_b \to h^+h'^-$ decays (blue dots) and from the calibration samples (red line). It is evident that the distributions are different in each case. The distributions are normalized to unitary area.

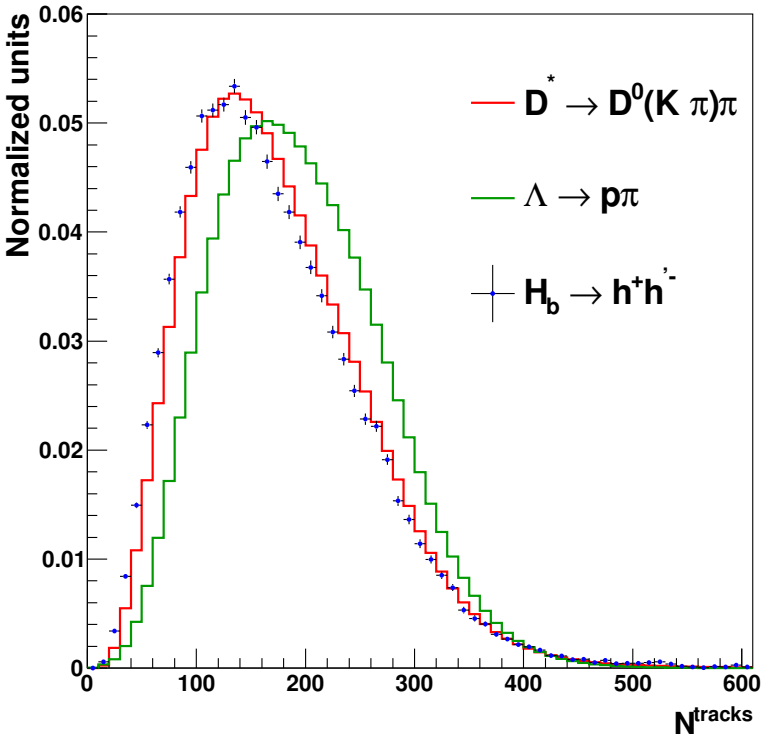

Figure 3.3: N^{tracks} distribution relative to the calibration samples coming from $D^* \to D^0(K\pi)\pi$ (red line) and $\Lambda \to p\pi$ (green line) decays. We also show the distributions of N^{tracks} for the $H_b \to h^+h'^-$ candidates with the associated error (blue dots).

where N is the number of $H_b \to h^+h'^-$ candidates, $\bar{\varepsilon}_{h^+}(\cdot)$ and $\bar{\varepsilon}_{h'^-}(\cdot)$ are the efficiencies as a function of p and η as determined from Eq. (3.3), $p_i^{+(-)}$ and $\eta_i^{+(-)}$ are the momentum and the pseudo-rapidity of the positive (negative) particle belonging to the i-th candidate. Candidates from fully simulated MC events are used.

3.2.1 Determination of PID efficiencies for $\Lambda_b^0 \to pK^-$ and $\Lambda_b^0 \to p\pi^-$

The case for the Λ_b^0 decays is different from that of the B meson decays, due to the fact that the distributions of p and η in the calibration sample for protons does not cover all the p and η phase space occupied by the protons coming from Λ_b^0 decays. We report the plots of the various particle distributions in the $p-\eta$ phase space for calibration samples and simulated $H_b \to h^+h'^-$ events in Fig. 3.5 and 3.6, respectively. To address this issue use samples of simulated $\Lambda_b^0 \to pK^-$ and $\Lambda_b^0 \to p\pi^-$ decays.

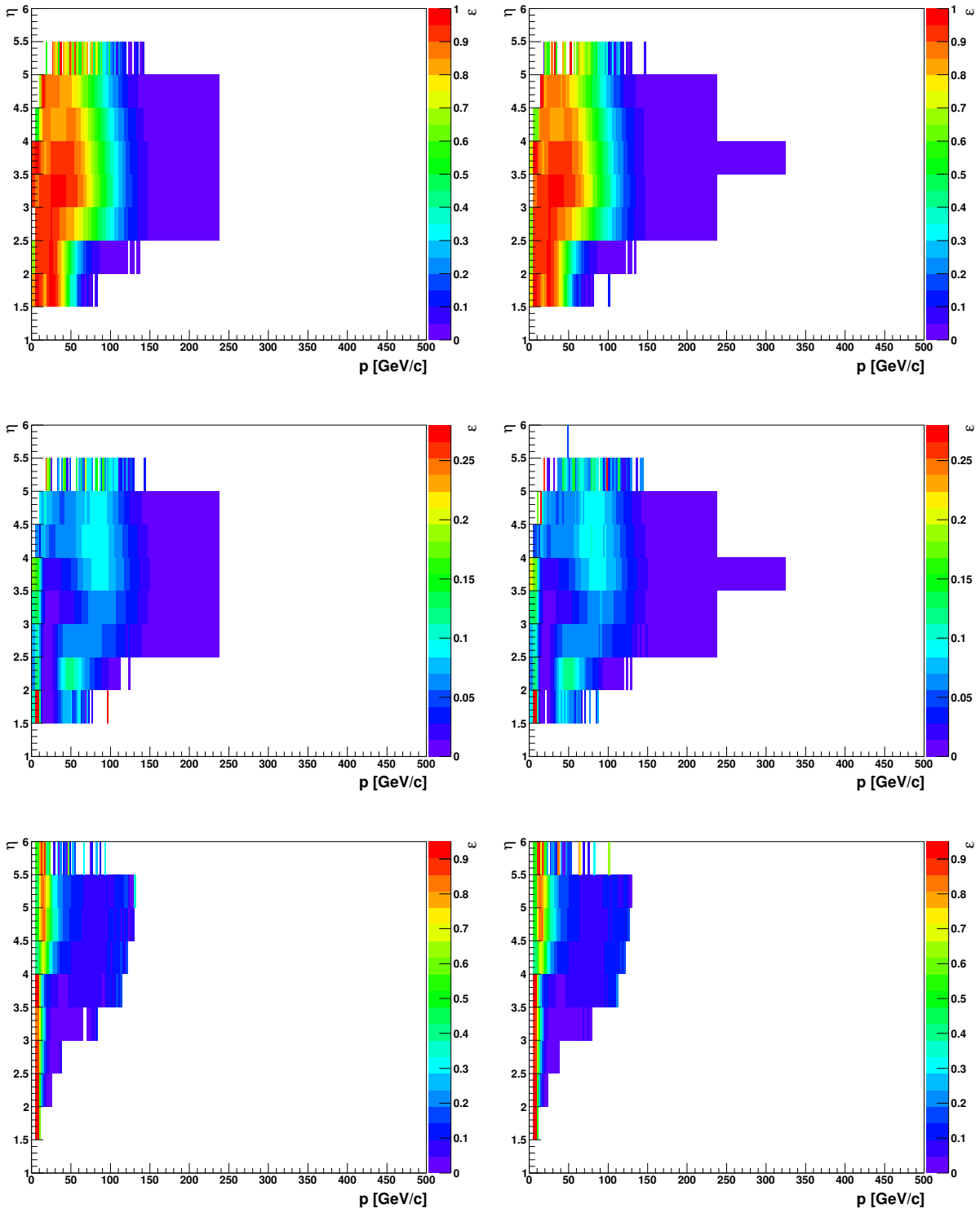

Figure 3.4: Kaon PID efficiencies after the cuts $\Delta \log \mathcal{L}_{K-\pi} > 3$ and $\Delta \log \mathcal{L}_{K-p} > -5$ under the kaon (first row), pion (second row) and proton (third row) hypothesis in bins of p and η. The first column contains the cases K^-, π^- and $\bar{p}$ while the second contains the cases K^+, π^+ and p.

First of all we define two zones in the $p - \eta$ plane, called fiducial and non-fiducial regions. The fiducial region is determined through different cuts on p and η as the zone where the calibration sample for protons contains a significant number of events. The non-fiducial zone covers the remaining phase space, where there are no events from the calibration sample. The fiducial region can be expressed in terms of conditions on the values of p and η of the protons as:

$$\begin{aligned}
&(\eta > p \cdot m_1 + q_1 \text{ AND } p \leq 40 \text{ GeV/c}) \text{ OR} \\
&(\eta > p \cdot m_2 + q_2 \text{ AND } p > 40 \text{ GeV/c AND } p \leq 110 \text{ GeV/c}) \text{ OR} \\
&(\eta > p \cdot m_3 + q_3 \text{ AND } p > 110 \text{ GeV/c}).
\end{aligned} \tag{3.5}$$

The values of the parameters m_i and q_i employed to calculate such functions can be found in Tab. 3.6. In the case of protons, the boundaries between fiducial and non-fiducial

Parameter	Value
m_1	0.0382 (c/GeV)
m_2	0.0086 (c/GeV)
m_3	0.0657 (c/GeV)
q_1	1.5706
q_2	2.7571
q_3	-3.5286

Table 3.6: Parameters used in the functions that define the boundary between the fiducial and non fiducial region.

region are superimposed on the distributions in Fig. 3.5 and 3.6.

Since the non-fiducial region is not covered by the calibration sample, the only option is to determine the PID efficiency in that region applying the requirements on simulated variables. The obtained efficiency is then been rescaled by a factor that takes into account the different PID performances between simulated events and data. Such a factor is defined by the following equation:

$$\mathcal{K} = \frac{\varepsilon_F}{\varepsilon_F^{MC}} \tag{3.6}$$

where ε_F is the PID efficiency in the fiducial region calculated applying the calibration procedure described in the previous paragraph by Eq. (3.4) and ε_F^{MC} is the PID efficiency relative to the fiducial region determined from MC events. The final efficiency is then calculated by:

$$\varepsilon = f \cdot \varepsilon_F + (1 - f) \cdot \mathcal{K} \cdot \varepsilon_{NO-F}^{MC} \tag{3.7}$$

where f is the fraction of events inside the fiducial region and ε_{NO-F}^{MC} is the PID efficiency relative to the non-fiducial region determined from MC events.

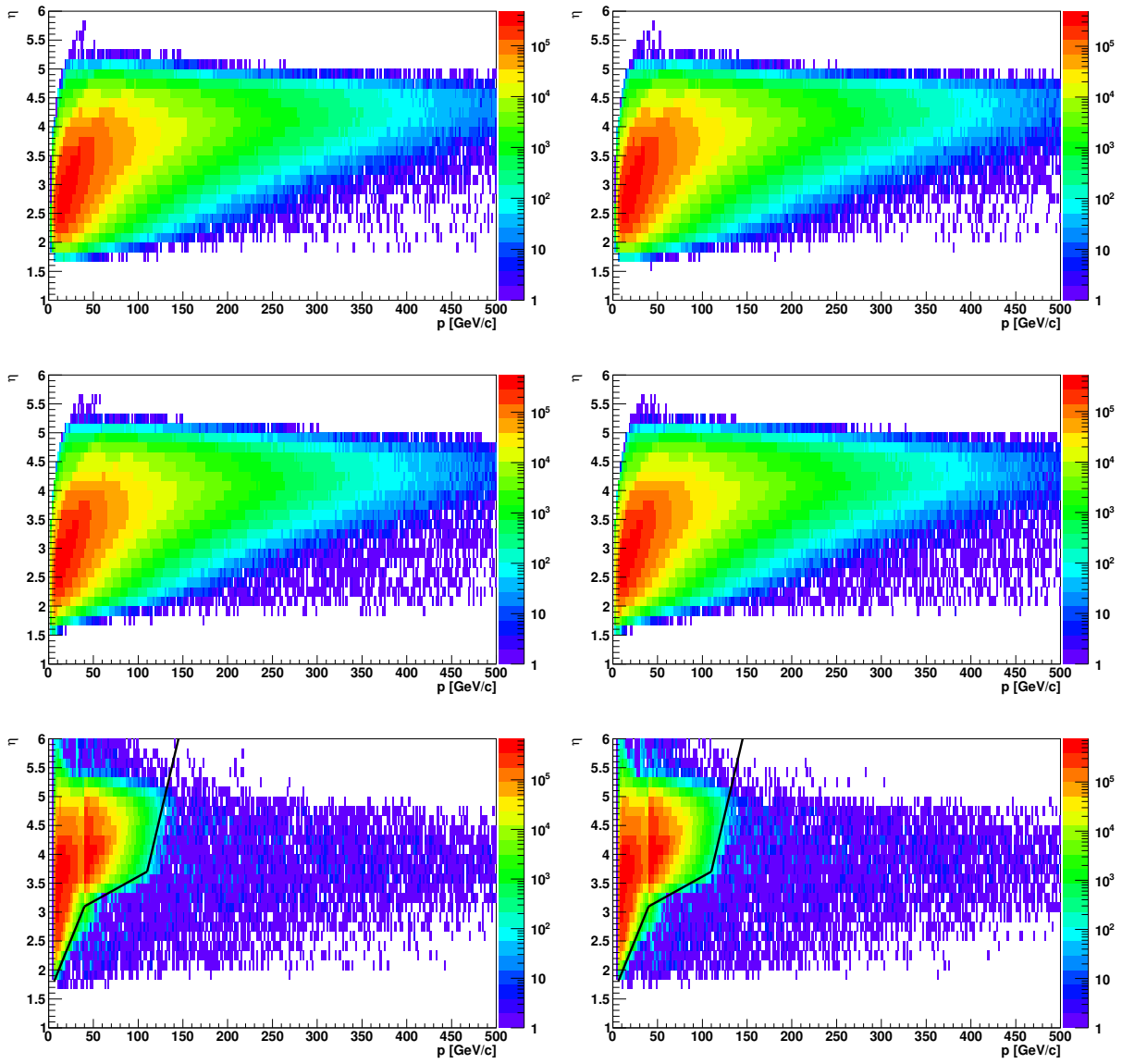

Figure 3.5: $p-\eta$ distributions for the K^- (top-left), K^+ (top-right), π^- (middle-left), π^+ (middle-right), p (bottom-left) and $\bar{p}$ (bottom right) coming from the calibration samples $D^* \to D^0(K\pi)\pi_s$ (pions and kaons) and $\Lambda^0 \to p\pi$ (protons). The colored scale indicates the number of events. The black line drawn in the last two plots represents the boundary between the fiducial region (on the left of the boundary) and the non fiducial region (on the right of the boundary) as defined in Eq. (3.5).

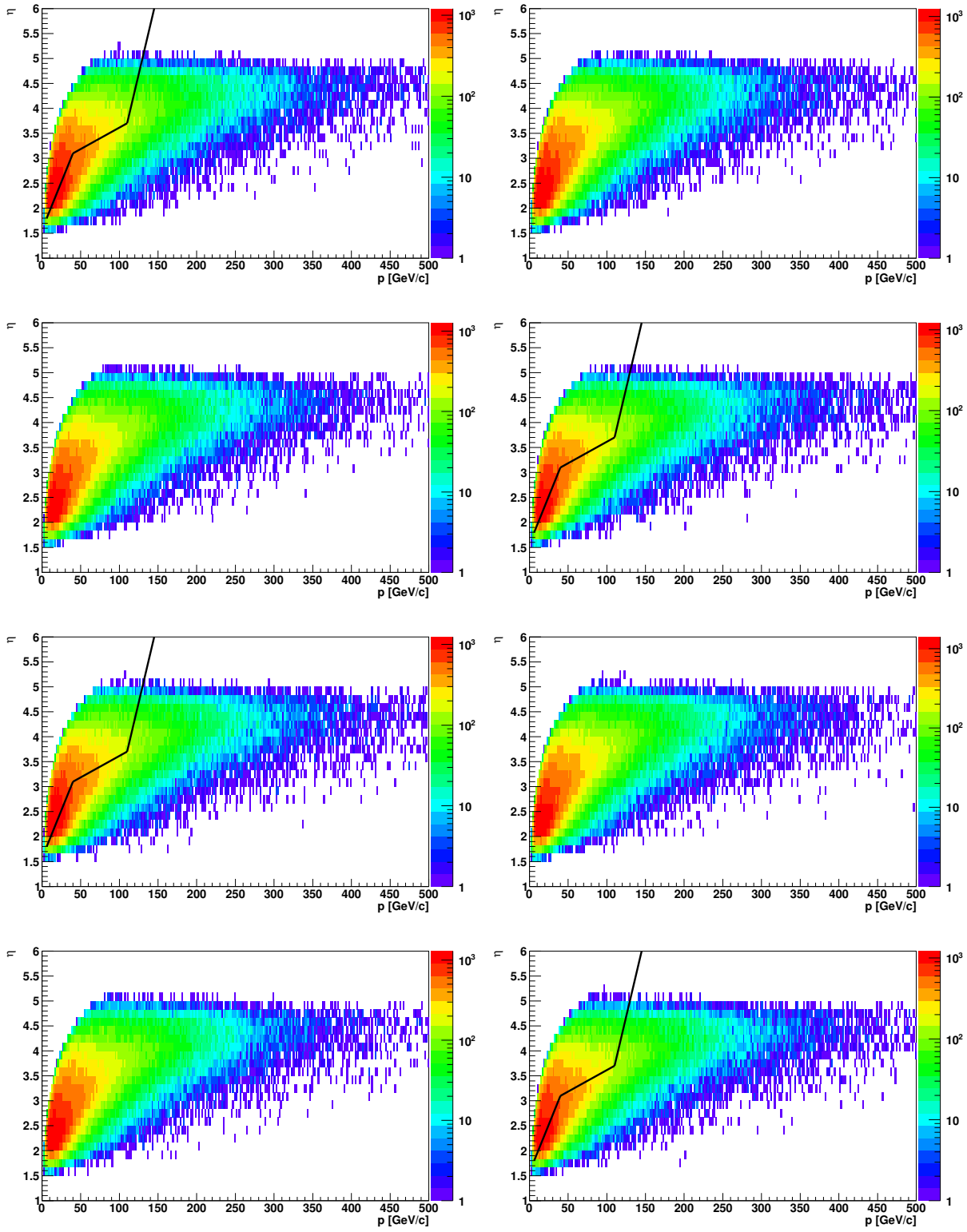

Figure 3.6: $p - \eta$ distributions for the $\Lambda_b^0 \to pK^-$ (first row), $\Lambda_b^0 \to K^+\bar{p}$ (second row), $\Lambda_b^0 \to p\pi^-$ (third row) and $\Lambda_b^0 \to \pi^+\bar{p}$ (fourth row) from the MC data samples (the colored scale indicates the number of events). The first column contains the plots relative to the positive particle present in each decay while the second column contains the plots relative to the negative particle present in each decay. The black line drawn in the p and $\bar{p}$ plots represent the boundary between the fiducial region (on the left of the boundary) and the non fiducial region (on the right of the boundary) as defined in Eq. (3.5).

3.3 Invariant mass model

The raw asymmetries are extracted from data by performing binned maximum likelihood fits to the invariant mass spectra. For a more detailed description of the theoretical basis of maximum likelihood fits see Appendix B.

We identify 4 main components contributing to the spectra:

Signal: $H_b \to h^+h'^-$ decays where the final state particles are correctly identified by the PID cuts;

Cross-feed background: $H_b \to h^+h'^-$ decays in which the identity of one or both the final state particles are wrongly assigned. This background is particularly dangerous since it peaks under the signal shape formed by the correctly reconstructed decays;

Partially reconstructed background: components coming from $H_b \to h^+h'^-X$ multibody decays where only the two h^+ and h'^- hadrons are used to form the parent H_b.

Combinatorial background: candidates composed by pairs of oppositely charged tracks not coming from the same decay chain.

3.3.1 Signal model

In order to correctly parametrize the signal shape we have to consider the effect of soft photons emission by the final state particles of the $H_b \to h^+h'^-$ decays. This is the so-called final state radiation and it can be accurately treated with quantum electrodynamics (QED).

According to Ref. [69] the differential decay rate to $\mathcal{O}(\alpha)$ of a $B \to hh' + n\gamma$ decay, where n stands for any number of emitted photons, can be expressed as:

$$\frac{\mathrm{d}\Gamma_{12}^{incl}}{\mathrm{d}E} = \frac{2\alpha}{\pi}\frac{|b_{12}|\Gamma_{12}^0}{E}\left(\frac{2E}{m_B}\right)^{\frac{2\alpha}{\pi}|b_{12}|} \tag{3.8}$$

where E is the sum of the energies of the emitted photons in the center-of-mass system of the decaying B hadron, Γ_{12}^0 stands for the pure weak decay rate, overwhelmed by the strong decay rate and thus unobservable, m_B is the mass of the B that is decaying and α is the the coupling constant characterizing the strength of the electromagnetic interaction. The term b_{12} is given by the equation:

$$b_{12} = \frac{1}{2} - \frac{4 - \Delta_1^2 - \Delta_2^2 + 2\beta^2}{8\beta}\log\left(\frac{\Delta_1 + \beta}{\Delta_1 - \beta}\right) + (1 \to 2) \tag{3.9}$$

where

$$\Delta_{1(2)} = 1 + r_{1(2)}^2 - r_{2(1)}^2, \qquad r_i = \frac{m_i}{m_B}, \quad i = 1, 2 \tag{3.10}$$

and

$$\beta = \sqrt{[1 - (r_1 + r_2)^2][1 - (r_1 - r_2)^2]} \tag{3.11}$$

with m_1 and m_2 masses of the two particles forming the final state. If we consider for simplicity the case of a single photon emission, then we can write m_B as:

$$m_B = (E_1 + E_2 + E_\gamma) \tag{3.12}$$

where E_1, E_2 and E_γ are the energies of the two final state particles and of the photon in the center-of-mas system of the B, where by definition we have:

$$\vec{p}_1 + \vec{p}_2 + \vec{p}_\gamma = 0 \ . \tag{3.13}$$

The invariant mass of the two final state particles can be written as:

$$m_{12}^2 = (E_1 + E_2)^2 - (\vec{p}_1 + \vec{p}_2)^2 = (E_1 + E_2)^2 - E_\gamma^2 \tag{3.14}$$

and so we conclude that:

$$m_{12} = m_B \sqrt{1 - \frac{2E_\gamma}{m_B}} \simeq m_B - E_\gamma \tag{3.15}$$

where we have expanded in Taylor series the square root since $E_\gamma / m_B \ll 1$. We have just demonstrated that the reconstructed mass is equal to the B mass shifted by an amount equal to the energy of the emitted photon, that is distributed according to Eq. (3.8). It can then be shown that the reconstructed mass is distributed according to a function of the form (neglecting resolution effects due to the detector):

$$f(m) = A[\Theta(m - m_B)(m - m_B)^s] \tag{3.16}$$

where

$$s = \frac{2\alpha}{\pi}|b_{12}| - 1 \ , \tag{3.17}$$

A is a normalization factor, and $\Theta(\cdot)$ is a step function. We can take into account the finite resolution effects due to the detector by calculating the convolution product of two Gaussian p.d.f.'s with zero mean with the function defined in Eq. (3.16), obtaining:

$$g(m) = \Theta(m_B - m') \cdot A \cdot (m_B - m')^s \otimes G_2(m - m';\ f_1, \sigma_1, \sigma_2) \tag{3.18}$$

where $G_2(\cdot)$ stands for the sum of the two Gaussians p.d.f.'s.

The p.d.f. reported in Eq. (3.18) is not yet sufficient to reproduce the invariant mass shape of reconstructed $B \to h^+ h'^-$ decays with high accuracy. In Ref. [70] it has been

observed that the final state reconstruction efficiency is dependent from the invariant mass value. In the study it has been shown that such a dependence can be parametrized as:

$$\varepsilon_m(m) \propto 1 + p_m \cdot |m - m_B| \tag{3.19}$$

where m is the reconstructed mass for the event and m_B is the mass of the B candidate. Thus, the p.d.f. used for the signal component has the form:

$$g(m) = A' \cdot \varepsilon_m(m) \cdot [\Theta(m_B - m') \cdot (m_B - m')^s \otimes G_2(m - m'; f_1, \sigma_1, \sigma_2)] \tag{3.20}$$

where $\varepsilon_m(m)$ is the efficiency function and A' is a normalization factor.

Note that the formalism outlined above just applies to decays of B mesons to two pseudo-scalars, hence it is not strictly valid for the two Λ_b^0 modes. Nonetheless, we have used the same p.d.f. in fits to the two Λ_b^0 modes. It can be seen that indeed the p.d.f. fits very well to all the invariant mass distributions, with results which are consistent to those of the B meson fits.

In order to validate this model we perform binned maximum likelihood fits of fully simulated $H_b \to h^+h'^-$ decays. As an example, we report the fit to the $\Lambda_b^0 \to p\pi^-$ and $B_s^0 \to K^+K^-$ invariant mass spectra in Fig. 3.7. The final state photon radiation is simulated with the PHOTOS software [63] for all the decay modes. We report in Tab. 3.7 the values of the s paramater as calculated by employing Eq. (3.17) for each $H_b \to h^+h'^-$ decay. We also list in the same table the value of the s and p_m parameters obtained as a result of the model validation procedure. These parameters are then fixed in the final fit.

The agreement between the theoretical prediction and the measured value of s is quite good. The small differences can be taken into account assigning a systematic uncertainty. However, the determination of systematic uncertainties is not covered in this thesis.

3.3.2 Cross-feed background model

When a wrong mass hypothesis is assigned to the final state particles of a $H_b \to h^+h'^-$ candidate, the spectrum of the reconstructed invariant mass is altered. Since this effect cannot be easily parametrized, in order to study the shapes of the cross-feed invariant mass spectra we have used MC data samples. In doing this we have to take into account the fact that the invariant mass resolution in MC events underestimates the invariant mass resolution observed in data.

The reproduction of invariant mass spectra of cross-feed backgrounds is performed in two steps. First of all for each MC event we compute the wrong invariant mass assuming perfect resolution. For example, the reconstructed invariant mass of any two-body decay under the $h^+h'^-$ final state hypothesis can be written as:

$$m_W(h^+h'^-) = \sqrt{m_{h^+}^2 + m_{h'^-}^2 + 2\left(\sqrt{(m_{h^+}^2 + p_+^2)(m_{h'^-}^2 + p_-^2)} - \vec{p}_+ \cdot \vec{p}_-\right)}\,, \tag{3.21}$$

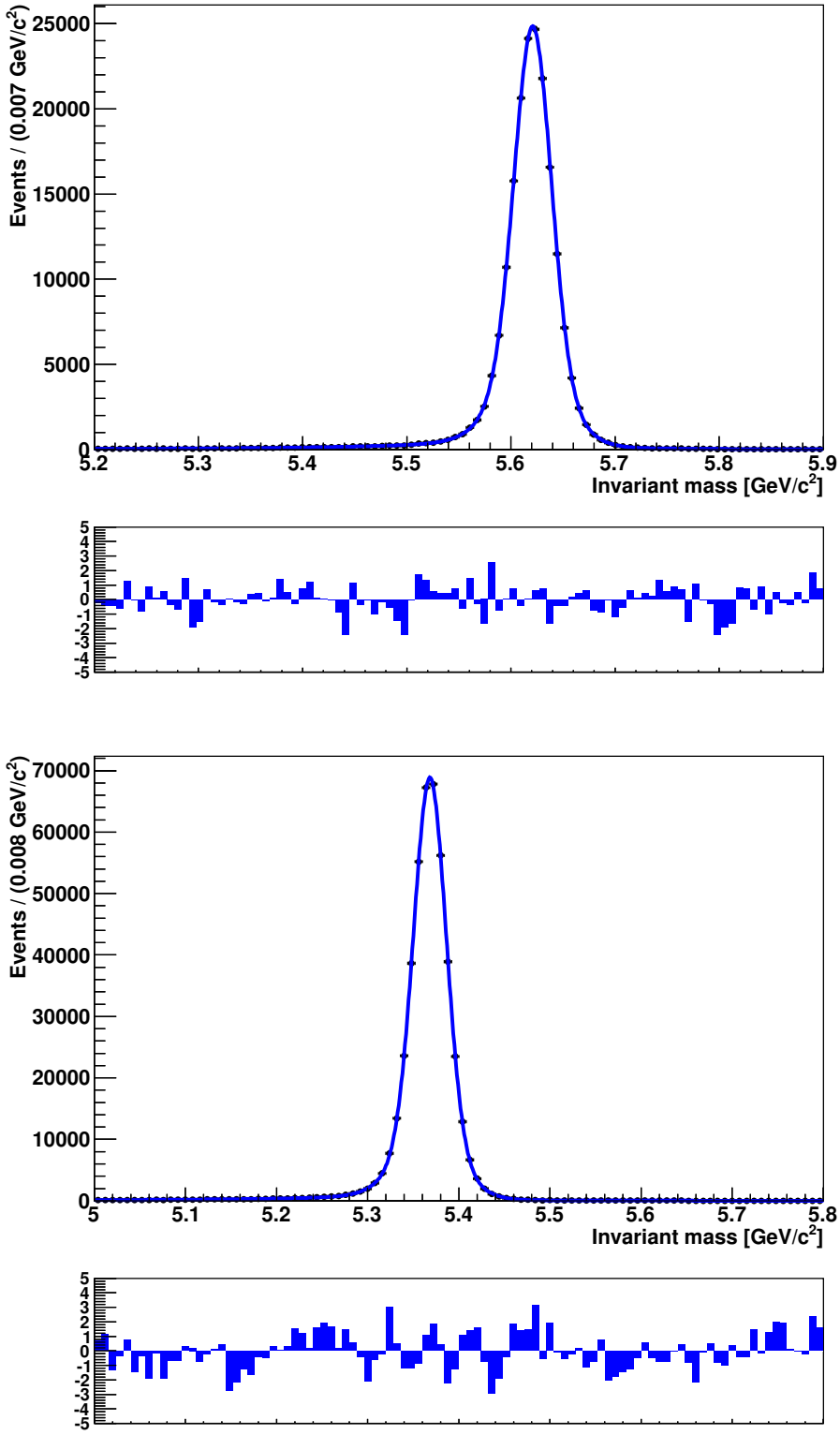

Figure 3.7: Invariant mass spectra relative to the Monte Carlo $\Lambda_b^0 \to p\pi^-$ (top) and $B_s^0 \to K^+K^-$ (bottom) decays respectively. The blue curve superimposed is the result of a binned maximum likelihood fit.

Decay channel	s_{theo}	s_{MC}	p_m [c^2/GeV]
$B^0 \to \pi^+\pi^-$	-0.9709	-0.9684 ± 0.0006	-1.05 ± 0.10
$B_s^0 \to \pi^+\pi^-$	-0.9709	-0.9685 ± 0.0006	-1.07 ± 0.07
$B^0 \to K^+K^-$	-0.9826	-0.9826 ± 0.0005	-1.26 ± 0.15
$B_s^0 \to K^+K^-$	-0.9826	-0.9829 ± 0.0004	-1.00 ± 0.09
$B^0 \to K^+\pi^-$	-0.9768	-0.9750 ± 0.0007	-1.26 ± 0.14
$B_s^0 \to \pi^+K^-$	-0.9766	-0.9756 ± 0.0008	-1.08 ± 0.12
$\Lambda_b^0 \to pK^-$	-0.9852	-0.9854 ± 0.0006	-0.99 ± 0.13
$\Lambda_b^0 \to p\pi^-$	-0.9793	-0.9792 ± 0.0006	-0.97 ± 0.10

Table 3.7: Value of the parameters needed to parametrize the signal model expressed by Eq. (3.20). The first column contains the s parameter calculated through Eq. (3.17) for each H_b decay channel; the second and third column contain the values of the s and p_m parameters obtained from the model validation procedure.

where m_{h^+} and $m_{h'^-}$ are the masses relative to the final state hypothesis, $\vec{p}_{+(-)}$ is the momentum of the positive (negative) final state particle obtained from the simulation and $p_{+(-)}$ stand for the module of $\vec{p}_{+(-)}$.

Then, to reproduce resolution effects observed in data we add a smearing to each event, extracting a random number according to the invariant mass resolution model that fits the data. The last effect to take into account is the fact that the PID cuts deform the invariant mass distributions obtained through the procedure described above. This is a consequence of the fact that PID cuts alter the momentum distribution of tracks. To address this, we assign a weight to each MC event due to the PID efficiencies; this weight is obtained from the $p-\eta$ efficiency maps calculated in the previous section, multiplying the two PID efficiencies relative to the final state particles under consideration. As an example in the left part of Fig. 3.8 we show the invariant mass spectrum of $\Lambda_b^0 \to pK^-$ decays when reconstructed under the K^+K^- hypothesis. The blue histogram represents the invariant mass spectrum before the application of PID cuts, while the red histogram represents the same spectrum after the application of PID cuts.

Finally, to obtain the cross-feed shapes, we apply a one-dimensional Kernel Estimation technique [71] to the mass distributions. This technique models the distribution of an arbitrary input dataset as a superposition of Gaussian kernels, one for each data point, each contributing proportionally to the weight assigned to the point. As an example, we show in the right part of Fig. 3.8 the results of the Kernel Estimation technique applied to the two invariant mass distributions on the left of the figure.

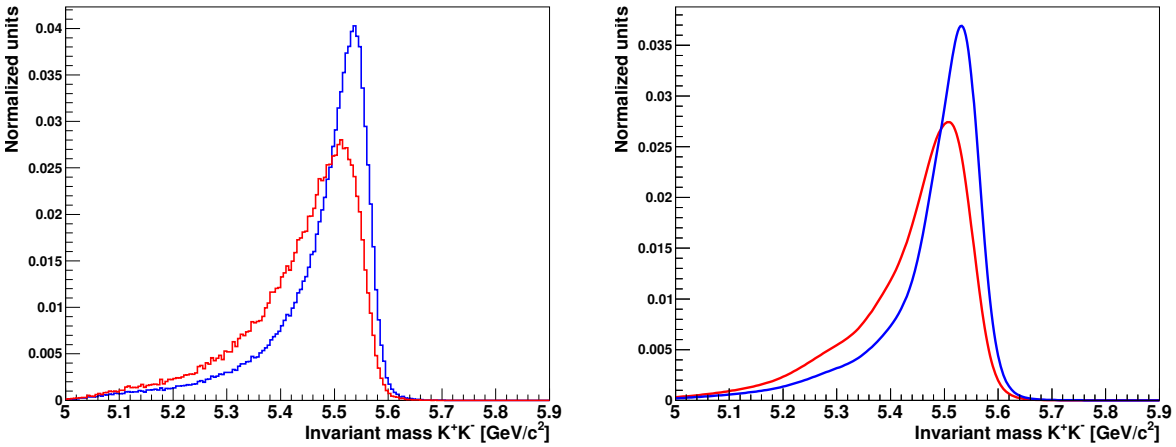

Figure 3.8: Invariant mass distributions for the wrong mass calculated by Eq. (3.21) for the $\Lambda_b^0 \to pK^-$ decay reconstructed under the K^+K^- final state hypothesis (left) and p.d.f.'s shapes obtained using a Kernel Estimation technique applied on a sub-sample of the same data (right). In the figures, the blue line represents the distribution and the relative p.d.f. without taking into account the deformation induced by PID cuts, while the red line represents the weighted distribution and the relative p.d.f., where the weights are calculated using the PID efficiencies.

3.3.3 Partially reconstructed multi-body H_b decays

This type of background originates from partially reconstructed decays where one or more final state particles are not reconstructed. As a consequence, the invariant mass of the considered particle is shifted at least by an amount equal to the invariant mass of the lost particles. The main components contributing to $p\pi^-$ and pK^- invariant mass spectra come from partially reconstructed $\Lambda_b^0 \to pK^-\pi^0$ and $\Lambda_b^0 \to p\pi^-\pi^0$ decays, respectively; the same is true for the $\pi^+\pi^-$, K^+K^-, and $K^+\pi^-$ spectra, where the main partially reconstructed background is given by $B^0 \to \pi^\pm\pi^\mp\pi^0$, $B^0_{(s)} \to K^\pm K^\mp\pi^0$, and $B^0_{(s)} \to K^\pm\pi^\mp\pi^0$ decays, respectively.

These components are empirically modelled with an ARGUS function [72] convolved with an invariant mass resolution model:

$$f(m) = A \cdot \left[m' \sqrt{1 - \frac{m'^2}{m_0^2}} \Theta(m_0 - m') e^{c_i \frac{m'}{m_0}} \right] \otimes G_2(m - m'; f_1, \sigma_1, \sigma_2) \ , \qquad (3.22)$$

where A is a normalization factor, $\Theta(\cdot)$ is a step function, m_0 and c are two parameters governing the shape of the ARGUS function, $\otimes$ stands for the convolution product and $G_2(\cdot)$ is the same invariant mass model used for the signal shapes.

From Eq. (3.22) it is clear that the parameter m_0 represents the end point of the ARGUS function. Since the main source of partially reconstructed background comes from the decays where a π^0 is not reconstructed, m_0 is centered at $m_{B^0} - m_\pi = 5.144$ GeV/c^2, $m_{B_s^0} - m_\pi = 5.232$ GeV/c^2 or $m_{\Lambda_b^0} - m_\pi = 5.484$ GeV/c^2 for the B^0, B_s^0 and Λ_b^0 decays, respectively.

3.3.4 Combinatorial background model

The combinatorial background is been modeled with an exponential p.d.f.:

$$c(m) = Be^{-km} \tag{3.23}$$

where k is the exponential slope found by the fit procedure and B is a normalization factor. We use a different slope for each invariant mass spectra, employing the same slope for the charge conjugate modes.

3.4 Offline selection

The sample obtained from the pre-selection must be further refined offline in order to obtain the best statistical sensitivity on the $\mathcal{CP}$ asymmetries. The offline selection is composed of two distinct parts:

- a kinematic and geometric selection applied to all the decay channels and based on a BDT multivariate algorithm;
- a specific final state selection based on the application of PID cuts.

Note that both the selection criteria must be optimized simultaneously to obtain the combination of cuts that yields the smallest error for each $\mathcal{A}_{\mathcal{CP}}$. Before describing the offline procedure used to optimize the offline selection criteria, it is appropriate to make some considerations:

- The kinematic and geometrical cuts imposed by the BDT selection reduce the quantity of combinatorial background present in each invariant mass spectrum, while the PID requirements are needed in order to decrease the number of cross-feed (misidentified) background events. However, note that PID cuts also modify the composition and the amount of combinatorial background.
- For each set of BDT and PID cuts we need to determine the number of signal, cross-feed background, partially reconstructed background and combinatorial background events.

- The pK^- and $p\pi^-$ invariant mass spectra are formed by different components. Since the raw asymmetries are obtained fitting a model to the spectra, the sensitivity on these quantities depends not only on the amount of signal and background events in the sample, but also on the fitting model itself.

Considering this, we employ the following procedure. First of all we train a BDT for each set of PID cuts, chosen in order to cover a wide region of the $\Delta \log \mathcal{L}$ distributions. Secondly, we select different samples of fully reconstructed pK^- and $p\pi^-$ final states, one for each combination of BDT and PID requirements. Then we perform maximum likelihood fits to the invariant mass spectra, determining the relevant parameters of the model. Finally we perform ten pseudo-experiments for each set of cuts, generating and fitting the data. Thus we use the results of these pseudo-experiments to find the requirements that yield the best sensitivity on each $\mathcal{CP}$ asymmetry. The optimization procedure is performed separately and independently for the $\Lambda_b^0 \to pK^-$ and $\Lambda_b^0 \to p\pi^-$ decays, as be described in the next paragraphs.

3.4.1 Kinematic selection

In order to enhance the separation between signal and combinatorial background we employ a BDT multivariate algorithm. For a description of multivariate algorithms and BDT see Appendix A. The BDT classification is performed in two steps. First of all the BDT algorithm is trained to distinguish between signal- and background-like candidates depending on a set of variables describing the candidates. After the training, the algorithm is able to assign to each event a numerical factor μ_{BDT} ranging from -1 to $+1$. When this factor is close to -1, the event is more likely to be background, whereas to $+1$ it is more likely to be a signal. In order to train the BDT, we need two distinct samples, one composed of pure signal and one of pure background events. The signal sample is taken from the fully simulated $\Lambda_b^0 \to pK^-$ and $\Lambda_b^0 \to p\pi^-$ MC events. The background sample is extracted from real data, selecting events passing the PID cuts (used to select pK^- and $p\pi^-$ final states) with an invariant mass (reconstructed under the $\pi\pi$ hypothesis) larger than 5.6 GeV/c^2. The variables used in the BDT classification are identical to those used in the `B2HHBDT` stripping line, listed in Tab. 3.5, with the addition of four other variables: the minimum and the maximum between the χ^2 of the impact parameters with respect to all the primary vertices (PV) of the two final state particles, $\min(\chi^2_{IP}(h^+), \chi^2_{IP}(h'^-))$ and $\max(\chi^2_{IP}(h^+), \chi^2_{IP}(h'^-))$, the χ^2 relative to the flight distance of the b hadron, $\chi^2_{FD}(H_b)$, and the χ^2 relative to the impact parameter with respect to all the PV of the b hadron, $\chi^2_{IP}(H_b)$. We report the distributions of the variables used to train the BDT in Figs. 3.9, 3.10, and 3.11 for signal and background events. We also report in Fig. 3.12 the correlation matrices for the signal and background variables used to train the BDT.

In our analysis we train three BDTs for each set of PID cuts. This is done in order

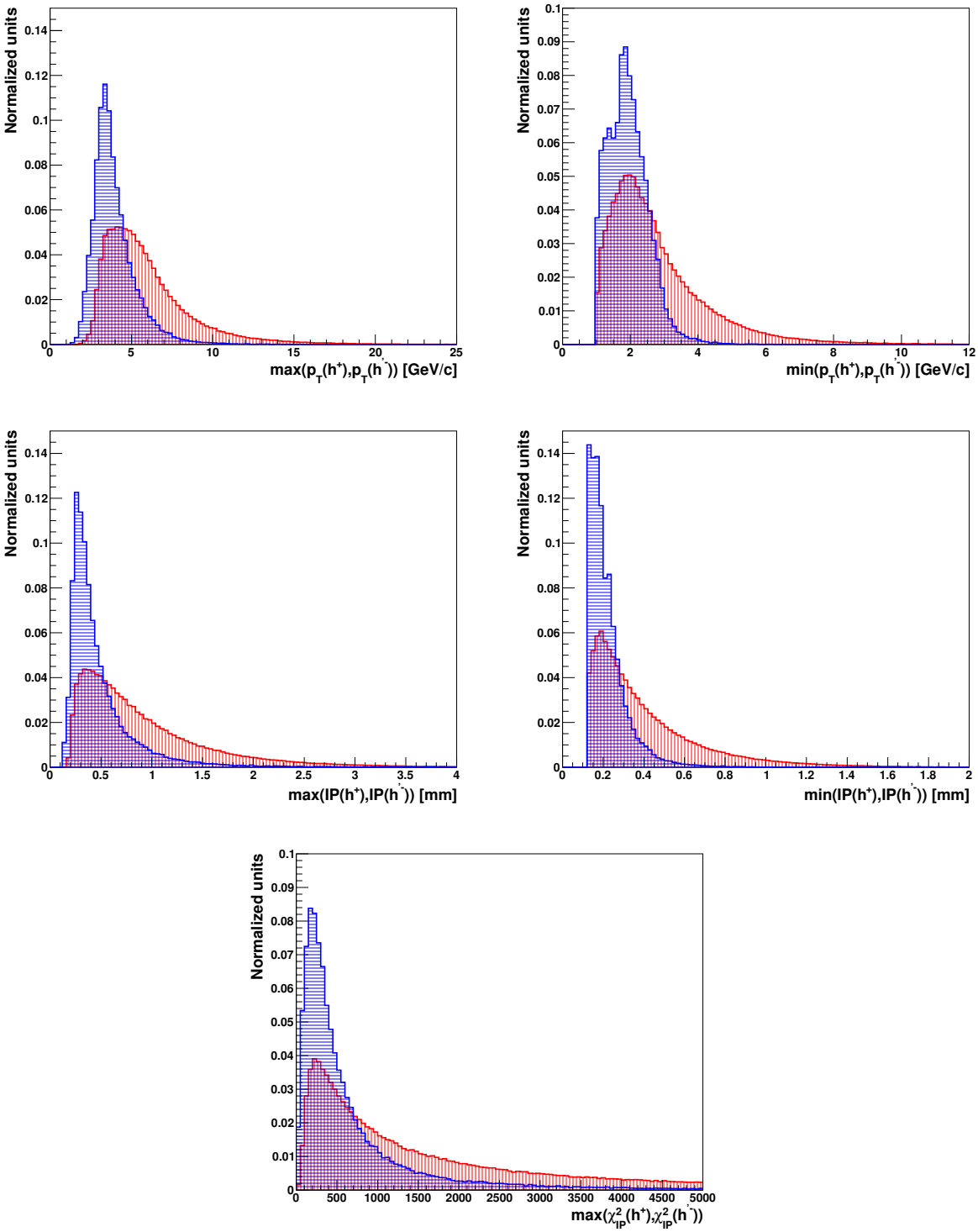

Figure 3.9: Plots showing the $\max(p_T(h^+), p_T(h'^-)$, $\min(p_T(h^+), p_T(h'^-)$, $\max(IP(h^+), IP(h'^-))$, $\min(IP(h^+), IP(h'^-))$, and $\max(\chi^2_{IP}(h^+), \chi^2_{IP}(h'^-))$ distributions for signal (red) and background (blue) events used to train the BDTs.

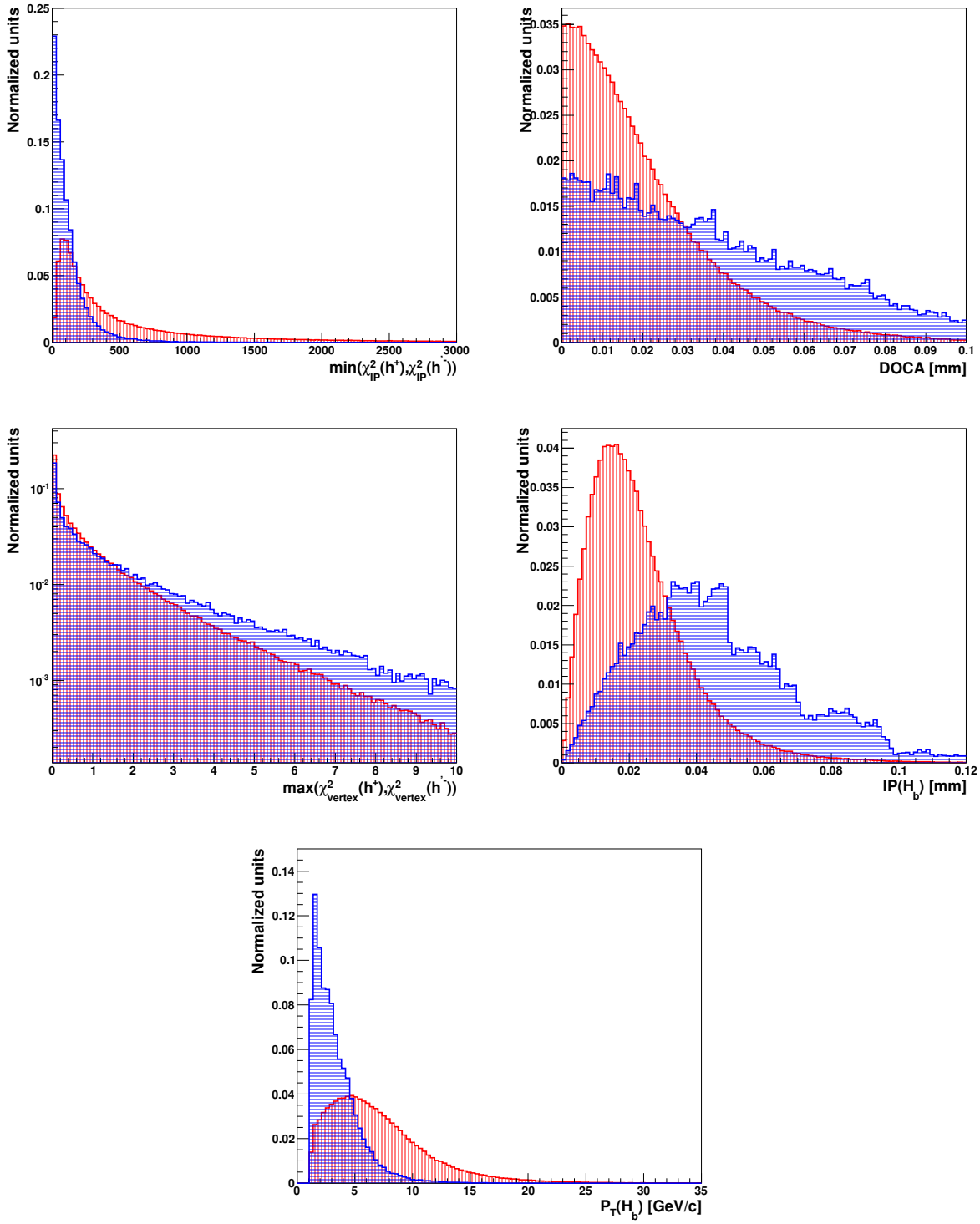

Figure 3.10: Plots showing the $\min(\chi^2_{IP}(h^+), \chi^2_{IP}(h'^-))$, DOCA, χ^2_{Vertex}, $IP(H_b)$ and $p_T(H_b)$ distributions for signal (red) and background (blue) events used to train the BDTs.

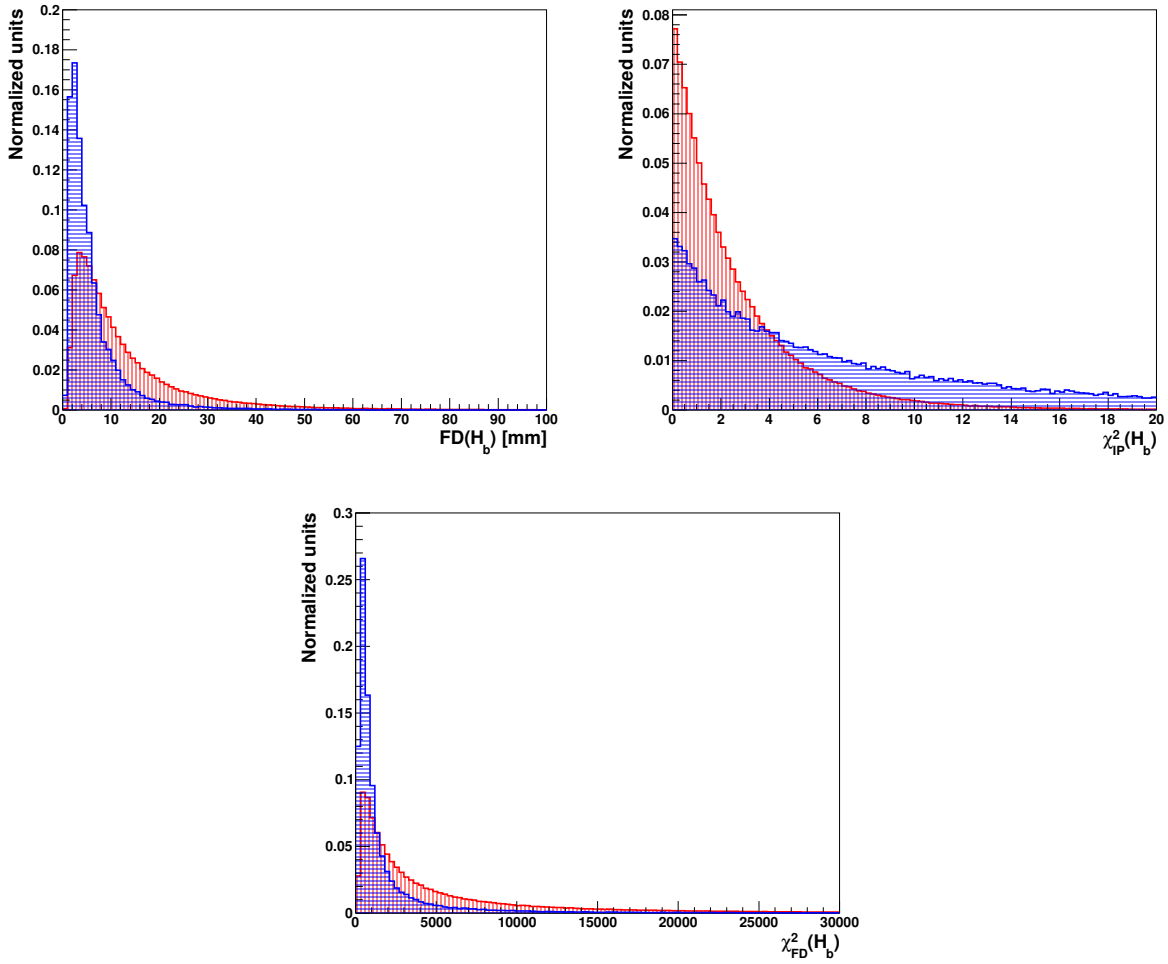

Figure 3.11: Plots showing the $FD(H_b)$, $\chi^2_{IP}(H_b)$ and $\chi^2_{FD}(H_b)$ distributions for signal (red) and background (blue) events used to train the BDTs.

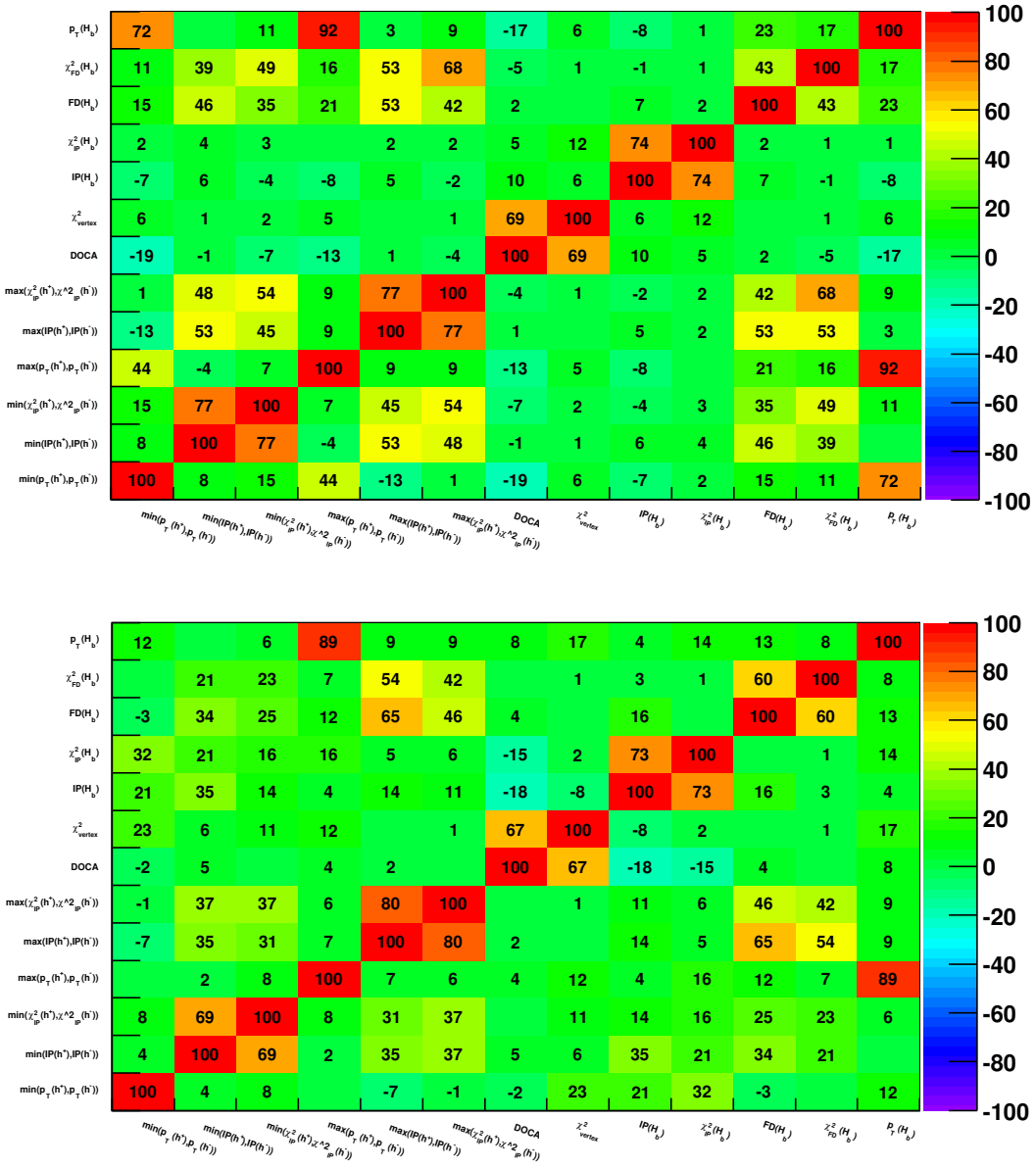

Figure 3.12: Correlation matrices of the variables used to train the BDT for signal (top) and background (bottom) events.

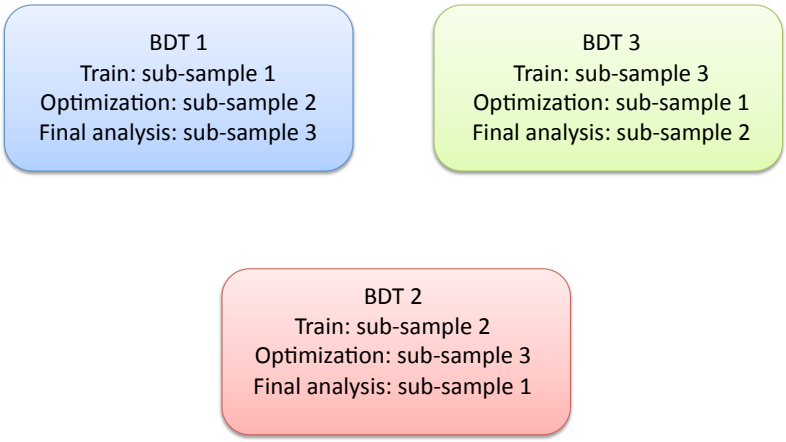

Figure 3.13: Representation of the method used to apply the BDT to the data sample.

to avoid the overtraining of the BDT and the risk of biasing the result. We randomly divide the total data sample into three different and independent sub-samples: `S1`, `S2`, and `S3`. Then we train a BDT for each sub-sample (`BDT1`, `BDT2`, and `BDT3` respectively). `BDT1` is used to select the events of `S2` in the optimization procedure while in the final analysis we will apply `BDT1` to `S3`. The same reasoning applies also to `BDT2` and `BDT3`. The approach is sketched in Fig. 3.13. We also report in Fig. 3.14 the distributions of the multivariate classificator μ_{BDT} relative to the training, optimization, and final analysis phases of the BDT, corresponding to the PID cuts found by the optimization procedure for the pK^- final state and listed in Tab. 3.11.

3.4.2 Optimization procedure

The first step of the optimization procedure consists in determining the amount of signal events, cross-feed background events, partially reconstructed background events, and combinatorial background events surviving each combination of PID and BDT requirements.

The PID cuts used to select protons for the pK^- and $p\pi^-$ final states require the $\Delta \log \mathcal{L}_{p-K}$ and $\Delta \log \mathcal{L}_{p-\pi}$ variables to be greater than a given threshold, while to choose kaons we ask $\Delta \log \mathcal{L}_{K-\pi}$ and $\Delta \log \mathcal{L}_{K-p}$ to be greater than a given threshold. We impose $\Delta \log \mathcal{L}_{K-\pi}$ and $\Delta \log \mathcal{L}_{p-\pi}$ to be smaller than a certain threshold in order to discriminate pions from kaons and protons. We report in Tabs. 3.8 and 3.9 the values for each of the $\Delta \log \mathcal{L}$ variables taken into account in the optimization procedure for the pK^- and $p\pi^-$ final states, respectively. Note that the value of the $\Delta \log \mathcal{L}_{K-p}$ and $\Delta \log \mathcal{L}_{p-\pi}$ variables used to select kaons and pions for pK^- and $p\pi^-$ final states are constrained to

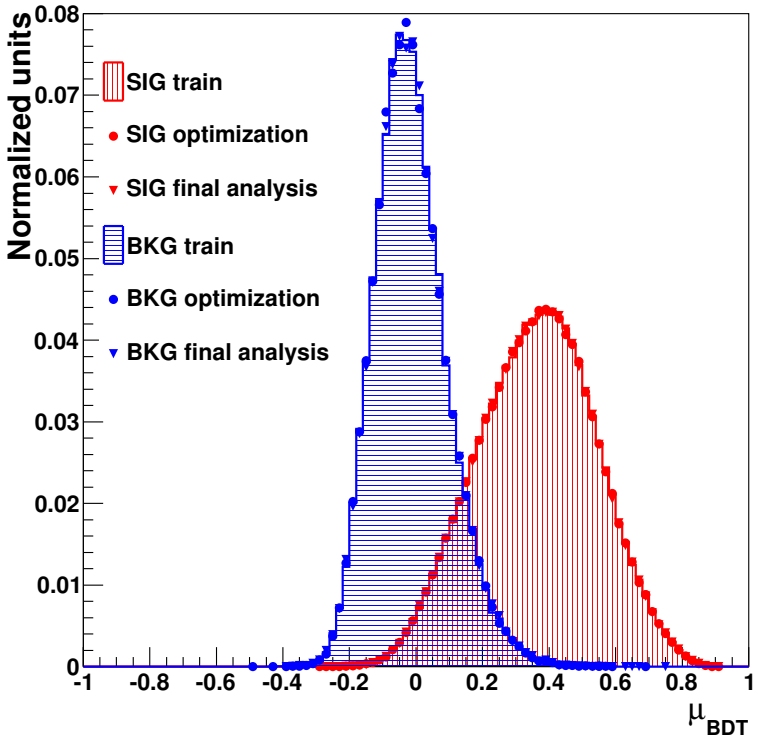

Figure 3.14: Plots showing the distributions of the multivariate classificator μ_{BDT} relative to the training (line), optimization (dot), and final analysis (triangle) phases of all the BDT, divided for signal (red) and background (blue) events. The BDT selections are those used in the analysis of the pK^- final state with the optimized cuts listed in Tab. 3.11.

be mutually exclusive with respect to the $\Delta \log \mathcal{L}_{p-\pi}$ and $\Delta \log \mathcal{L}_{p-K}$ cuts employed to select protons. This is done in order not to overlap regions between the two final states.

PID variables		Values used
$\Delta \log \mathcal{L}_{p-\pi}(p)$	$>$	5, 7, 9, 11, 13, 15
$\Delta \log \mathcal{L}_{p-K}(p)$	$>$	1, 3, 5, 7, 9, 11, 13, 15
$\Delta \log \mathcal{L}_{K-\pi}(K)$	$>$	0, 1, 3, 5, 7
$\Delta \log \mathcal{L}_{K-p}(K)$	$>$	$\max(-\Delta \log \mathcal{L}_{p-K}(p), -11) \rightarrow -1$ (step-size: 2) ; 0

Table 3.8: List of the PID cuts and respective values used in the optimization procedure for the pK^- final state.

We perform maximum likelihood fits to the selected samples in order to obtain the various

PID variables		Values used
$\Delta \log \mathcal{L}_{p-\pi}(p)$	$>$	5, 7, 9, 11, 13, 15
$\Delta \log \mathcal{L}_{p-K}(p)$	$>$	1, 3, 5, 7, 9, 11, 13, 15
$\Delta \log \mathcal{L}_{K-\pi}(\pi)$	$<$	-7, -5, -3, -1, 0
$\Delta \log \mathcal{L}_{p-\pi}(\pi)$	$<$	0 ; 1 $\to \min(\Delta \log \mathcal{L}_{p-\pi}(p), 11)$ (step-size: 2)

Table 3.9: List of the PID cuts and respective values used in the optimization procedure for the $p\pi^-$ final state.

yields and the other relevant parameters of the fitting model; note that in this step do not separate the two $\mathcal{CP}$ conjugated final states of each decay, hence not measuring any asymmetry. The model used to describe the data is the same described in Section 3.3. As an example, we report in Fig. 3.15 and Fig. 3.16 two normalization fits relative to the pK^- and $p\pi^-$ invariant mass spectra.

The numbers of signal, partially reconstructed background and combinatorial background events are left free to vary in the fit procedure.

The number of cross-feed background events is calculated in a different way. First of all, we consider only cross-feed background contributions to pK^- and $p\pi^-$ invariant mass spectra where just one final state particle is wrongly reconstructed. This is done because the amount of decays where the identity of both final state particles is wrongly assigned is negligible. Thus, the cross-feed backgrounds considered in the fit model are:

- $\bar{B}^0 \to \pi^+K^-$, $B_s^0 \to \pi^+K^-$, $B_s^0 \to K^+K^-$, and $\Lambda_b^0 \to p\pi^-$ decays for the $\Lambda_b^0 \to pK^-$ invariant mass spectrum;
- $B^0 \to K^+\pi^-$, $\bar{B}_s^0 \to K^+\pi^-$, $B^0 \to \pi^+\pi^-$, and $\Lambda_b^0 \to pK^-$ decays for $\Lambda_b^0 \to p\pi^-$ invariant mass spectrum.

We determine the number of $B^0 \to K^+\pi^-$ ($\bar{B}^0 \to \pi^+K^-$) decays directly from the fits to the pK^- ($p\pi^-$) invariant mass spectrum. The yields of other cross-feed backgrounds coming from B mesons, *i.e.* $B_s^0 \to \pi^+K^-$ and $B_s^0 \to K^+K^-$ ($\bar{B}_s^0 \to K^+\pi^-$ and $B^0 \to \pi^+\pi^-$), are constrained to the yields of the $B^0 \to K^+\pi^-$ ($\bar{B}^0 \to \pi^+K^-$), while the yields of cross-feed backgrounds coming from the other Λ_b^0 decay are constrained to the yields of the signal. The relation used is:

$$N_i = N_j \cdot \frac{\mathcal{B}(i)}{\mathcal{B}(j)} \frac{f_i}{f_j} \frac{\varepsilon_i}{\varepsilon_j} \tag{3.24}$$

where N_j represents the yields of the considered cross-feed backgrounds and N_i represents the yield of the reference decay. Note that in Eq. (3.24) $\mathcal{B}$ stands for the branching ratio, f is the hadronization fraction of the b hadron and ε is the PID efficiency of the decay under the pK^- ($p\pi^-$) hypothesis. The values of the quantities $\mathcal{B}(i)/\mathcal{B}(j) \cdot (f_i/f_j)$ are taken from a LHCb measurement [74] and are reported in Tab 3.10.

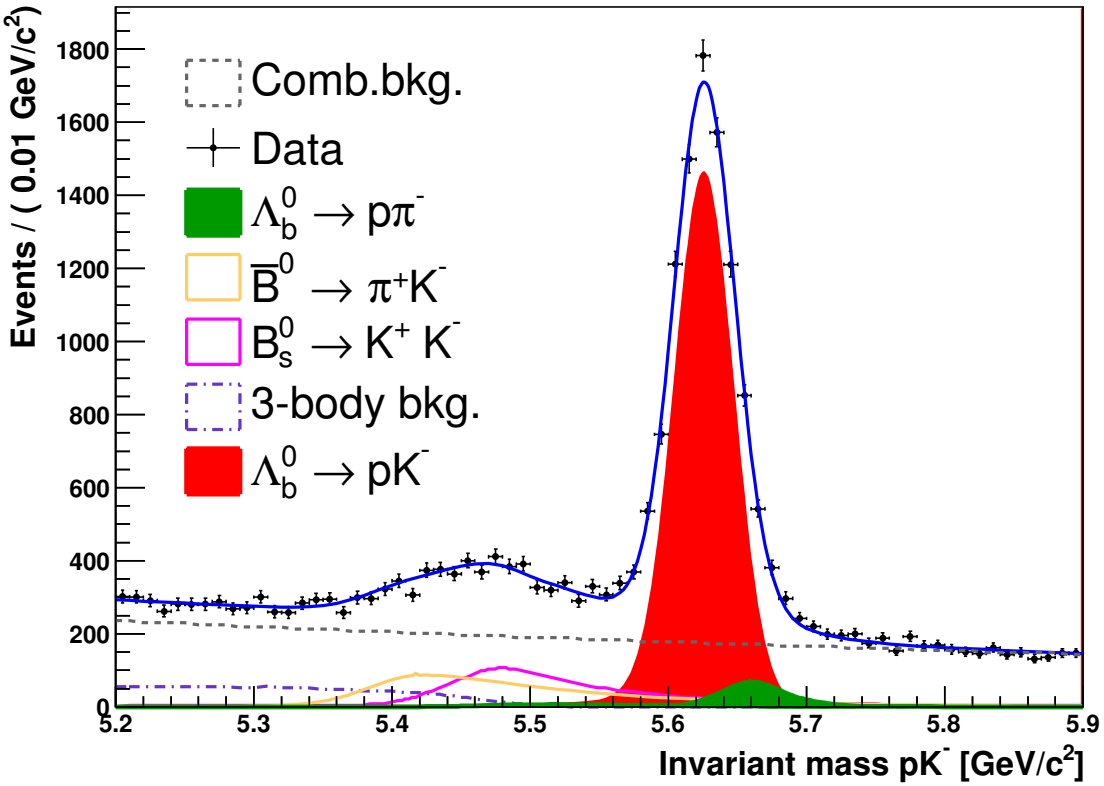

Figure 3.15: $\Lambda_b^0 \to pK^-$ invariant mass spectrum as generated using the model defined in paragraph 3.3 and selected requiring $\Delta \log \mathcal{L}_{p-\pi}(p) > 11$, $\Delta \log \mathcal{L}_{p-K}(p) > 7$, $\Delta \log \mathcal{L}_{K-\pi}(K) > 1$, and $\Delta \log \mathcal{L}_{K-p}(K) >$ -7 and BDT > 0.2. The results of the binned maximum likelihood fit are superimposed.

	Values used
$\mathcal{B}(B^0 \to \pi^+\pi^-)/\mathcal{B}(B^0 \to K^+\pi^-)$	$0.262 \pm 0.009 \pm 0.017$
$\mathcal{B}(B_s^0 \to K^+K^-)/(B^0 \to K^+\pi^-) \cdot (f_s/f_d)$	$0.316 \pm 0.009 \pm 0.019$
$\mathcal{B}(B_s^0 \to \pi^+K^-)/\mathcal{B}(B^0 \to K^+\pi^-) \cdot (f_s/f_d)$	$0.074 \pm 0.006 \pm 0.006$
$\mathcal{B}(\Lambda_b^0 \to p\pi^-)/\mathcal{B}(\Lambda_b^0 \to pK^-)$	$0.86 \pm 0.08 \pm 0.05$

Table 3.10: Values obtained in a previous LHCb measurement [74] and used in Eq. (3.24). The first uncertainties are statistic, whereas the second are systematic.

Afterwards, we perform ten pseudo-experiments for each combination of BDT and PID cuts, generating and then fitting the data using the same model and the results obtained in the previous stage. Note that in this step we introduce the asymmetry between the

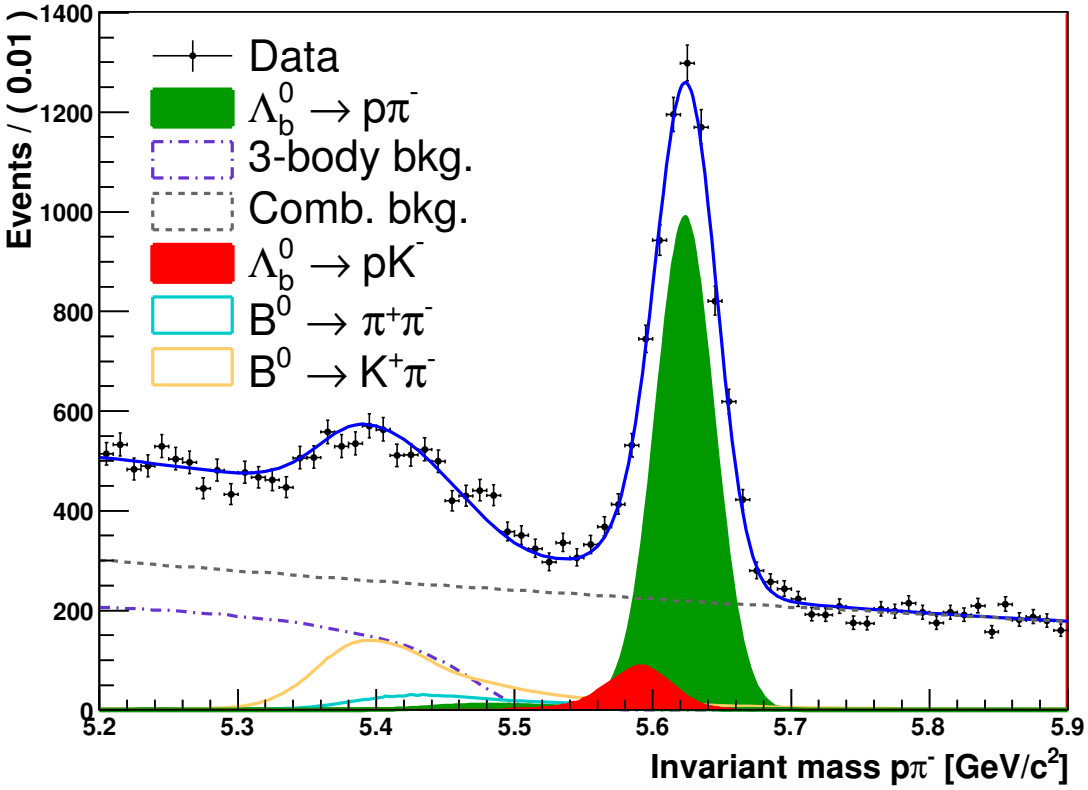

Figure 3.16: $\Lambda_b^0 \to p\pi^-$ invariant mass spectrum as generated using the model defined in paragraph 3.3 and selected requiring $\Delta \log \mathcal{L}_{p-\pi}(p) > 13$, $\Delta \log \mathcal{L}_{p-K}(p) > 7$, $\Delta \log \mathcal{L}_{K-\pi}(\pi) <$ -1, and $\Delta \log \mathcal{L}_{p-\pi}(\pi) < 7$ and BDT > 0.2. The results of the binned maximum likelihood fit are superimposed.

two $\mathcal{CP}$ conjugate modes for each component, generating the data with null asymmetries and then leaving them free to vary in the fit.

Finally we have average the ten uncertainties on each signal raw asymmetry for each set of BDT and PID cuts and we find the requirements that give the smallest average of the statistical error on the asymmetry. The values of the best PID and BDT cuts found as result of the optimization procedure for the $\Lambda_b^0 \to pK^-$ and $\Lambda_b^0 \to p\pi^-$ decays are listed in Tab. 3.11.

$\Lambda_b^0 \to pK^-$			$\Lambda_b^0 \to p\pi^-$		
Cut		Value founded	Cut		Value founded
$\Delta \log \mathcal{L}_{p-\pi}(p)$	$>$	11	$\Delta \log \mathcal{L}_{p-\pi}(p)$	$>$	11
$\Delta \log \mathcal{L}_{p-K}(p)$	$>$	7	$\Delta \log \mathcal{L}_{p-K}(p)$	$>$	7
$\Delta \log \mathcal{L}_{K-\pi}(K)$	$>$	0	$\Delta \log \mathcal{L}_{K-\pi}(\pi)$	$<$	0
$\Delta \log \mathcal{L}_{K-p}(K)$	$>$	-7	$\Delta \log \mathcal{L}_{p-\pi}(\pi)$	$<$	9
BDT	$>$	0.16	BDT	$>$	0.2

Table 3.11: Best PID and BDT cuts found by the optimization procedure for the $\Lambda_b^0 \to pK^-$ and $\Lambda_b^0 \to p\pi^-$ decays.

We also show in Fig. 3.17 a graphical representation of the predicted statistical uncertainties relative to the two raw asymmetries as a function of the PID and BDT cuts. Note that for each plot we use the values listed in Tab 3.11 for the requirements not represented, letting the plotted cut vary over the values used in the optimization procedure.

The optimized requirements for $\Delta \log \mathcal{L}_{K-\pi}(K)$ and $\Delta \log \mathcal{L}_{K-\pi}(\pi)$ are on the border of the region probed. This may hide the possibility that the requirements in Tab. 3.11 are not the optimal ones. However, one has to consider that $\Delta \log \mathcal{L}_{K-\pi}$ is the variable that allows to separate pK^- and $p\pi^-$ final states. A large contribution of $\Lambda_b^0 \to pK^-$ under the $\Lambda_b^0 \to p\pi^-$ peak (and vice versa) may lead to large systematic uncertainties. As a consequence we decide to not further loosen the cut on the $\Lambda_b^0 \to p\pi^-$ PID variable.

3.5 Final fits

We perform binned maximum likelihood fits to the mass spectra of offline selected events, with the PID and BDT cuts optimized to obtain the best statistical sensitivity on the two $\mathcal{CP}$ asymmetries. First of all we have apply the BDT requirement on the full $H_b \to h^+h'^-$ data sample.

We use the PID requirements listed in Tab. 3.11 to obtain the samples containing pK^- ($K^+\bar{p}$) and $p\pi^-$ ($\pi^+\bar{p}$) final states, whereas we use the requirements written in Tab. 3.12 to select $K^+\pi^-$ (π^+K^-), K^+K^-, and $\pi^+\pi^-$ final state hypotheses. The cuts reported in Tab. 3.12 are adopted because they were already used in previous studies, proving to perform well for our purposes [74]. Note that all the charge conjugate final states written inside parentheses are selected just swapping the requirements between the positive and the negative particles.

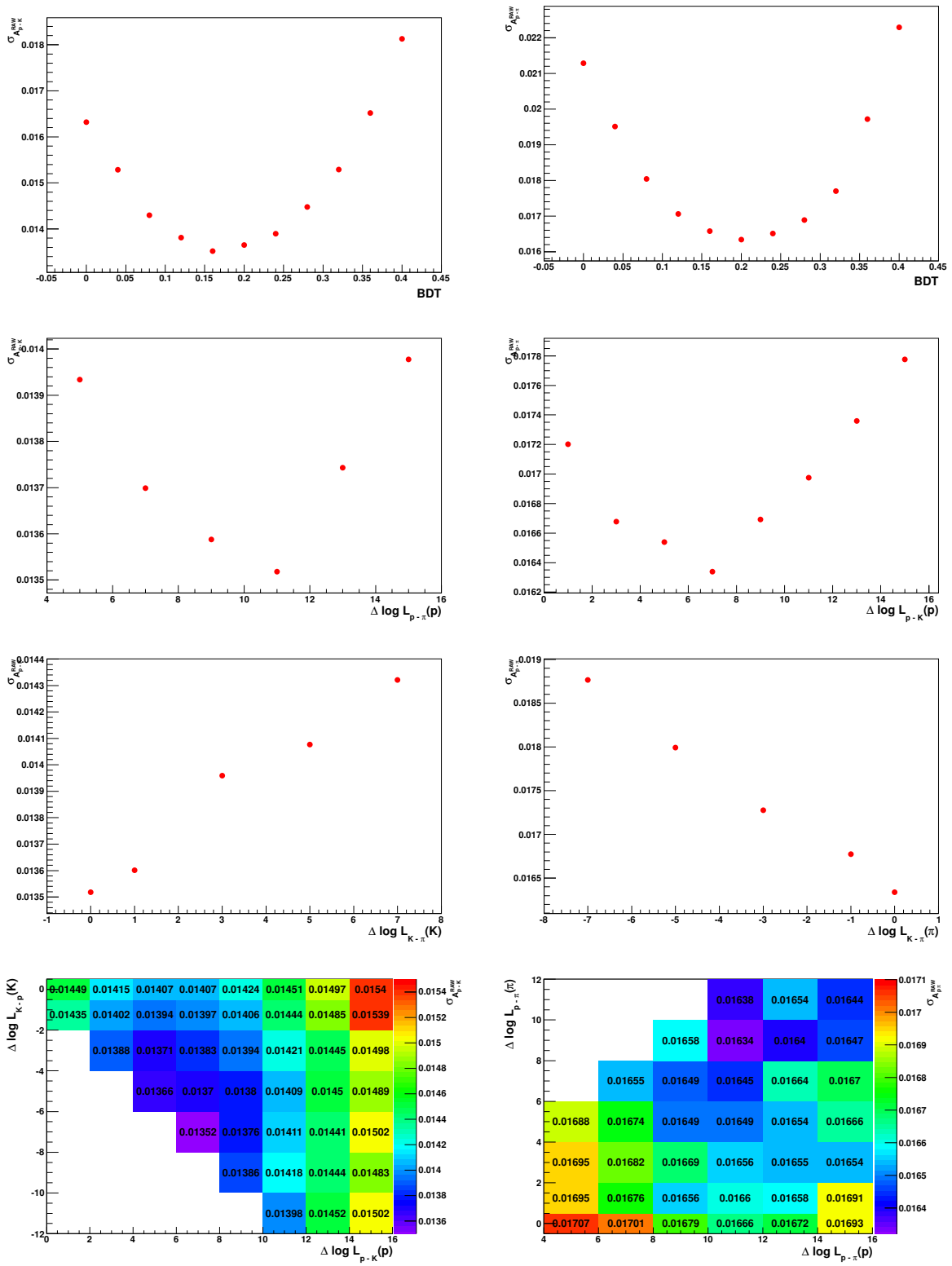

Figure 3.17: Plots showing the error on $\mathcal{A}^{RAW}(pK^-)$ (left) and $\mathcal{A}^{RAW}(p\pi^-)$ (right) as a function of the BDT and PID cuts. In every plot only the cuts vary over the respective ranges, while the other requirements (not plotted) are fixed to the values found through the optimization procedure.

$K^+\pi^-$			K^+K^-			$\pi^+\pi^-$		
Cut		Value	Cut		Value	Cut		Value
$\Delta\log\mathcal{L}_{K-\pi}(h^+)$	$>$	3	$\Delta\log\mathcal{L}_{K-\pi}(h^+)$	$>$	3	$\Delta\log\mathcal{L}_{K-\pi}(h^+)$	$<$	-3
$\Delta\log\mathcal{L}_{K-p}(h^+)$	$>$	-5	$\Delta\log\mathcal{L}_{K-p}(h^+)$	$>$	-5	$\Delta\log\mathcal{L}_{p-\pi}(h^+)$	$<$	5
$\Delta\log\mathcal{L}_{K-\pi}(h'^-)$	$<$	-3	$\Delta\log\mathcal{L}_{K-\pi}(h'^-)$	$>$	3	$\Delta\log\mathcal{L}_{K-\pi}(h'^-)$	$<$	-3
$\Delta\log\mathcal{L}_{p-\pi}(h'^-)$	$<$	5	$\Delta\log\mathcal{L}_{K-p}(h'^-)$	$>$	-5	$\Delta\log\mathcal{L}_{p-\pi}(h'^-)$	$<$	5

Table 3.12: PID cuts applied for the identification of the $K^+\pi^-$, K^+K^-, and $\pi^+\pi^-$ mass hypotheses. Note that to obtain the charge conjugate final states, h^+ and h'^- must be exchanged.

The fit model used for the analysis is composed of the signal model defined in paragraph 3.3.1, the cross-feed background model, obtained as described in paragraph 3.3.2, the 3-body partially reconstructed background parametrization given by Eq. (3.22), and the combinatorial background model described in paragraph 3.3.4.

Raw asymmetries are extracted directly from the fit using the following parameterization:

$$N_i = \frac{N_i^{tot}}{2} \cdot (1 + \mathcal{A}_i^{RAW}) \ , \tag{3.25}$$

$$\bar{N}_i = \frac{N_i^{tot}}{2} \cdot (1 - \mathcal{A}_i^{RAW}) \ , \tag{3.26}$$

where N_i ($\bar{N}_i$) are the yields of the two charge-conjugate states of the i-th component contributing to the invariant mass spectra, $\mathcal{A}_i^{RAW}$ is the raw asymmetry of the i-th component and N_i^{tot} is the total yield of the i-th component.

The normalization of each cross-feed background is determined as the product of the yields of the correctly identified channel with the ratio of the PID efficiencies relative to the wrong and correct final state hypotheses. As an example, the number of $B^0 \to \pi^+\pi^-$ events giving a cross-feed background contribution to the $K^+\pi^-$ mass spectrum is given by:

$$N(\pi^+\pi^- \to K^+\pi^-) = Y(B^0 \to \pi^+\pi^-)\frac{\varepsilon^{B^0\to\pi^+\pi^-}_{K^+\pi^-}}{\varepsilon^{B^0\to\pi^+\pi^-}_{\pi^+\pi^-}} \tag{3.27}$$

where $N(\pi^+\pi^- \to K^+\pi^-)$ is the number of $\pi^+\pi^-$ final states wrongly identified as $K^+\pi^-$ final states, $Y(B^0 \to \pi^+\pi^-)$ represents the number of $B^0 \to \pi^+\pi^-$ decays as obtained from the fit, and $\varepsilon^{B^0\to\pi^+\pi^-}_{K^+\pi^-}$ ($\varepsilon^{B^0\to\pi^+\pi^-}_{\pi^+\pi^-}$) is the PID efficiency of the $B^0 \to \pi^+\pi^-$ decay under the $K^+\pi^-$ ($\pi^+\pi^-$) hypothesis. We report in Tabs. 3.13 and 3.14 the value of the PID efficiencies obtained from the calibration procedure described in Section 3.2 using the PID and BDT cuts found for the pK^- and $p\pi^-$ final states by the optimization procedure.

Decay	Final state hypothesis							
	$\pi^+\pi^-$	K^+K^-	$K^+\pi^-$	π^+K^-	pK^-	$K^+\bar{p}$	$p\pi^-$	$\pi^+\bar{p}$
$B^0 \to K^+\pi^-$	1.579	2.985	52.742	0.091	0.183	0.809	0.401	0.019
$B_s^0 \to K^+\pi^-$	1.579	2.985	52.742	0.091	0.183	0.809	0.401	0.019
$B^0 \to \pi^+K^-$	1.587	2.989	0.091	52.682	0.802	0.187	0.019	0.405
$B_s^0 \to \pi^+K^-$	1.587	2.989	0.091	52.682	0.802	0.187	0.019	0.405
$B^0 \to \pi^+\pi^-$	49.181	0.162	2.784	2.778	0.114	0.116	0.605	0.608
$B_s^0 \to \pi^+\pi^-$	49.181	0.162	2.784	2.778	0.114	0.116	0.605	0.608
$B^0 \to K^+K^-$	0.051	56.510	1.703	1.694	1.150	1.167	0.014	0.014
$B_s^0 \to K^+K^-$	0.051	56.510	1.703	1.694	1.150	1.167	0.014	0.014
$\Lambda_b^0 \to pK^-$	0.019	7.476	0.258	0.554	61.840	0.346	1.330	0.006
$\Lambda_b^0 \to K^+\bar{p}$	0.015	7.528	0.564	0.264	0.307	61.918	0.003	1.321
$\Lambda_b^0 \to p\pi^-$	0.519	0.409	6.985	0.028	9.450	0.297	44.716	0.004
$\Lambda_b^0 \to \pi^+\bar{p}$	0.538	0.428	0.039	7.120	0.212	9.352	0.004	44.762

Table 3.13: PID efficiencies (in %) of the various mass hypotheses obtained using the optimized PID cuts for the pK^- final state selection.

Decay	Final state hypothesis							
	$\pi^+\pi^-$	K^+K^-	$K^+\pi^-$	π^+K^-	pK^-	$K^+\bar{p}$	$p\pi^-$	$\pi^+\bar{p}$
$B^0 \to K^+\pi^-$	1.587	2.972	51.526	0.092	0.023	0.617	1.059	0.078
$B_s^0 \to K^+\pi^-$	1.587	2.972	51.526	0.092	0.023	0.617	1.059	0.078
$B^0 \to \pi^+K^-$	1.606	2.964	0.093	51.469	0.615	0.023	0.078	1.071
$B_s^0 \to \pi^+K^-$	1.606	2.964	0.093	51.469	0.615	0.023	0.078	1.071
$B^0 \to \pi^+\pi^-$	48.069	0.163	2.761	2.766	0.032	0.116	0.737	0.740
$B_s^0 \to \pi^+\pi^-$	48.069	0.163	2.761	2.766	0.032	0.032	0.737	0.740
$B^0 \to K^+K^-$	0.053	55.185	1.723	1.702	0.414	0.419	0.126	0.127
$B_s^0 \to K^+K^-$	0.053	55.185	1.723	1.702	0.414	0.419	0.126	0.127
$\Lambda_b^0 \to pK^-$	0.019	7.068	0.258	0.524	47.079	0.054	6.353	0.084
$\Lambda_b^0 \to K^+\bar{p}$	0.015	7.077	0.533	0.261	0.050	47.338	0.049	6.339
$\Lambda_b^0 \to p\pi^-$	0.492	0.405	6.598	0.027	2.517	0.088	58.487	0.050
$\Lambda_b^0 \to \pi^+\bar{p}$	0.510	0.420	0.038	6.695	0.080	2.438	0.026	58.695

Table 3.14: PID efficiencies (in %) of the various mass hypotheses obtained using the optimized PID cuts for the $p\pi^-$ final state selection.

To properly take into account the possible cross-feed contributions to all invariant mass spectra, we perform a joint fit of the eight categories at once. In this way we determine simultaneously all signal yields and normalizations of the backgrounds.

The binned maximum likelihood fit features 58 free parameters:

- four raw $\mathcal{CP}$ asymmetries $\mathcal{A}_{sig}^{RAW}$ for the signal: $\mathcal{A}_{sig}^{RAW}(B^0 \to K^+\pi^-)$, $\mathcal{A}_{sig}^{RAW}(B_s^0 \to K^+\pi^-)$, $\mathcal{A}_{sig}^{RAW}(\Lambda_b^0 \to pK^-)$ and $\mathcal{A}_{sig}^{RAW}(\Lambda_b^0 \to p\pi^-)$;

- three raw $\mathcal{CP}$ asymmetries for the combinatorial backgrounds relative to the $K^+\pi^-$, pK^-, and $p\pi^-$ final states;

- four raw $\mathcal{CP}$ asymmetries for the 3-body partially reconstructed background components considered in the $K^+\pi^-$, pK^-, and $p\pi^-$ spectra;

- eight signal yields: $N^{Tot}(B^0 \to K^+\pi^-)$, $N^{Tot}(B_s^0 \to K^+\pi^-)$, $N^{Tot}(B^0 \to \pi^+\pi^-)$, $N^{Tot}(B_s^0 \to \pi^+\pi^-)$, $N^{Tot}(B^0 \to K^+K^-)$, $N^{Tot}(B_s^0 \to K^+K^-)$, $N^{Tot}(\Lambda_b^0 \to pK^-)$ and $N^{Tot}(\Lambda_b^0 \to p\pi^-)$;

- five combinatorial background yields relative to the $K^+\pi^-$, K^+K^-, $\pi^+\pi^-$, pK^-, and $p\pi^-$ final states;

- six 3-body partially reconstructed background yields, relative to the components contributing to the $K^+\pi^-$, $\pi^+\pi^-$, K^+K^-, pK^-, and $p\pi^-$; the number of parameters results to be greater than the number of final states since in the $K^+\pi^-$ spectra two source of partially reconstructed background have been considered, one from decays of B^0 mesons and one from the decays of B_s^0 mesons;

- five parameters of the ARGUS p.d.f. that models the 3-body partially reconstructed background relative to $K^+\pi^-$, $\pi^+\pi^-$, K^+K^-, pK^-, and $p\pi^-$ spectra;

- five fractions governing the proportion between the Gaussian functions composing the invariant mass resolution model in the $K^+\pi^-$, $\pi^+\pi^-$, K^+K^-, pK^-, and $p\pi^-$ spectra.

- three mean values of the reconstructed invariant mass for the B^0, B_s^0 and Λ_b^0 hadrons;

- ten standard deviations relative to the Gaussian functions composing the invariant mass resolution model in the $K^+\pi^-$, $\pi^+\pi^-$, K^+K^-, pK^-, and $p\pi^-$ spectra respectively;

- five exponential slopes for the combinatorial backgrounds relative to the $K^+\pi^-$, $\pi^+\pi^-$, K^+K^-, pK^-, and $p\pi^-$ final states.

The fits are realized using the MIGRAD minimization engine of the MINUIT software library [75], configured with the so-called *Strategy 2*, followed upon convergence by the HESSE algorithm of the same library, in order to calculate with better precision the covariance matrix. Two binned maximum likelihood fits are done, either using the selection optimized to obtain the best statistical sensitivity on $\mathcal{A}_{\mathcal{CP}}(pK^-)$ or on $\mathcal{A}_{\mathcal{CP}}(p\pi^-)$.

3.5.1 Selection optimized for $\mathcal{A}_{\mathcal{CP}}(\Lambda_b^0 \to pK^-)$

The relevant parameters determined by the maximum likelihood fit are summarized in Tab. 3.15.

Parameter	Fit Result
$B^0 \to K^+\pi^-$ yield	121019 ± 427
$B_s^0 \to \pi^+K^-$ yield	9337 ± 162
$B^0 \to \pi^+\pi^-$ yield	30980 ± 485
$B_s^0 \to \pi^+\pi^-$ yield	873 ± 98
$B^0 \to K^+K^-$ yield	874 ± 94
$B_s^0 \to K^+K^-$ yield	42908 ± 270
$\Lambda_b^0 \to pK^-$ yield	8666 ± 192
$\Lambda_b^0 \to p\pi^-$ yield	5274 ± 122
B^0 mass [GeV/c^2]	5.28540 ± 0.00007
B_s^0 mass [GeV/c^2]	5.37290 ± 0.00012
Λ_b^0 mass [GeV/c^2]	5.62510 ± 0.00027
$\mathcal{A}^{RAW}(pK^-)$	0.018 ± 0.013

Table 3.15: Relevant parameters determined by the binned maximum likelihood fit to the data sample surviving the event selection optimized for the best sensitivity on $\mathcal{A}_{\mathcal{CP}}(\Lambda_b^0 \to pK^-)$. Only statistical uncertainties are shown.

We also show in Figs. 3.18, 3.19, 3.20, 3.21 all the invariant mass spectra for candidates surviving the event selection optimized for the best sensitivity on $\mathcal{A}_{\mathcal{CP}}(\Lambda_b^0 \to pK^-)$, with the results of the binned maximum likelihood fit superimposed. Note that the cross-feed contributions to all invariant mass spectra are considered in the fit procedure, but only those with greater yields are visible in the plots.

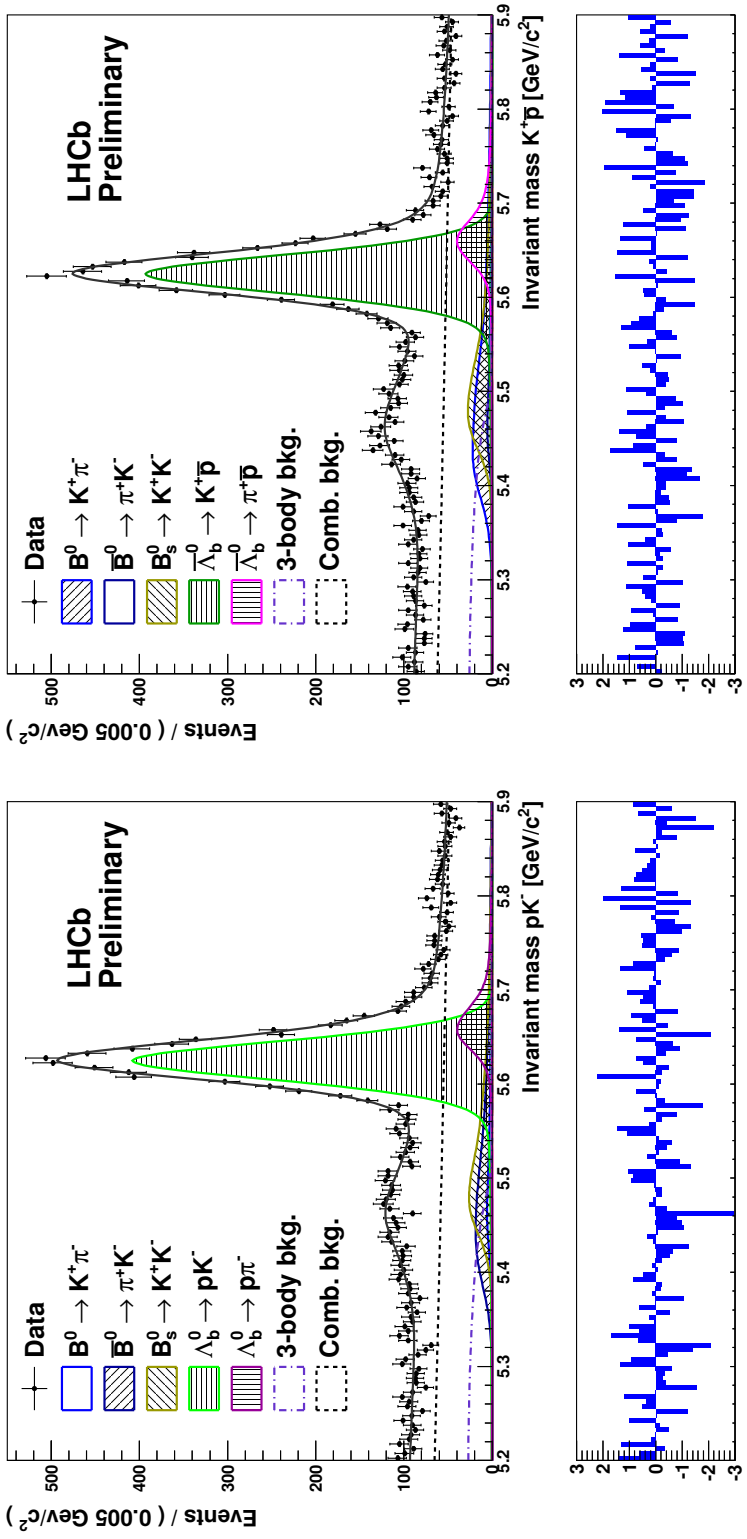

Figure 3.18: pK^- (left) and $K^+\bar{p}$ (right) invariant mass spectra for events surviving the selection optimized to obtain the best sensitivity on $\mathcal{A}_{CP}(\Lambda_b^0 \to pK^-)$. The result of the binned maximum likelihood fit is superimposed to the histogram. The various signal and background components contributing to the fit model are also shown.

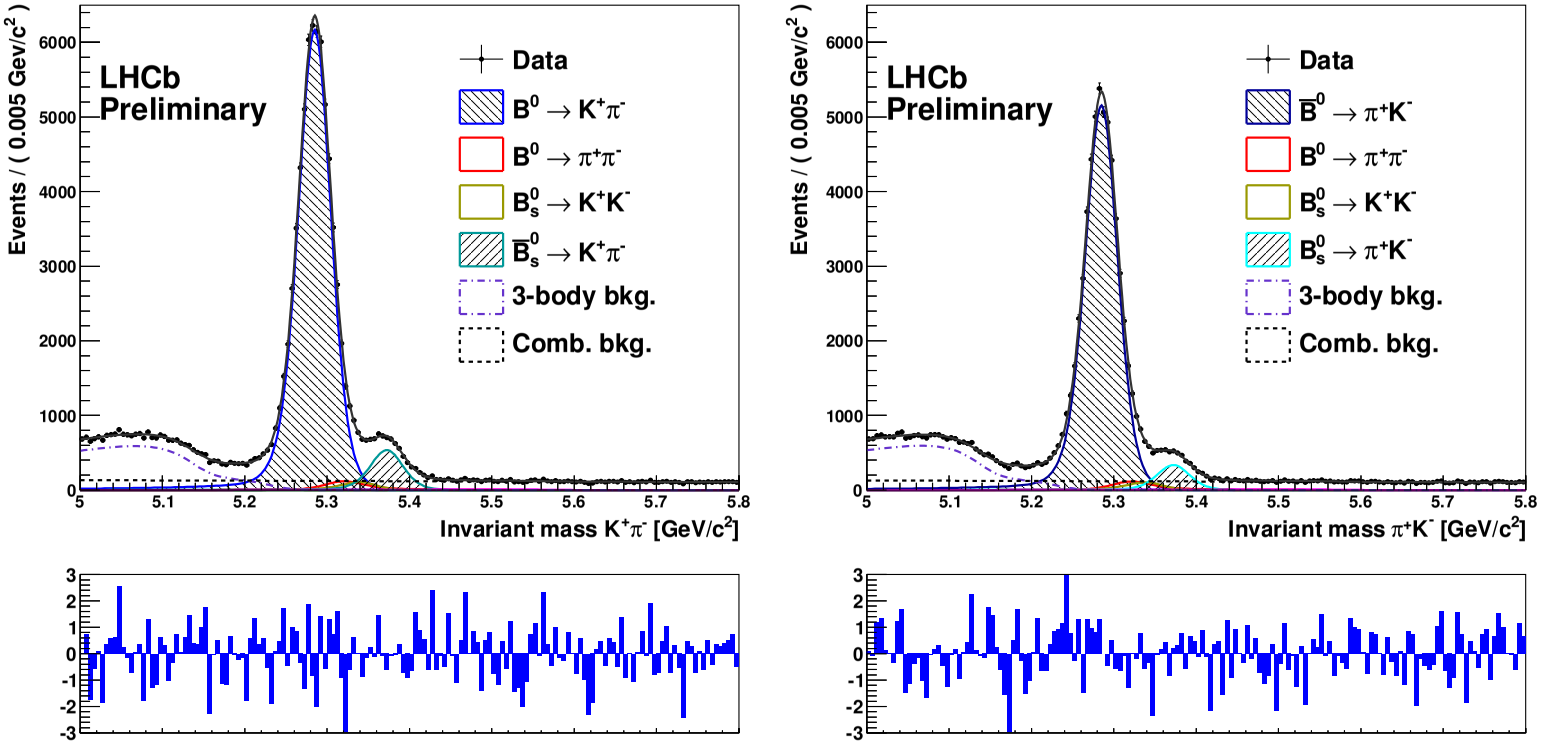

Figure 3.19: $K^+\pi^-$ (left) and π^+K^- (right) invariant mass spectra for events surviving the selection optimized to obtain the best sensitivity on $\mathcal{A}_{CP}(\Lambda_b^0 \to pK^-)$. The result of the binned maximum likelihood fit is superimposed to the histogram. The various signal and background components contributing to the fit model are also shown.

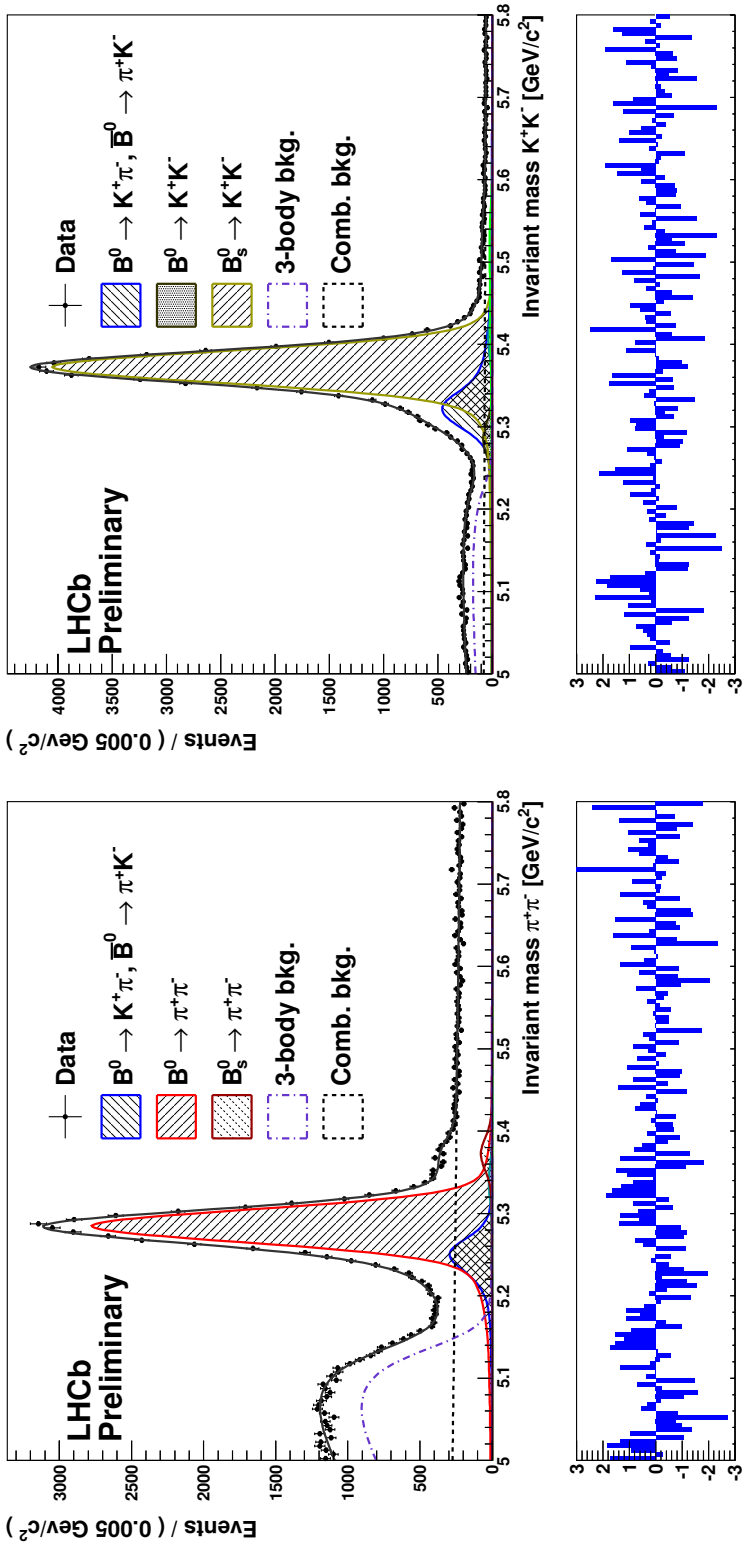

Figure 3.20: $\pi^+\pi^-$ (left) and K^+K^- (right) invariant mass spectra for events surviving the selection optimized to obtain the best sensitivity on $\mathcal{A}_{CP}(\Lambda_b^0 \to pK^-)$. The result of the binned maximum likelihood fit is superimposed to the histogram. The various signal and background components contributing to the fit model are also shown.

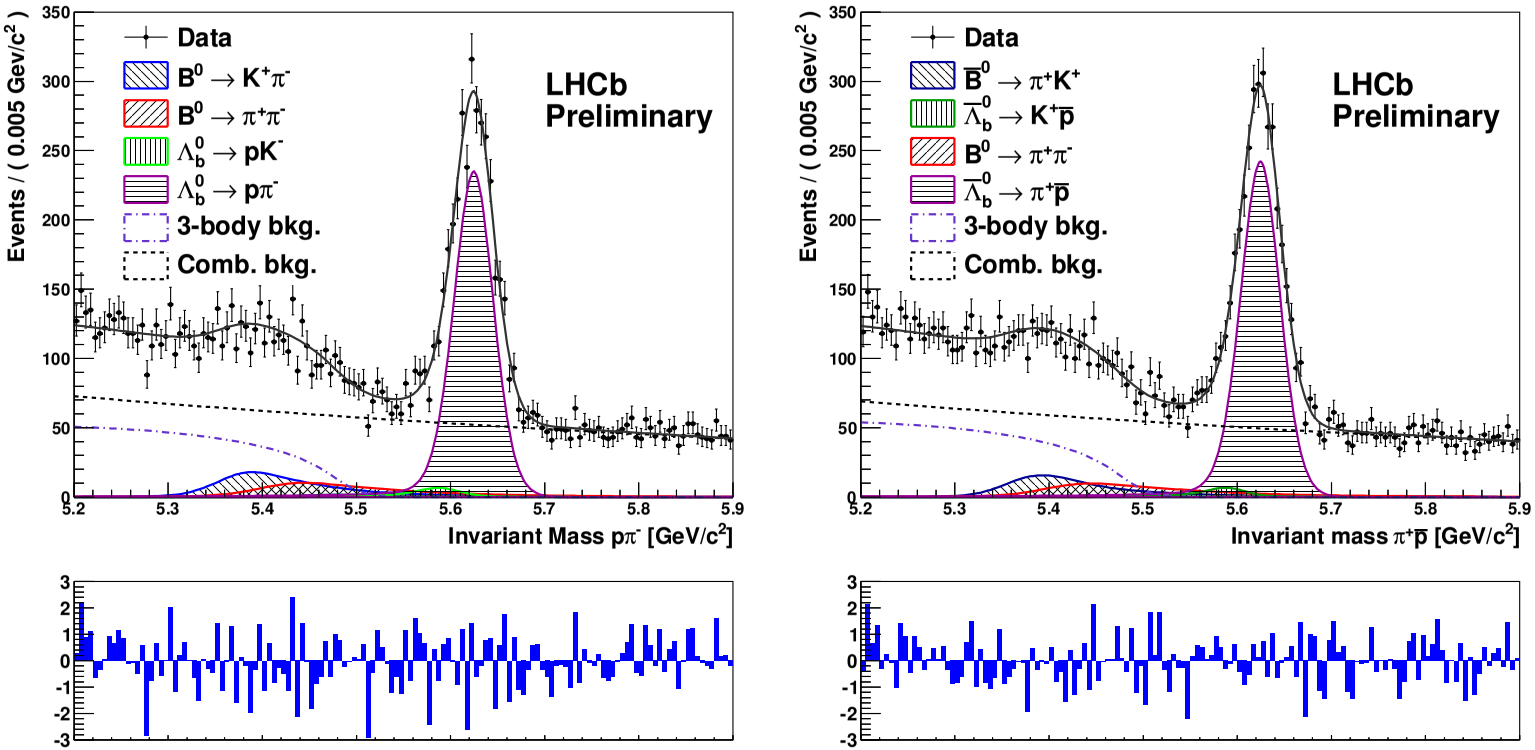

Figure 3.21: $p\pi^-$ (left) and $\pi^+\bar{p}$ (right) invariant mass spectra for events surviving the selection optimized to obtain the best sensitivity on $\mathcal{A}_{CP}(\Lambda_b^0 \to pK^-)$. The result of the binned maximum likelihood fit is superimposed to the histogram. The various signal and background components contributing to the fit model are also shown.

3.5.2 Selection optimized for $\mathcal{A}_{\mathcal{CP}}(\Lambda_b^0 \to p\pi^-)$

The relevant parameters determined by the maximum likelihood fit are summarized in Tab. 3.16.

Parameter	Fit Result
$B^0 \to K^+\pi^-$ yield	108555 ± 383
$B_s^0 \to \pi^+K^-$ yield	8217 ± 139
$B^0 \to \pi^+\pi^-$ yield	27899 ± 314
$B_s^0 \to \pi^+\pi^-$ yield	732 ± 73
$B^0 \to K^+K^-$ yield	865 ± 81
$B_s^0 \to K^+K^-$ yield	38226 ± 254
$\Lambda_b^0 \to pK^-$ yield	6386 ± 111
$\Lambda_b^0 \to p\pi^-$ yield	5972 ± 155
B^0 mass [GeV/c^2]	5.28540 ± 0.00007
B_s^0 mass [GeV/c^2]	5.37290 ± 0.00003
Λ_b^0 mass [GeV/c^2]	5.6255 ± 0.0027
$\mathcal{A}^{RAW}(p\pi^-)$	-0.002 ± 0.016

Table 3.16: Relevant parameters determined by the binned maximum likelihood fit to the data sample surviving the event selection optimized for the best sensitivity on $\mathcal{A}_{\mathcal{CP}}(\Lambda_b^0 \to p\pi^-)$. Only statistical uncertainties are shown.

We also show in Figs. 3.22, 3.23, 3.24, 3.25 the invariant mass spectra for candidates surviving the event selection optimized for the best sensitivity on $\mathcal{A}_{\mathcal{CP}}(\Lambda_b^0 \to p\pi^-)$, with the results of the binned maximum likelihood fit superimposed. Note again that the cross-feed contributions to all invariant mass spectra are considered in the fit procedure, but only those with greater yields are visible in the plots.

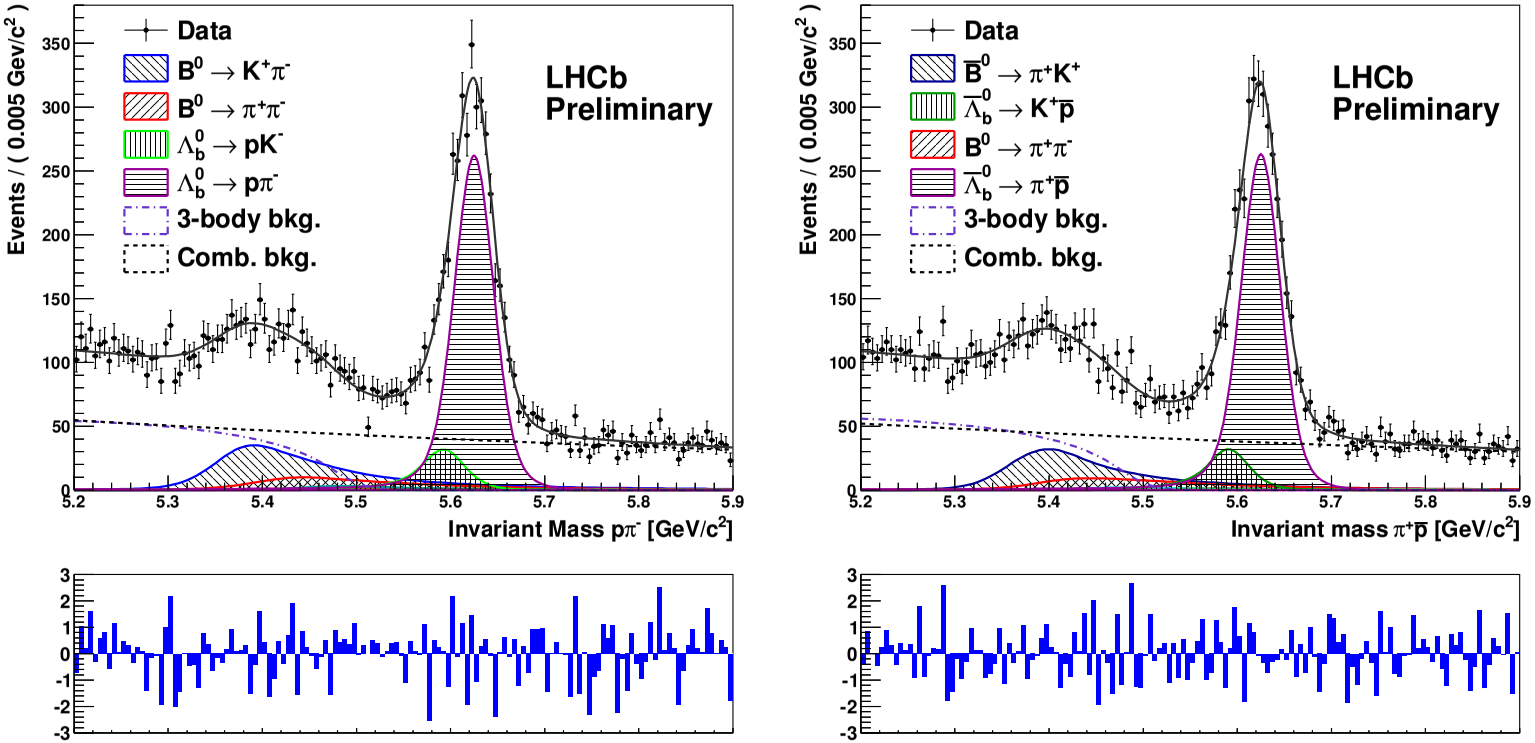

Figure 3.22: $p\pi^-$ (left) and $\pi^+\bar{p}$ (right) invariant mass spectra for events surviving the selection optimized to obtain the best sensitivity on $\mathcal{A}_{CP}(\Lambda_b^0 \to p\pi^-)$. The result of the binned maximum likelihood fit is superimposed to the histogram. The various signal and background components contributing to the fit model are also shown.

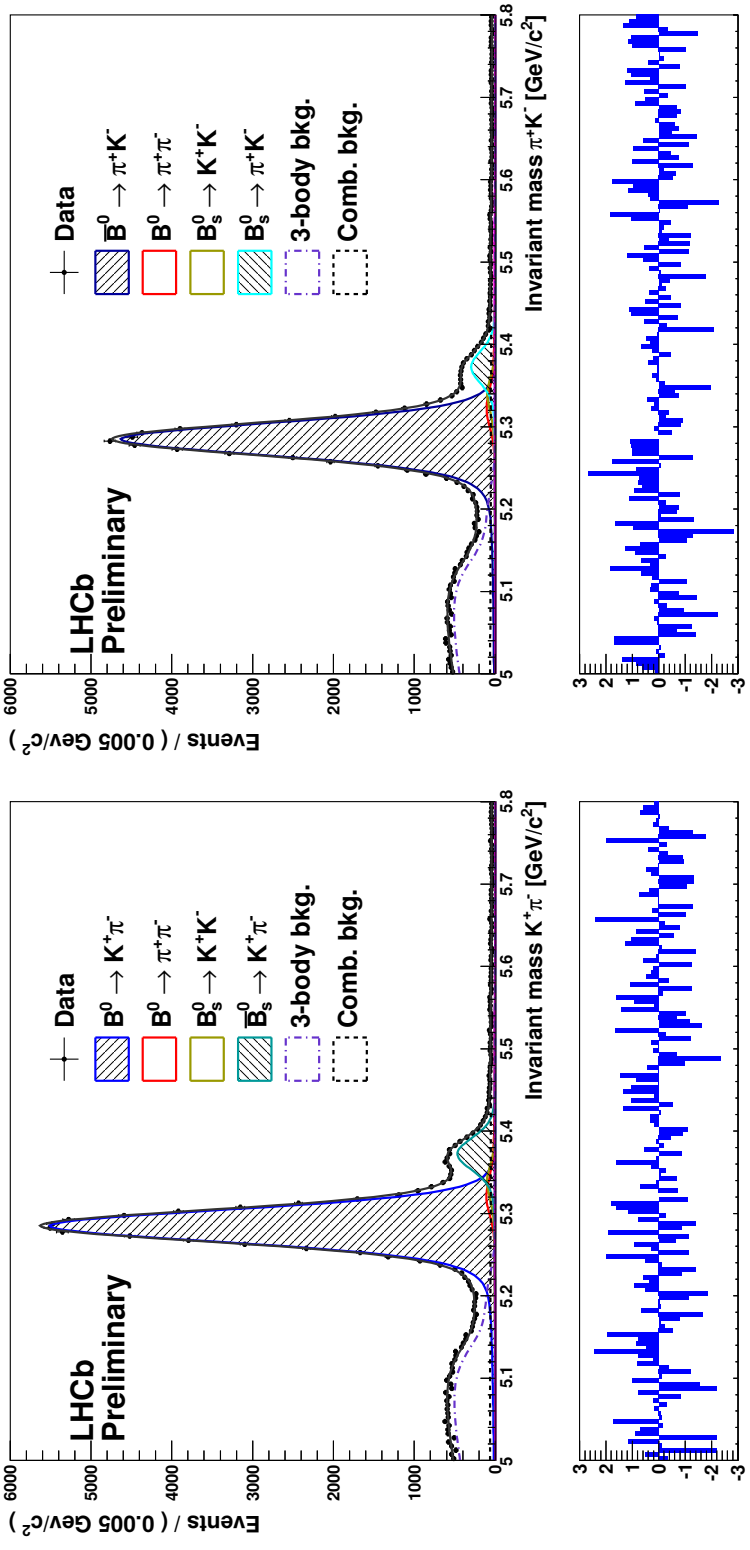

Figure 3.23: $K^+\pi^-$ (left) and π^+K^- (right) invariant mass spectra for events surviving the selection optimized to obtain the best sensitivity on $\mathcal{A}_{CP}(\Lambda_b^0 \to p\pi^-)$. The result of the binned maximum likelihood fit is superimposed to the histogram. The various signal and background components contributing to the fit model are also shown.

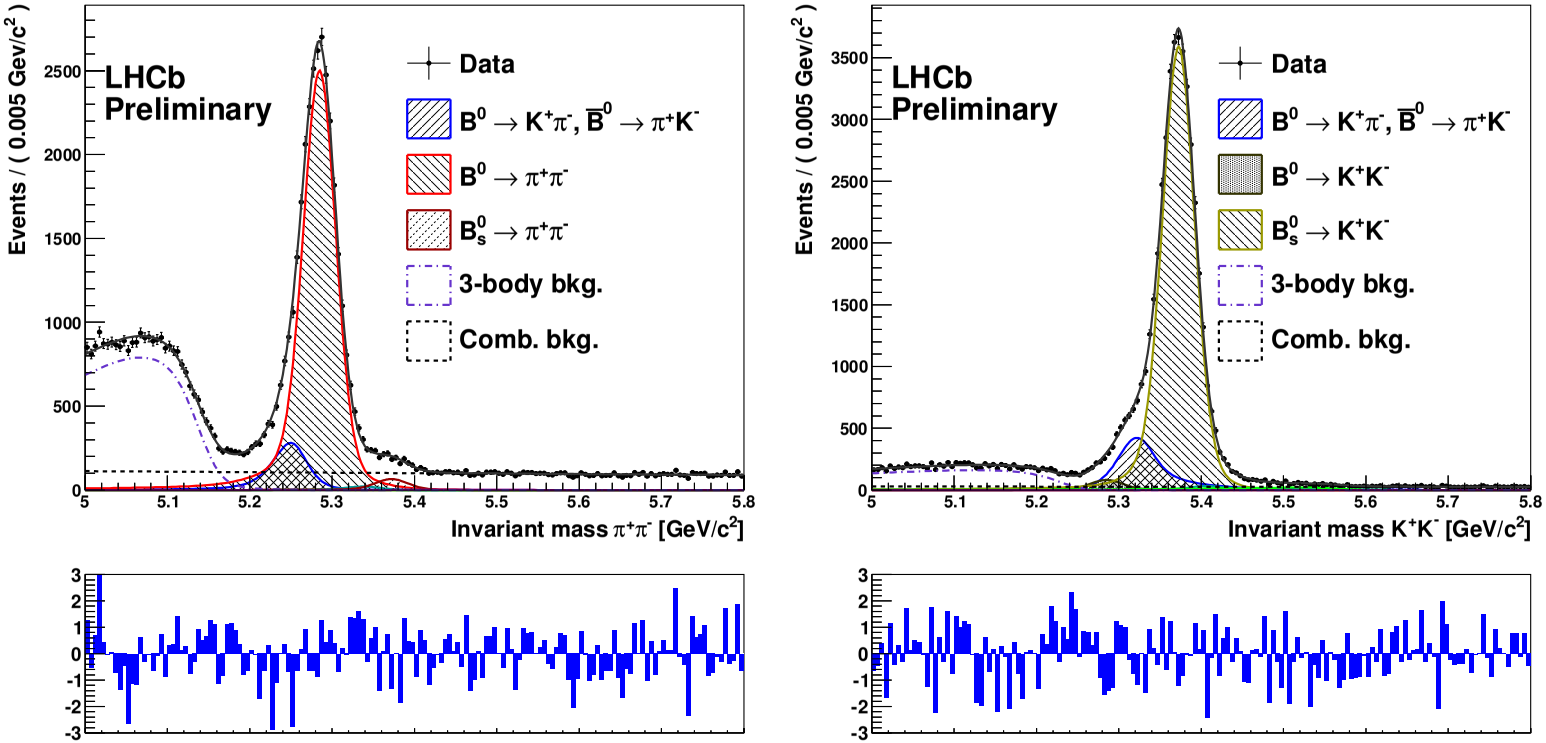

Figure 3.24: $\pi^+\pi^-$ (left) and K^+K^- (right) invariant mass spectra for events surviving the selection optimized to obtain the best sensitivity on $\mathcal{A}_{\mathcal{CP}}(\Lambda_b^0 \to p\pi^-)$. The result of the binned maximum likelihood fit is superimposed to the histogram. The various signal and background components contributing to the fit model are also shown.

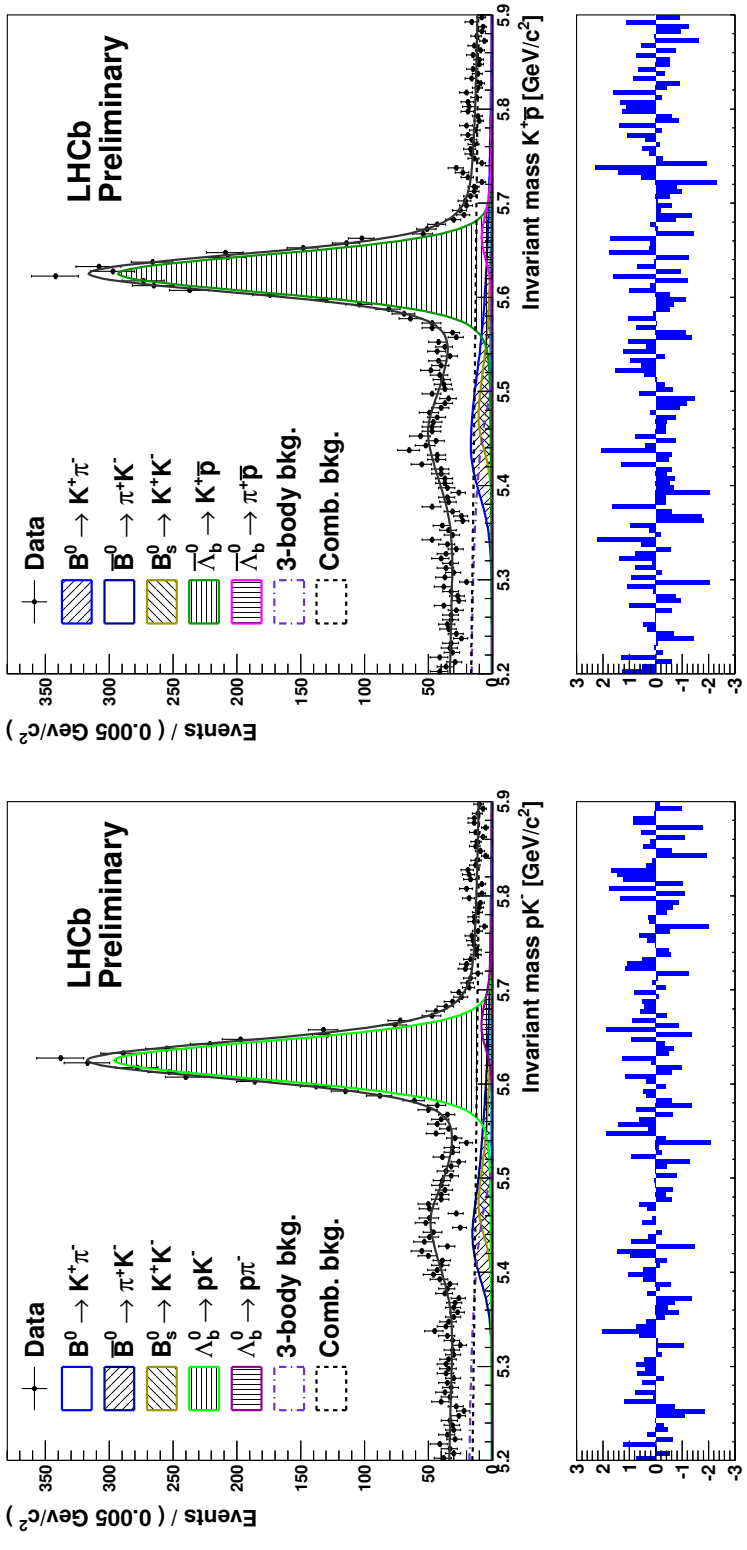

Figure 3.25: pK^- (left) and $K^+\bar{p}$ (right) invariant mass spectra for events surviving the selection optimized to obtain the best sensitivity on $\mathcal{A}_{CP}(\Lambda_b^0 \to p\pi^-)$. The result of the binned maximum likelihood fit is superimposed to the histogram. The various signal and background components contributing to the fit model are also shown.

3.6 Corrections

The quantities we extracted from fit are not the physical $\mathcal{CP}$ asymmetries that we want to measure. However, they can be related to the physical asymmetries, as shown in the following.

The definition of raw asymmetry for a particular decay is:

$$\mathcal{A}^{RAW}(f) = \frac{N(f) - \bar{N}(\bar{f})}{N(f) + \bar{N}(\bar{f})} \tag{3.28}$$

where N ($\bar{N}$) represent the number of baryons (anti-baryons) decayed to a final state f ($\bar{f}$). We can now write the number of Λ_b^0 ($\bar{\Lambda}_b^0$) decaying to a final state $f = pK^-$ ($\bar{f} = K^+\bar{p}$) as:

$$N \propto \int_{\Omega_{\Lambda_b^0}} \int_{\Omega_p} \int_{\Omega_K} \varepsilon(pK^-|\vec{\theta}_p, \vec{\theta}_K) R(\vec{\theta}_{\Lambda_b^0}) |A(pK^-)|^2 \rho(\vec{\theta}_p, \vec{\theta}_K, \vec{\theta}_{\Lambda_b^0}) \mathrm{d}\vec{\theta}_p \mathrm{d}\vec{\theta}_K \mathrm{d}\vec{\theta}_{\Lambda_b^0} \tag{3.29}$$

$$\bar{N} \propto \int_{\Omega_{\Lambda_b^0}} \int_{\Omega_p} \int_{\Omega_K} \varepsilon(\bar{p}K^+|\vec{\theta}_p, \vec{\theta}_K) \bar{R}(\vec{\theta}_{\Lambda_b^0}) |\bar{A}(\bar{p}K^+)|^2 \rho(\vec{\theta}_p, \vec{\theta}_K, \vec{\theta}_{\Lambda_b^0}) \mathrm{d}\vec{\theta}_p \mathrm{d}\vec{\theta}_K \mathrm{d}\vec{\theta}_{\Lambda_b^0} \tag{3.30}$$

where $\varepsilon(\cdot|\cdot)$ is the reconstruction efficiency of a final state as a function of the kinematic variables relative to the two final state particles ($\vec{\theta}_p$ and $\vec{\theta}_K$), $R(\vec{\theta}_{\Lambda_b^0})$ ($\bar{R}(\vec{\theta}_{\Lambda_b^0})$) is the production rate of the Λ_b^0 ($\bar{\Lambda}_b^0$), and $|A(f)|^2$ ($|\bar{A}(\bar{f})|^2$) is the decay amplitude relative to $\Lambda_b^0 \to f$ ($\bar{\Lambda}_b^0 \to \bar{f}$). Note that $\rho(\vec{\theta}_p, \vec{\theta}_K, \vec{\theta}_{\Lambda_b^0})$ represents the distribution of the kinematic variables of the b hadron and of the two final state particles. For the $\Lambda_b^0 \to p\pi^-$ decay we have two relations completely analogous to Eqs. (3.29) and (3.30). Since the reconstruction efficiency of a particle as a function of its kinematics is independent from that of the other particle composing the decay, we can write:

$$\varepsilon(pK^-|\vec{\theta}_p, \vec{\theta}_K) = \varepsilon(p|\vec{\theta}_p)\varepsilon(K^-|\vec{\theta}_K) \ . \tag{3.31}$$

where the correlation between the two reconstruction efficiencies comes only from the correlation between the kinematic variables.

At this point it is appropriate to define various asymmetries as a function of the reconstruction efficiencies, the production rates, and the decay amplitudes. We can write the following detection asymmetries:

$$\mathcal{A}_D(p) = \frac{\varepsilon(p) - \varepsilon(\bar{p})}{\varepsilon(p) + \varepsilon(\bar{p})} \ , \tag{3.32}$$

$$\mathcal{A}_D(K) = \frac{\varepsilon(K^+) - \varepsilon(K^-)}{\varepsilon(K^+) + \varepsilon(K^-)} \ , \tag{3.33}$$

$$\mathcal{A}_D(\pi) = \frac{\varepsilon(\pi^+) - \varepsilon(\pi^-)}{\varepsilon(\pi^+) + \varepsilon(\pi^-)} \ , \tag{3.34}$$

where we have omitted the dependence from the kinematic variables in order to shorten the notation. Now note that Eqs. (3.32), (3.33) and (3.34) can be rewritten as:

$$\begin{aligned}
\varepsilon(p) &= \hat{\varepsilon}_p(1+\mathcal{A}_D(p)) \ , && (3.35)\\
\varepsilon(\bar{p}) &= \hat{\varepsilon}_p(1-\mathcal{A}_D(p)) \ , && (3.36)\\
\varepsilon(K^+) &= \hat{\varepsilon}_K(1+\mathcal{A}_D(K)) \ , && (3.37)\\
\varepsilon(K^-) &= \hat{\varepsilon}_K(1-\mathcal{A}_D(K)) \ , && (3.38)\\
\varepsilon(\pi^+) &= \hat{\varepsilon}_\pi(1+\mathcal{A}_D(\pi)) \ , && (3.39)\\
\varepsilon(\pi^-) &= \hat{\varepsilon}_\pi(1-\mathcal{A}_D(\pi)) \ , && (3.40)
\end{aligned}$$

where $\hat{\varepsilon}_p \equiv [\varepsilon(\bar{p})+\varepsilon(p)]/2$, $\hat{\varepsilon}_K \equiv [\varepsilon(K^+)+\varepsilon(K^-)]/2$ and $\hat{\varepsilon}_\pi \equiv [\varepsilon(\pi^+)+\varepsilon(\pi^-)]/2$ are the average reconstruction efficiencies of p, K, and π respectively.

The production asymmetry of the Λ_b^0 baryon can be defined as:

$$\mathcal{A}_P(\Lambda_b^0) = \frac{R(\vec{\theta}_{\Lambda_b^0}) - \bar{R}(\vec{\theta}_{\Lambda_b^0})}{R(\vec{\theta}_{\Lambda_b^0}) + \bar{R}(\vec{\theta}_{\Lambda_b^0})} \tag{3.41}$$

while the physical $\mathcal{CP}$ asymmetry for the final state $f = pK^-, p\pi^-$ is defined as:

$$\mathcal{A}_{\mathcal{CP}}(f) = \frac{|A(f)|^2 - |\bar{A}(\bar{f})|^2}{|A(f)|^2 + |\bar{A}(\bar{f})|^2} \tag{3.42}$$

Following the same reasoning applied to the detection asymmetries, we can rewrite Eqs. (3.41) and (3.42) in the following way:

$$\begin{aligned}
R &= \hat{R}(1+\mathcal{A}_P(\Lambda_b^0)) \ , && (3.43)\\
\bar{R} &= \hat{R}(1-\mathcal{A}_P(\Lambda_b^0)) \ , && (3.44)\\
|A(f)|^2 &\propto \hat{\mathcal{B}}(1+\mathcal{A}_{\mathcal{CP}}(f)) \ , && (3.45)\\
|\bar{A}(\bar{f})|^2 &\propto \hat{\mathcal{B}}(1-\mathcal{A}_{\mathcal{CP}}(f)) \ , && (3.46)
\end{aligned}$$

where we have defined the averaged production rate of Λ_b^0 baryons, $\hat{R} \equiv \left(R+\bar{R}\right)/2$, and the $\mathcal{CP}$ averaged branching ratio $\hat{\mathcal{B}}(f) \equiv \left(|A(f)|^2 + |\bar{A}(\bar{f})|^2\right)/2$. We can now use these definitions for the reconstruction efficiencies, production rates, and decay amplitudes together with Eq. (3.31) in Eqs. (3.29) and (3.30), obtaining for the pK^- raw asymmetry:

$$\begin{aligned}
&\mathcal{A}^{RAW}(pK^-) = \frac{N-\bar{N}}{N+\bar{N}} \simeq \\
&\simeq \mathcal{A}_{\mathcal{CP}}(pK^-)\frac{\int_{\Omega_{\Lambda_b^0}}\int_{\Omega_p}\int_{\Omega_K} \hat{\varepsilon}_p(\vec{\theta}_p)\hat{\varepsilon}_K(\vec{\theta}_K)\hat{R}(\vec{\theta}_{\Lambda_b^0})\rho(\vec{\theta}_p,\vec{\theta}_K,\vec{\theta}_{\Lambda_b^0})\mathrm{d}\vec{\theta}_{\Lambda_b^0}\mathrm{d}\vec{\theta}_p\mathrm{d}\vec{\theta}_K}{\int_{\Omega_{\Lambda_b^0}}\int_{\Omega_p}\int_{\Omega_K} \hat{\varepsilon}_p(\vec{\theta}_p)\hat{\varepsilon}_K(\vec{\theta}_K)\hat{R}(\vec{\theta}_{\Lambda_b^0})\rho(\vec{\theta}_p,\vec{\theta}_K,\vec{\theta}_{\Lambda_b^0})\mathrm{d}\vec{\theta}_{\Lambda_b^0}\mathrm{d}\vec{\theta}_p\mathrm{d}\vec{\theta}_K} +
\end{aligned}$$

$$+\frac{\int_{\Omega_{\Lambda_b^0}}\int_{\Omega_p}\int_{\Omega_K}\mathcal{A}_P(\Lambda_b^0)\hat{\varepsilon}_p(\vec{\theta}_p)\hat{\varepsilon}_K(\vec{\theta}_K)\hat{R}(\vec{\theta}_{\Lambda_b^0})\rho(\vec{\theta}_p,\vec{\theta}_K,\vec{\theta}_{\Lambda_b^0})\mathrm{d}\vec{\theta}_{\Lambda_b^0}\mathrm{d}\vec{\theta}_p\mathrm{d}\vec{\theta}_K}{\int_{\Omega_{\Lambda_b^0}}\int_{\Omega_p}\int_{\Omega_K}\hat{\varepsilon}_p(\vec{\theta}_p)\hat{\varepsilon}_K(\vec{\theta}_K)\hat{R}(\vec{\theta}_{\Lambda_b^0})\rho(\vec{\theta}_p,\vec{\theta}_K,\vec{\theta}_{\Lambda_b^0})\mathrm{d}\vec{\theta}_{\Lambda_b^0}\mathrm{d}\vec{\theta}_p\mathrm{d}\vec{\theta}_K}+$$
$$+\frac{\int_{\Omega_{\Lambda_b^0}}\int_{\Omega_p}\int_{\Omega_K}\mathcal{A}_D(p|\vec{\theta}_P)\hat{\varepsilon}_p(\vec{\theta}_p)\hat{\varepsilon}_K(\vec{\theta}_K)\hat{R}(\vec{\theta}_{\Lambda_b^0})\rho(\vec{\theta}_p,\vec{\theta}_K,\vec{\theta}_{\Lambda_b^0})\mathrm{d}\vec{\theta}_{\Lambda_b^0}\mathrm{d}\vec{\theta}_p\mathrm{d}\vec{\theta}_K}{\int_{\Omega_{\Lambda_b^0}}\int_{\Omega_p}\int_{\Omega_K}\hat{\varepsilon}_p(\vec{\theta}_p)\hat{\varepsilon}_K(\vec{\theta}_K)\hat{R}(\vec{\theta}_{\Lambda_b^0})\rho(\vec{\theta}_p,\vec{\theta}_K,\vec{\theta}_{\Lambda_b^0})\mathrm{d}\vec{\theta}_{\Lambda_b^0}\mathrm{d}\vec{\theta}_p\mathrm{d}\vec{\theta}_K}-$$
$$-\frac{\int_{\Omega_{\Lambda_b^0}}\int_{\Omega_p}\int_{\Omega_K}\mathcal{A}_D(K|\vec{\theta}_K)\hat{\varepsilon}_p(\vec{\theta}_p)\hat{\varepsilon}_K(\vec{\theta}_K)\hat{R}(\vec{\theta}_{\Lambda_b^0})\rho(\vec{\theta}_p,\vec{\theta}_K,\vec{\theta}_{\Lambda_b^0})\mathrm{d}\vec{\theta}_{\Lambda_b^0}\mathrm{d}\vec{\theta}_p\mathrm{d}\vec{\theta}_K}{\int_{\Omega_{\Lambda_b^0}}\int_{\Omega_p}\int_{\Omega_K}\hat{\varepsilon}_p(\vec{\theta}_p)\hat{\varepsilon}_K(\vec{\theta}_K)\hat{R}(\vec{\theta}_{\Lambda_b^0})\rho(\vec{\theta}_p,\vec{\theta}_K,\vec{\theta}_{\Lambda_b^0})\mathrm{d}\vec{\theta}_{\Lambda_b^0}\mathrm{d}\vec{\theta}_p\mathrm{d}\vec{\theta}_K}\ , \tag{3.47}$$

where the branching ratios are simplified in each term of the sum and where we have neglected terms in the asymmetries higher than the second order. Note that a completely analogous equation holds also in the case of $p\pi^-$ final state. The expression:

$$\int_{\Omega_{\Lambda_b^0}}\int_{\Omega_p}\int_{\Omega_K}\hat{\varepsilon}_p(\vec{\theta}_p)\hat{\varepsilon}_K(\vec{\theta}_K)\hat{R}(\vec{\theta}_{\Lambda_b^0})\rho(\vec{\theta}_p,\vec{\theta}_K,\vec{\theta}_{\Lambda_b^0})\mathrm{d}\vec{\theta}_{\Lambda_b^0}\mathrm{d}\vec{\theta}_p\mathrm{d}\vec{\theta}_K \tag{3.48}$$

represent the distribution of the kinematic variables relative to the reconstructed decays. For this reason, Eq. (3.47) and its analogous for the $p\pi^-$ final state can be written as:

$$\mathcal{A}^{RAW}(pK^-) \simeq \mathcal{A}_{\mathcal{CP}}(pK^-) + \hat{\mathcal{A}}_P(\Lambda_b^0) + \hat{\mathcal{A}}_D(p) - \hat{\mathcal{A}}_D(K)\ , \tag{3.49}$$
$$\mathcal{A}^{RAW}(p\pi^-) \simeq \mathcal{A}_{\mathcal{CP}}(p\pi^-) + \hat{\mathcal{A}}_P(\Lambda_b^0) + \hat{\mathcal{A}}_D(p) - \hat{\mathcal{A}}_D(\pi)\ , \tag{3.50}$$

where the Λ_b^0 production asymmetry and the proton, kaon, and pion detection asymmetries are mediated over the distributions of the kinematic variables relative to the b hadron and to the final state particles.

Finally we can write the following relation between the two raw asymmetries and the two $\mathcal{CP}$ asymmetries:

$$\begin{aligned}
&\mathcal{A}^{RAW}(pK^-) - \mathcal{A}^{RAW}(p\pi^-) = \\
&= \mathcal{A}_{\mathcal{CP}}(pK^-) + \hat{\mathcal{A}}_P(\Lambda_b^0) + \hat{\mathcal{A}}_D(p) - \hat{\mathcal{A}}_D(K) - \mathcal{A}_{\mathcal{CP}}(p\pi^-) - \hat{\mathcal{A}}_P(\Lambda_b^0) - \hat{\mathcal{A}}_D(p) + \hat{\mathcal{A}}_D(\pi) = \\
&= \mathcal{A}_{\mathcal{CP}}(pK^-) - \mathcal{A}_{\mathcal{CP}}(p\pi^-) + \hat{\mathcal{A}}_D(\pi) - \hat{\mathcal{A}}_D(K)\ ,
\end{aligned} \tag{3.51}$$

that can be rewritten as:

$$\Delta\mathcal{A}_{\mathcal{CP}} = \Delta\mathcal{A}^{RAW} + \hat{\mathcal{A}}_D(K) - \hat{\mathcal{A}}_D(\pi) \tag{3.52}$$

where $\Delta\mathcal{A}_{\mathcal{CP}} \equiv \mathcal{A}_{\mathcal{CP}}(pK^-) - \mathcal{A}_{\mathcal{CP}}(p\pi^-)$ and $\Delta\mathcal{A}^{RAW} \equiv \mathcal{A}^{RAW}(pK^-) - \mathcal{A}^{RAW}(p\pi^-)$. As can be seen from Eq. (3.52), the Λ_b^0 production asymmetry and the proton detection asymmetry cancel in the difference.

The LHCb Collaboration has measured two values for $\mathcal{A}_D(K^+\pi^-)$ in a previous analysis using $H_b \to h^+h'^-$ decays [15]. These two quantities are reported in Tab. 3.17 and are related to different selections optimized to extract the $\mathcal{CP}$ asymmetries of $B^0 \to K^+\pi^-$ and $B_s^0 \to \pi^+K^-$ decays. In our analysis we use the mean value of the two detection asymmetries. Before considering the statistical uncertainty to be associated to this value we note that the data sample used to compute the two detection asymmetries is the same (only the selections are different). This means that the two detection asymmetries computed in [15] have a very high correlation. For this reason, we chose conservatively to adopt as statistical uncertainty for $\mathcal{A}_D(K^+\pi^-)$ the largest one reported in Tab. 3.17. Thus the detection asymmetry calculated after these considerations results to be $\mathcal{A}_D(K^+\pi^-) = (-1.19 \pm 0.23)\%$.

Detection asymmetry	Value
$\mathcal{A}_D(K^+\pi^-)$ from $B^0 \to K^+\pi^-$	$(-1.15 \pm 0.23)\%$
$\mathcal{A}_D(K^+\pi^-)$ from $B_s^0 \to \pi^+K^-$	$(-1.22 \pm 0.21)\%$

Table 3.17: Kaon-pion detection asymmetries measured by the LHCb Collaboration in [15].

For the same considerations used in Eq. (3.31) we can then write:

$$\mathcal{A}_D(K^+\pi^-) = \mathcal{A}_D(K) - \mathcal{A}_D(\pi) \ , \tag{3.53}$$

that equals the detection asymmetry terms entering Eq. (3.52).

Using the raw asymmetries reported in Tabs. 3.15 and 3.16 and the value of $\mathcal{A}_D(K^+\pi^-)$, we can compute

$$\Delta\mathcal{A}_{\mathcal{CP}} = (0.8 \pm 2.1 \pm 0.2)\% \ , \tag{3.54}$$

where the first uncertainty is statistical and the second comes from that on $\mathcal{A}_D(K^+\pi^-)$. No evidence for $\mathcal{CP}$ violation is observed.

Conclusions

A measurement of $\mathcal{CP}$ violation in charmless charged two-body decays of the Λ_b^0 baryon has been presented. The quantity that has been measured is $\Delta\mathcal{A}_{\mathcal{CP}} = \mathcal{A}_{\mathcal{CP}}(pK^-) - \mathcal{A}_{\mathcal{CP}}(p\pi^-)$, where $\mathcal{A}_{\mathcal{CP}}(pK^-)$ and $\mathcal{A}_{\mathcal{CP}}(p\pi^-)$ are the direct $\mathcal{CP}$ asymmetries in $\Lambda_b^0 \to pK^-$ and $\Lambda_b^0 \to p\pi^-$ decays. If this quantity differs from zero, the presence of $\mathcal{CP}$ violation is implied, whereas if it is compatible with zero, $\mathcal{CP}$ violation cannot be excluded.

The analysis has been realised using the entire sample of pp collisions collected in 2011 and 2012 with the LHCb detector, corresponding to a total integrated luminosity of about 3 fb^{-1}. Two multivariate selections based on a boosted decision tree algorithm have been optimised separately for $\Lambda_b^0 \to pK^-$ and $\Lambda_b^0 \to p\pi^-$ decays, with the aim of achieving the best statistical sensitivity on the $\mathcal{CP}$ asymmetries. Particular attention has been paid to the calibration of the particle identification performance, as the selection of the decays under study is affected by a sizable background coming from other two-body decays of b hadrons, where one or both final state particles are misidentified. For this reason, the pK^- and $p\pi^-$ invariant mass spectra are characterized by a large number of background components, which have been accurately modelled while defining the probability density functions to be used in binned maximum likelihood fits. These fits have been performed to obtain the so-called raw asymmetries, *i.e.* the uncorrected relative differences between the yields of charge-conjugate final states in each of the two Λ_b^0 decays. Finally, the $\mathcal{CP}$-violating quantity $\Delta\mathcal{A}_{\mathcal{CP}}$ has been determined taking into account corrections to the raw asymmetries due to asymmetric detection efficiencies of charge-conjugate final states.

The main result of this thesis is then

$$\Delta\mathcal{A}_{\mathcal{CP}} = (0.8 \pm 2.1 \pm 0.2)\%,$$

where the first uncertainty is statistical, whereas the second comes from the uncertainty on the detection asymmetry between the charge-conjugate final states. Albeit a complete study of the systematic uncertainties affecting this measurement is still lacking, one can already conclude that there is no evidence for $\mathcal{CP}$ violation with the present experimental precision. This is the first time that $\mathcal{CP}$ violation is probed in two-body decays of Λ_b^0 baryons. To date, $\mathcal{CP}$ violation has not been observed in any baryon decay.

There are still two tasks to be accomplished before this work can be turned into a publication. The first is to quantify the size of the possible asymmetric production

between Λ_b^0 and $\bar{\Lambda}_b^0$ baryons arising from the primary pp collisions. Once the production asymmetry of Λ_b^0 baryons is known, it will possible to determine $\mathcal{A}_{\mathcal{CP}}(pK^-)$ and $\mathcal{A}_{\mathcal{CP}}(p\pi^-)$ separately. The presence of such an initial asymmetry would in fact mimic $\mathcal{CP}$ violation in the decays, thus obfuscating the measurement of the two $\mathcal{CP}$ asymmetries. This problem is not present when measuring $\Delta\mathcal{A}_{\mathcal{CP}}$, as the presence of a production asymmetry term is cancelled in the difference. The second task is the study of systematic uncertainties. The main components contributing to the systematic uncertainty affecting the measurement are already well known. They can be grouped into three categories: PID calibration, fitting model, and instrumental and production asymmetries. These further studies will be completed within the analysis activities of the LHCb Bologna group.

Appendix A

Multivariate analysis

In order to further enhance the separation between signal and background in the decay channels of interest for this analysis, we have employed a multivariate analysis technique. This approach uses different parameters x_i measured in each event, *e.g.* p_T^{track}, IP^{track} and others, to improve the separation between signal and background events, exploiting the different distributions of these parameters. In order to have an easier evaluation of the cuts that lead to the best separation, the parameters are combined in just one function, called test statistic t [68]:

$$\vec{x} = (x_1, \ldots, x_n) \rightarrow t(x_1, \ldots, x_n). \tag{A.1}$$

The goal is to make a statement about how well the observed data stand in agreement with given predicted probabilities, *i.e.* a hypothesis. The hypothesis under consideration is usually called null hypothesis H_0 which can specify, for example, a probability density $f(x)$. If the p.d.f. depends on one or more unknown parameters, then the hypothesis is said to be composite, while if it only depends on the variable then it is called simple.

A statement about the validity or the likelihood of the H_0 hypothesis often involves a comparison with some other alternative hypotheses $H_1, H_2, \ldots$. Now suppose that we have a data sample consisting in n measured quantities $\vec{x} = (x_1, \ldots, x_n)$ and two hypotheses H_0 and H_1, specifying two p.d.f.'s $f(\vec{x} \mid H_0)$ and $f(\vec{x} \mid H_1)$. For example, H_0 could be the signal+background hypothesis for an event and H_1 could be the background only hypothesis for the same event. In order to measure the agreement between the observed data and a given hypothesis then one constructs the test statistic $t(x_1, \ldots, x_n)$ that will have the p.d.f. $g(t \mid H_0)$ if H_0 is correct and $g(t \mid H_1)$ if H_1 is correct. The situation is represented in Fig. A.1.

We can now define a critical region for t or equivalently its complement called acceptance region. If the value of t, determined from the x_n measured quantities, is above a certain threshold t_{cut}, then we decide to reject the hypothesis H_0, that for example can be our signal hypothesis and in this case the event will be classified as background. On the contrary, if $t < t_{cut}$, we accept H_0 and our event will be classified as a signal event.

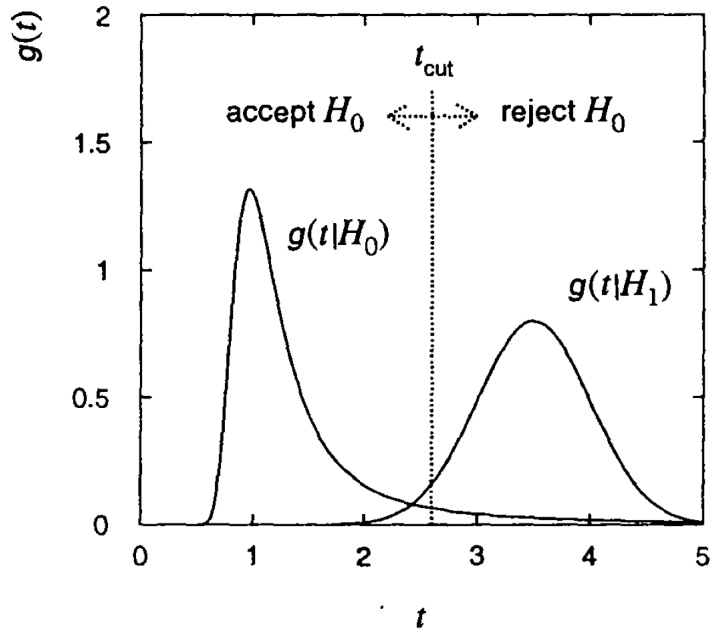

Figure A.1: Probability density function for test statistic t under the assumption of the hypothesis H_0 and H_1. The hypothesis H_0 is rejected if $t > t_{cut}$ and is accepted if $t < t_{cut}$.

The critical region is chosen as the region where the probability for t to be observed there under the assumption of the hypothesis H_0 is some value α, called the significance level of the test:

$$\alpha = \int_{t_{cut}}^{+\infty} g(t \mid H_0)\mathrm{d}t \quad . \tag{A.2}$$

There is thus a probability α that we will reject H_0 even if it is true. This is called an error of the first kind; instead, an error of the second kind happens when H_0 is accepted (*i.e.* t observed is less than t_{cut}), but the true hypothesis was H_1. The probability for this to happen is:

$$\beta = \int_{-\infty}^{t_{cut}} g(t \mid H_1)\mathrm{d}t \tag{A.3}$$

where $1 - \beta$ is called the power of the test to discriminate against the alternative hypothesis H_1.

We have chosen to adopt the boosted decision trees to perform our multivariate analysis due to the straightforward nature of the decision trees, consisting in a set a binary conditions imposed on an event, and due to the performances of the method itself, that often outperforms other multivariate methods. A drawback of decision trees is their instability with respect to statistical fluctuations in the training sample from which the tree structure is derived. To overcome this problem we have then constructed

a forest of decision trees, procedure known as *boosting*. In this way, the stability against statistical fluctuations of the method and its separation power are greatly improved.

We will now describe in detail the main characteristics of this multivariate analysis method.

A.1 Decision trees

The decision tree is a binary structure in which events are classified based on a set of subsequent yes/no decisions taken on a single discriminating variable at a time. This situation is sketched in Fig. A.2. The process continues until a selection criterion is reached; typically an event is classified as signal or background when the percentual of events of the same type in a node reaches a certain threshold. In this way, the phase space formed by the discriminating variables is divided in several multidimensional regions, that will contain signal or background events on the basis of the cuts imposed.

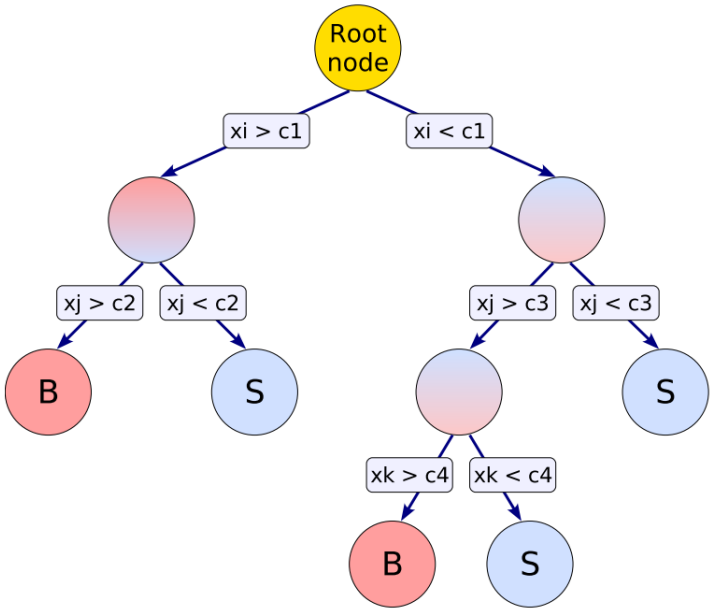

Figure A.2: Schematic representation of a decision tree. Starting from a root node, a sequence of binary splits is applied to determine if an event is signal-like (S) or background-like (B). The cut used in each decision is chosen as the one that gives the best discrimination. The leaves at the ends of the tree are labelled as S or B, depending on the majority of events that populates each final node.

The training of a decision tree is the process that defines the splitting criteria for

each node. This starts with the root node, where an initial splitting criterion for the full training sample is determined; this results in two subsets of training events each of which goes through the same algorithm in order to determine the next splitting criterion. This is done until the whole tree is built, *i.e.* until a node contains a percentual that lies over a certain threshold of events of the same type (signal or background). The training sample is usually composed by a dataset containing signal events tanken from the data sample signal region and by a dataset containing background events taken from a side-band composed only by combinatorial background events. The decision tree chooses the best cutting variable to be used in each node basing its decision on a series of coefficients defined as:

$$G_{ini} = \left(\sum_{i=1}^{n} w_i \right) P_S(1 - P_S) \tag{A.4}$$

where the w_i are the events weights and $P_S = N_S/(N_S + N_B)$, with N_S and N_B standing respectively for the number of signal and background events. The cut applied in each node is chosen in order to maximize the quantity:

$$C = G_{ini}^{parent} - (G_{ini}^{left\ child} + G_{ini}^{right\ child}). \tag{A.5}$$

where G_{ini}^{parent} refers to the node upon which the cut will be applied and G_{ini}^{child} refers to the two resulting nodes after the splitting procedure. In this way, the maximum separation between signal and background events is obtained (in fact, if $P_S^{child} = 1$, then according to Eq. (A.4) one child contains only signal events and the other child contains only background events and thus the C quantity is maximized).

The main disadvantage of decision trees is that they are susceptible to statistical fluctuations and if that happens in a initial decision node then the structure below that node is altered, possibly resulting in a different classifier response. This problem is overcome adopting a procedure called *boosting*, that we are now going to describe.

A.1.1 Boosting

The problems listed in the previous section can be solved adopting the procedure known as boosting. This consists in growing a forest of decision trees where all the trees used are derived from the same training sample instead of using only one decision tree. Every tree will have a weight α and thus an event will be classified on the base of the relative mean of the scores T_i obtained from each decision tree, defined as:

$$T_i = \sum_{m=1}^{N_{DT}} T_{i,m} \alpha_m \tag{A.6}$$

where N_{DT} stands for the number of decision trees, α_m is the weight assigned to each tree and $T_{i,m}$ is the score for the event i given by the m-th decision tree. After the

application of a decision tree, the mis-classified events are reweighted and a new decision tree is constructed and optimized with those events. This is repeated until the desired degree of separation is reached.

The boosting procedure leads to an increase in the statistical stability of a classifier against the fluctuations, that is one of the major weak points affecting the use of decision trees. Moreover, boosting also increases the separation performance of the classifier.

Appendix B

Maximum likelihood fits

We have performed maximum likelihood fits to extract the parameters of interest for the analysis. We are now going to describe the theoretical basis on which the maximum likelihood works.

We can write the total p.d.f. comprehending the signal and background model and using the invariant mass as a discriminating variable as follows:

$$f(m|\vec{\alpha},\ \vec{\beta},\ p) = p \cdot s(m \mid \vec{\alpha}) + (1-p) \cdot b(m \mid \vec{\beta}) \tag{B.1}$$

where m is the invariant mass, $s(\cdot)$ and $b(\cdot)$ are respectively the signal and background p.d.f.'s, $\vec{\alpha}$ and $\vec{\beta}$ are the parameters needed to determine the shapes of $s(\cdot)$ and $b(\cdot)$ and p is the fraction of signal events. The method of maximum likelihood is a technique for estimating the values of the parameters given a finite sample of data. Assuming the hypothesis $f(m|\vec{\alpha},\ \vec{\beta},\ p)$, the probability for the first measurement to be in the interval $[m_1, m1 + \mathrm{d}m_1]$ is $f(m_1|\vec{\alpha},\ \vec{\beta},\ p)\mathrm{d}m_1$. Since the measurements are all independent, the probability to have the first one in $[m_1, m_1 + \mathrm{d}m_1]$, the second in $[m_2, m_2 + \mathrm{d}m_2]$ and so on is given by the expression:

$$P(m_i \in [m_i, m_i + dm_i]) = \prod_{i=1}^{n} f(m_i|\vec{\alpha},\ \vec{\beta},\ p)\mathrm{d}m_i \tag{B.2}$$

where n is the number of independent measurements one has. If the chosen model and parameter values are correct, one expects a high probability for the data actually measured. Since the $\mathrm{d}m_i$ do not depend on the parameters, the same reasoning can also be applied to the function:

$$\mathcal{L}(\vec{\alpha},\ \vec{\beta},\ p) = \prod_{i=1}^{n} f(m_i|\vec{\alpha},\ \vec{\beta},\ p) \tag{B.3}$$

called the likelihood function.

At this point we can define the maximum likelihood estimators as those which maximize the likelihood function, *i.e.* the parameters that give the highest probability for the measurements obtained, as (using the notation $\vec{\theta}$ for all the k parameters considered in the analysis):

$$\frac{\partial \mathcal{L}}{\partial \theta_i} = 0, \quad i = 1, \ldots, k \tag{B.4}$$

Rather than using the likelihood function as defined in Eq. (B.3) it is usually more convenient the use its logarithm. The log-likelihood function is then:

$$-\log \mathcal{L}(\vec{\theta}) = -\sum_{i=1}^{n} \log f(m_i|\ \vec{\theta}) \ , \tag{B.5}$$

where often the sign is changed from positive to negative; this means that searching the maximum of the $\mathcal{L}$ function corresponds to searching the minimum of the $-\log \mathcal{L}$ function (as the logarithm is a monotonic increasing function). This is done in order to soften the calculus requirements involved in the determination of the best estimators for the parameters.

Since often it is too much difficult to find it analytically, the distribution of the ML estimates can be investigated with various methods. One of the most adopted methods uses the Rao-Cramér-Frechet (RCF) inequality, also called the information inequality, which gives a lower bound on an estimator's variance. For the case of a single parameter, the limit on the estimator's variance is given by:

$$V[\hat{\theta}] \geq \left(1 + \frac{\partial b}{\partial \theta}\right)^2 \Big/ E\left[-\frac{\partial^2 \log \mathcal{L}}{\partial \theta^2}\right], \tag{B.6}$$

where $V[\cdot]$ stands for the variance of a parameter, $E[\cdot]$ is the expectation value of a parameter, $\mathcal{L}$ is the likelihood function and b is the bias as defined by:

$$b = E[\hat{\theta}] - \theta \ . \tag{B.7}$$

In the case of equality instead of the upper limit in Eq. (B.6), *i.e.* in the case of minimum variance, the estimator is said to be efficient; it has been shown that if efficient estimators exist for a given problem, then the maximum likelihood method will find them.

In our case, we do not have a single parameter, but a vector of paramaters $\vec{\theta} = (\theta_1, \ldots, \theta_k)$, and so Eq. (B.6) becomes:

$$(V^{-1})_{ij} = E\left[-\frac{\partial^2 \log \mathcal{L}}{\partial \theta_i \partial \theta_j}\right] \ , \tag{B.8}$$

where we have assumed efficiency and zero bias and where V^{-1} stands for the inverse of the covariance matrix V; Eq. (B.8) can also be written as:

$$(V^{-1})_{ij} \ = \ \int \ldots \int -\frac{\partial^2}{\partial \theta_i \partial \theta_j} \left(\sum_{q=1}^{n} \log f(m_q \mid \vec{\theta})\right) \prod_{r=1}^{n} f(m_r \mid \vec{\theta})\ \mathrm{d}m_r =$$

$$= \quad n \cdot \int -f(m \mid \vec{\theta}) \frac{\partial^2}{\partial\theta_i \partial\theta_j} \log f(m \mid \vec{\theta}) \, \mathrm{d}x \ , \tag{B.9}$$

where $f(m \mid \vec{\theta})$ is the likelihood function for the random variable m, for which one has n measurements. We can clearly see that $V^{-1} \propto n$ and thus it is clear that the parameters statistical error computed through Eq. (B.9) decreases proportionally to $1/\sqrt{n}$. This analytical approach is usually impractical to compute and so one often estimates the V^{-1} using the measured data and the maximum likelihood estimates $\hat{\theta}$:

$$(\widehat{V^{-1}})_{ij} = -\frac{\partial^2 \log \mathcal{L}}{\partial\theta_i \partial\theta_j}\bigg|_{\vec{\theta}=\hat{\vec{\theta}}} \ , \tag{B.10}$$

that for a single parameter θ reduces to:

$$\widehat{\sigma^2_{\hat{\theta}}} = \left(-1 \Big/ \frac{\partial^2 \log \mathcal{L}}{\partial\theta^2} \right) \bigg|_{\theta=\hat{\theta}} \ . \tag{B.11}$$

The method implemented by the routines *Migrad* and *Hesse* in the program *Minuit* used by *RooFit* calculates numerically the matrix of second derivatives of the $\log \mathcal{L}$ function, evaluates the ML estimates and finds the covariance matrix of all the parameters involved in the fit procedure. This matrix is then inverted to obtain the estimates for the parameter errors.

Bibliography

[1] C. S. Wu, E. Ambler, R. W. Hayward, D. D. Hoppes, and R. P. Hudson *Experimental Test of Parity Conservation in Beta Decay*, *Phys.Rev.* **105**, 1143, (1957).

[2] M. Goldhaber, L. Grodzins, and A. W. Sunyar, *Helicity of Neutrinos*, *Phys.Rev.* **109**, 1015, (1958).

[3] J. H. Christensen *et .al*, *Phys.Rev.Lett.* **13**, 138, (1964).

[4] S. L. Glashow, J. Iliopoulos and L. Maiani, *Phys. Rev.* **D2**, 1285-1292, (1970).

[5] J. J. Aubert *et al.*, *Experimental Observation of a Heavy Particle J*, *Phys.Rev.Lett* **33**, 1404, (1974).

[6] J. E. Augustin *et al.*, *Discovery of a Narrow Resonance in e^+e^- Annihilation*, *Phys.Rev.Lett.* **33**, 1409, (1974).

[7] M. Kobayashi and T. Maskawa, *$\mathcal{CP}$-Violation in the Renormalizable Theory of Weak Interaction Prog.Theor.Phys.* **49**, 652, (1973).

[8] S. W. Herb *et. al.*, *Observation of a Dimuon Resonance at 9.5 GeV in 400-GeV Proton-Nucleus Collisions*, *Phys.Rev.Lett.* **39**, 252, (1977).

[9] F. Abe *et al.* (CDF Collaboration), *Observation of Top Quark Production in $p\bar{p}$ Collisions with the Collider Detector at Fermilab*, *Phys.Rev.Lett.* **74**, 2626, (1995).

[10] S. Abachi *et al.* (D0 Collaboration), *Search for High Mass Top Quark Production in $p\bar{p}$ Collisions at $\sqrt{s} = 1.8$ TeV*, *Phys.Rev.Lett.* **74**, 2422, (1995).

[11] A. Abulencia *et al.* (CDF Collaboration) *Observation of $B_s^0 - -\bar{B}_s^0$ Oscillations*, *Phys.Rev.Lett.* **97**, 242003, (2006).

[12] R. Aaij *et al.*, [LHCb Collaboration], *Observation of $D^0 - \bar{D}^0$ oscillations*, *Phys.Rev.Lett.* **110**, 101802, (2013).

[13] B. Aubert *et al.* (BaBar Collaboration), *Observation of **CP** Violation in the B^0 Meson System*, *Phys.Rev.Lett.* **87**, 091801, (2001).

[14] K.Abe *et al.* (Belle Collaboration) *Observation of Large **CP** Violation in the Neutral **B** Meson System*, *Phys.Rev.Lett.* **87**, 091802, (2001).

[15] R. Aaij *et. al.*, (LHCb Collaboration), *First observation of CP violation in the decays of B_s^0 mesons*, *Phys.Rev.Lett.* **110**, (2013).

[16] B. Aubert *et al.*, (BaBar Collaboration), arXiv:0807.4226v2 (hep-ex).

[17] B. Aubert *et al.*, (BaBar Collaboration), *Phys.Rev.Lett* **87**, 091801, (2001).

[18] K. Abe *et al.*, (Belle Collaboration), *Phys.Rev.Lett.* **87**, 091802, (2001).

[19] H. Burkhardt *et al.*, (NA31 Collaboration), *Phys.Lett.* **B206**, 169, (1998).

[20] V.Fanti *et al.*, (NA48 Collaboration), *Phys.Lett.* **B465**, 335, (1999).

[21] A. Alavi-Harti *et al.*, (KTeV Collaboration), *Phys.Rev.Lett.* **83**, 22, (1999).

[22] B. Aubert *et al.*, (BaBar Collaboration), *Phys.Rev.Lett.* **93**, 131801, (2004).

[23] K. Abe *et al.*, (Belle Collaboration), arXiv:hep-ex/0507045.

[24] B. Aubert *et al.*, (BaBar Collaboration), *Phys.Rev.* **D72**, 072003, (2005).

[25] A. Garmash *et al.*, (Belle Collaboration), *Phys.Rev.Lett.* **96**, 251803, (2006).

[26] R. Aaij *et al.*, (LHCb Collaboration), CERN-PH-EP-2011-206.

[27] A. D. Sakharov, *Violation Of CP Invariance, C Asymmetry, And Baryon Asymmetry Of The Universe*, *Pisma Zh. Exp. Theor. Fiz.* **5**, 32, (1967), English translation in *JETP Lett.* **5**, 24 (1967), reprinted in *Sov.Phys.Usp. 34*, 392, (1991).

[28] T. D. Lee, *Particle physics and introduction to field theory*, Harwood Academic Publishers (1981).

[29] N. Cabibbo, *Phys.Rev.Lett.* **10**, 531, (1963).

[30] B. J. Bjørken and S. L. Glashow, *Phys.Lett.* **B11**, 255-257, (1964).

[31] C. Jarlskog, *Phys.Rev.Lett.* **55**, 1039, (1985)

[32] L. Wolfenstein, *Phys.Rev.Lett.* **51**, 1945, (1983)

[33] UTfit Collaboration web pages, *http://www.utfit.org/UTfit/*.

[34] M. Ciuchini et al., *JHEP* **0107**, 013 (2001), [arXiv:hep-ph/0012308].

[35] *Unitary Triangle Fit*, http://www.utfit.org/UTfit/ResultsSummer2013PostEPS.

[36] R. Fleischer, *B Physics and CP Violation, Lect. Notes Phys.* **647**, 42-77, (2004).

[37] G. Buchalla, A. J. Buras, M. E. Lautenbacher, *Weak decays beyond leading logarithms*, *Rev.Mod.Phys.* **68**, 1125-1144, (1996).

[38] R. Fleischer, *Phys.Rep.* **370**, 531, (2002).

[39] M. Gronau and D. London, *Phys.Lett.* **B253**, 483, (1991);
M. Gronau and D. Wyler, *Phys.Lett.* **B265**, 172, (1991).

[40] D. Atwood, I. Dunietz and A. Soni, *Phys.Rev.Lett.* **78**, 3257, (1997);
D. Atwood, I. Dunietz and A. Soni, *Phys.Rev.* **D63**, 036005, (2001).

[41] A. A. Alves *et. al.* (LHCb Collaboration), *JINST* **3**, S08005, (2008).

[42] The CERN Large Hadron Collider: Accelerator and Experiments, *JINST* **3**, S08001, (2008).

[43] R. Aaij *et. al.*, (LHCb Collaboration), *Measurement of the* $\sigma(pp \to b\bar{b}X)$ *at* $\sqrt{s} = 7\ TeV$, *Phys.Lett.* **B694**, 209, (2010).

[44] (LHCb Collaboration), *Prompt charm production in pp collisions at* $s = \sqrt{7}\ TeV$, LHCb-CONF-2010-013.

[45] (LHCb Collaboration), CERN-LHCC-2001-011.

[46] (LHCb Collaboration), CERN-LHCC-2003-030.

[47] (LHCb Collaboration), CERN-LHCC-2003-031.

[48] (LHCb Collaboration), CERN-LHCC-2002-029.

[49] (LHCb Collaboration), CERN-LHCC-2001-024.

[50] (LHCb Collaboration) CERN-LHCC-2000-007.

[51] (LHCb Collaboration), CERN-LHCC-2000-037.

[52] (LHCb Collaboration), CERN-LHCC-2000-036.

[53] William R. Leo, *Techniques for Nuclear and Particle Physics Experiments - 2nd Revised Edition*, Springer, (1994).

[54] H. Fessler *et al.*, *Nucl.Instr. and Meth.* **A240**, 284, (1985).

[55] G. S. Atoyan *et al.*, *Nucl.Instr. and Meth.* **A320**, 144, (1992).

[56] I. Machikhiliyan (LHCb Collaboration), *Current status and perfomance of the LHCb electromagnetic and hadron calorimeters*, *Journal of Physics: Conference Series (CALOR 2010)*, 6, (2010)

[57] (LHCb Collaboration), CERN-LHCC-2003-002.

[58] M. Adinolfi *et .al.* (The LHCb RICH Collaboration), *Performance of the LHCb RICH detector at the LHC*, *Eur.Phys.Jour.* **C73**, 2431, (2013).

[59] Torbjörn Sjöstrand, Stephen Mrenna and Peter Skans, *PYTHIA 6.4 physics and manual*, *JHEP* **05**, (2006).

[60] Torbjörn Sjöstrand, Stephen Mrenna and Peter Skans, *A brief introduction to PYTHIA 8.1*, *Comput.Phys.Commun.* **187**, 825-867, (2008).

[61] Belyaev, I. and others, *Handling of the generation of primary events in Gauss, the LHCb simulation framework*, *Nuclear Science Symposium Conference Record (NSS/MIC)* **IEEE**, (2010).

[62] Lange, D. J., *The EvtGen particle decay simulation package*, *Nucl.Instrum.Meth.* **A462**, 152-155, (2001).

[63] Piotr Golonka and Zbigniew Was, *PHOTOS Monte Carlo: a precision tool for QED corrections in Z and W decays*, *Eur.Phys.J.* **C45**, 97-107, (2006).

[64] John Allison, K. Amako, J. Apostolakis, H. Araujo, P.A. Dubois and others, *Geant4 developments and applications*, *IEEE Trans.Nucl.Sci.* **53**, (2006).

[65] S. Agostinelli and others, *Geant4: a simulation toolkit*, *Nucl.Instrum.Meth.* **A506**, (2003).

[66] M. Clemencic and others, *The LHCb simulation application, Gauss: design, evolution and experience*, *J.Phys.Conf.Ser.* **331**, (2011).

[67] Muriel Pivk and Francois R. Le Diberder *sPlot: a statistical tool to unfold data distributions*, *Nucl.Instrum.Meth.* **A555**, 356-369, (2005).

[68] G. Cowan, *Statistical Data Analysis*, Oxford University Press (1998).

[69] E. Baracchini and G. Isidori *Phys.Lett.B* **663** p.309, (2006) [arXiv:hep-ph/0508071].

[70] (LHCb Collaboration), *Roadmap for selected key measurements of LHCb*, LHCb-PUB-2009-029, (2009).

[71] Kyle S. Cranmer, *Kernel Estimation in High-Energy Physics*, *Comput.Phys.Commun.* **136**, 198-207, (2001).

[72] H. Albrecht *et. al.* (ARGUS Collaboration), *Search for hadronic $b \to u$ decays*, *Phys.Lett.* **B241**, 278-282, (1990).

[73] W. Verkerke and D. Kirkby, *Proceedings of 2003 Conference for Computing in High-Energy and Nuclear Physics (CHEP 03), La Jolla, California, 2003* [arXiv:physics/0306116].

[74] R. Aaij *et al.*, (LHCb Collaboration), *Measurement of b-hadron branching fractions for two-body decays into charmless charged hadrons*, *J.High.Energy.Phys.* **10**, 037, (2012).

[75] F. James, Minuit Reference Manual, `http://wwwinfo.cern.ch/asdoc/minuit/minmain.ht`.

Acknowledgements

Having reached the end of my studies, I think that it is time to thank all the people that made beautiful these five years inside the Department of Physics in Bologna.

First of all, I would like to thank my parents, Edo and Rosella, for they continuous support and encouragement throughout all these years of study. I would not have achieved all the results I have obtained without them.

Secondly, I sincerely thank all the Bologna LHCb Group for they patience and their effort to teach me all their knowledge about flavour physics. In particular, I am in debt with Stefano for his aid and his commitment in preparing this analysis with me, and with Angelo for the work done with him for my Degree thesis and for his continuous support in this analysis. I would also like to thank Vincenzo, Umberto, Domenico, and Maria for their friendship during this period with them. I think that the first important thing in an office is to work hard with a smile always on your face and I think that I have found such a place with you.

I thank my two best friends JJ and Palma for all the moments together and for their patience in listening me talking about some random and boring science stuff. I also thank Fabiana for bearing the above mentioned JJ. Finally I thank Paolo, Pede, Selena, Elisa, Mimì, Eleonora, Melissa, Francesco, Pasqua, Bi, and Charlie for the time passed together.

I would also like to thank Il Fattone, Pedo, Davide, Boccio, Conni, Grazia, Alessandra, Giulia, Camilla, Francesca, Costanza, Alba, Martelli, Leo, Fillo, Bush, Martì, Arianna, Roberta, Onofrio, Mirko, Enrico, Lucio, Barbi, Ascanio, Carmine (or Mattia?), Maria Celeste, Erika, Bruna, Nicole, Simon, Gaspa, and all the others I may have forgotten for the wonderful experience of these five years together. In particular I thank especially Fefe, Lisa, and Shaki for the last two years together and for the all the days we have passed studying the courses and overcoming all the difficulties we found ahead of us.

I also thank the Ferrara Crew, namely Patatèn-Fangèn, Mingo, Ergi, and Meg for their kindness and for not being too much angry with me due to my unexplained absences. Forgive me!

Hoping that I did not forget someone, I finally thank the readers of this thesis for their patience in reading this work.